HAW
HAMBURG

Masterarbeit

Jonas Christian Wolff

Investigation of the Critical RF Fields of Superconducting Cavity Connections

Fakultät Technik und Informatik
Department Informations- und Elektrotechnik

Faculty of Computer Science and Engineering
Department Information and Electrical Engineering

Jonas Christian Wolff

Investigation of the Critical RF Fields of Superconducting Cavity Connections

Mastertarbeit eingereicht im Rahmen der Masterprüfung
im Studiengang Master of Science Informations- und Kommunikationstechnik
am Department Informations- und Elektrotechnik
der Fakultät Technik und Informatik
der Hochschule für Angewandte Wissenschaften Hamburg

Betreuender Prüfer: Prof. Dr.-Ing. Ralf Wendel
Zweitgutachter: Dr. Alexey Sulimov

Eingereicht am: 24. Oktober 2019

Jonas Christian Wolff

Thema der Arbeit

Investigation of the Critical RF Fields
of Superconducting Cavity Connections

Stichworte

Hohlraumresonator, kritische Feldstärke, Koaxialleitung, Leistungskoppler, Quench, Strahlrohr, Supraleitung

Kurzzusammenfassung

Zur Optimierung der Strahlrohrlänge von supraleitenden Hohlraumresonatoren ist es notwendig, die kritische Hochfrequenz (HF)-Feldstärke am Flanschübergang des Resonators zu kennen, um einen vorzeitigen Verlust der Supraleitung am Übergang für den Fall einer Längenreduzierung des Strahlrohrs zu vermeiden. Für die erforderlichen Hochfrequenzmessungen kann zur Erhöhung der Feldstärke am Flanschübergang ein Zylinder im Zentrum des Strahlrohres eines einzelligen Testresonators verwendet werden, um Änderungen am Resonator zu vermeiden. Anhand der so erreichten Felderhöhung lässt sich der Flanschübergang virtuell verschieben. Im Rahmen dieser Arbeit wurde ein entsprechender Zylindereinschub für die Untersuchung der Feldlimitierung von 1.3 GHz TESLA-Typ-Resonator-Flanschübergängen implementiert und getestet.

Jonas Christian Wolff

Title of Thesis

Investigation of the Critical RF Fields
of Superconducting Cavity Connections

Keywords

cavity, critical field magnitude, coaxial line, input coupler, quench, drift tube, superconductivity

Abstract

To optimise the length of the drift tube of a superconducting radio frequency (SRF) cavity, it is required to know the critical value of the radio frequency (RF) field and thereby prevent a potential early quench at the flange connection in case of a drift tube length reduction. To avoid changes on the cavity used for the tests, the required RF cryogenic experiments can be carried out by using a cylinder in the center of a 1-cell cavity drift tube to increase the field magnitude at the connection. By means of this field increase the connection can be virtually displaced. In this thesis an appropriate cylinder insert for the investigation of the field limitation of 1.3 GHz TESLA-shape cavity connections was implemented and tested.

Table of Contents

List of Figures **iv**

List of Tables **x**

List of Abbreviations **xiii**

List of Symbols **xiv**

1 Introduction **1**

2 Theoretical Background **3**

2.1 The Pillbox Cavity 3
2.2 Electron Bunch Acceleration 8
2.3 Cavity Validation 8
2.4 The Residual Resistance Ratio 9
2.5 Estimation of the Surface Losses 9
  2.5.1 Surface Impedance of Normal Conductors 10
  2.5.2 Surface Resistance of Superconductors 11
  2.5.3 The Meissner Effect 14
  2.5.4 Field Limitation of Superconductors 14
2.6 Thermal Conductivity of Superconductors 17
2.7 Surface Treatment 17
  2.7.1 Etching 18
  2.7.2 Rinsing 19
2.8 Antenna Coupling 19

3 Motivation **23**

3.1 Model Requirement Analysis 24
3.2 Former Investigations 25

4 Development of the Cylinder Insert **26**

4.1 Selection of the RF Simulation Software 26
4.2 Influence of the Connection Gap Width 27
4.3 Automisation of a Stepwise Cylinder Length Increase 28
4.4 Optimisation of the Cylinder Length 32
4.5 Selection of the Cylinder Diameter 33
4.6 Field Magnitude Conversion 34

4.7 Investigation of a Possible Q_0 Degradation 36
  4.7.1 Determinition of the Surface Resistances 36
  4.7.2 Computation of Q_0 40
4.8 Computation of $\mathrm{Q}_{\mathrm{ext}}$ of the Input Antenna 40
4.9 Field Probe Antenna Design 42
4.10 Model Validation 46
  4.10.1 Field Distribution in the Test Cavity 46
  4.10.2 Field Distribution in the Connection Gap 48
4.11 Alteration of the Surface Losses 53
  4.11.1 Proportional Surface Losses in the Drift Tube 53
  4.11.2 Proportional Surface Losses in the Connection Gap 54
4.12 Impact of Minor Position Deviations 55
4.13 Manufacturing of the Cylinder Insert 57
  4.13.1 RF Shielding of the Connection Gap 57

5 Vertical Performance Testing **59**
5.1 Temperature Detection 59
  5.1.1 Sensor Calibration 61
  5.1.2 Determination of the Measurement Error 62
5.2 First Vertical Test: Unshielded Vacuum Gasket 62
  5.2.1 Measurement Execution 63
  5.2.2 Evaluation of the Temperature Sensors 64
  5.2.3 Test Results 64
5.3 Second Vertical Test: Unshielded Vacuum Gasket 64
  5.3.1 Measurement Execution 64
  5.3.2 Evaluation of the Temperature Sensors 67
  5.3.3 Test Results 67
5.4 Third Vertical Test: Shielded Vacuum Gasket 67
  5.4.1 Measurement Execution 69
  5.4.2 Evaluation of the Temperature Sensors 71
  5.4.3 Test Results 71

6 Conclusion **72**

7 Outlook **74**

8 Acknowledgement **75**

A Appendix **79**

Selbstständigkeitserklärung **80**

List of Figures

1.1 Depiction of a 9-cell accelerating cavity. [AESS12, p. 3, Figure 2]. 1

1.2 Single cell cavity used for development purposes. 2

2.1 A pillbox cavity with a radius r and a longitudinal length h. 4

2.2 Model of a pillbox cavity together with the required drift tubes (a). Exponential decay of the magnetic field in the drift tube of a single cell cavity evaluated along the sketched "field evaluation line". In the cavity cut the distribution of the electric field is shown (b). 6

2.3 Bessel functions J_0, J_1, J_2 and J_3 (a). Derivatives of the Bessel functions J'_0 to J'_3 (b). 7

2.4 9-cell accelerating cavity: The orange curve illustrates the electric field distribution in its zenith. The blue curve shows the ideal distribution from the perspective of an electron bunch (red) accelerated along the dotted beam axis by the electric field. . . 8

2.5 Trajectories of electrons close to the conductor's surface for the case $\ell > \delta_0$. Adapted from: [DG02, p. 114, Fig. 5.9]. 10

2.6 Screening of an external applied magnetic field by a perfect conductor or a superconductor (a) Trapping of the magnetic flux in the perfect conductor or rather expulsion of the flux in case of a superconductor (Meissner effect) (b). Adapted from: [Kle17, p. 11, Figure 2.2] and [PKH08, pp. 82-83, Figure 4.3/4.4] 14

2.7 Magnetic field magnitude B_i in the interior of the (super)conductor as a function of the magnitude of an external (magnetic) field (a). Magnetisation of the (super)conductor in dependence of an external (magnetic) field (b). Adapted from: [EH00, p. 284, Abb. 10.8] 15

2.8 Magnetic flux in the center of a spherical supercondcutor as a function of an external magnetic field B_e. Adapted from: [EH00, p. 286, Abb. 10.10] 16

2.9 Distribution of normal conducting (gray) and superconducting regions in the Shubnikov-phase. For one of the flux tubes the distribution of the magnetic field lines (blue) and the related shielding currents (orange) is illustrated. The shown arrangement of the flux tube in perfect crystals is known as the Abrikosov-structure. Adapted from: [EH00, p. 289, Abb. 10.14] 16

2.10 Magnetic field in a type II superconductor as a function of an external magnetic field (a). Related magnetisation M in dependence of the external magnetic field(b) (Below B_{c1} the conductor is in the Meissner state). Adapted from: [EH00, p. 288, Abb. 10.12] 17

2.11 Replication of the thermal conductivity (normalised by the thermal conductivity in the normal conducting state K_n close to $\mathrm{T_c}$) according to the BCS theory (orange; dashed) and of a measured Niobium sample (blue) as a function of the temperature. Addapted from: [PKH08, p. 76, Figure 3.12] 18
2.12 Depiction of the coupling antennas of a single cell cavity. The adjustable antenna with an adjustment range l is used for the power coupling. By means of the field probe antenna the transmitted power through the cavity can be measured. 19
2.13 Simplified block diagram of the measurement setup. The RF generator is used to provide the input power. By means of the circulator reflected power at the input coupler in case of an impedance mismatch is transmitted into a matched load. Thereby possible damage of the RF generator can be prevented. The field probe antenna is used to measure the transmitted power through the cavity. Adapted from: [Wan08, p. 141, Figure 5.3(a)] 20
2.14 Equivalent circuit of the measurement setup in steady state. Adapted from: [Wan08, p. 144, Figure 5.6] (a). Equivalent circuit of figure 2.14a with all components transformed into the circuit representing the RF generator. Adapted from: [Wan08, p. 145, Figure 5.7] (b). 20

3.1 Commonly used NbTi55-flange for SRF cavities at DESY (a). Aluminium vacuum gasket with high surface losses in case of an RF field exposure in comparison with superconducting Niobium (b). 23
3.2 Geometry of the TESLA-shape test cavity with the mounted cylinder insert. Adapted from: [Edw95, p. 122, Figure 4.2] 24
3.3 Depiction of a cut of a circular superconducting gasket for the use in a SRF particle separator. The gasket is combining the functionality of a vacuum gasket and a RF seal. UHV-tightness is ensured by Indium wires located in the grooves on both sides of the gasket. To ensure a good RF contact special shaped “lips“ to scratch through the oxide layer during the mounting process are used. Adapted from: [GLR77, Fig. 3] 25

4.1 Superfish simulation model of a single cell cavity with the mounted cylinder insert. In the magnification the connection gap is shown to illustrate the mesh cell distribution. 26
4.2 Sections of the used SF simulation models to illustrate the position of the field evaluation lines used for the comparison of the field distribution along the connection gap. 27
4.3 Comparison of the radial decay of the magnetic field along the connection gap of the commonly used connection (CUCD) and the connection design adapted for the use of the RF seal (AICD). 28
4.4 Section of a Superfish simulation model of a single cell cavity with the mounted cylinder insert to illustrate the position of the field evaluation point (red) in the center of the connection gap entrance. 29
4.5 Flowchart of the automised simulation series for a stepwise cylinder length increase. . 30

4.6 Absolute value of the electric field magnitude at the connection gap entrance $\mathrm{E_{con}}$ as a function of the cylinder length (a). Resonance frequency $\mathrm{f_r}$ as a function of the cylinder length (b). Absolute value of the magnetic field magnitude at the connection gap entrance $\mathrm{H_{con}}$ as a function of the cylinder length (c). All values are normalised by the maximum value of the simulated range. 31

4.7 Electric field distribution of the second resonance in the drift tube at 1.3 GHz for a cylinder length of 44.64 mm (a). For comparison the distribution for a cylinder with a length of 50 mm (b). 31

4.8 Flowchart of the cylinder length optimisation process. 32

4.9 Section of a Superfish simulation model of an actually displaced connection to illustrate the position of the field evaluation point (red) in the center of the connection gap entrance. 33

4.10 $E_z(z)$ equates the electric field distribution along the z-axis of the cavity. The product $E_z(z)\, cos(\phi)$ corresponds to the effective electric field from the perspective of an electron bunch synchronised to the phase traveling through the cavity. The grey dashed lines illustrate the evaluation range for the computation of E_{acc_sim} (a). Positions of the “field evaluation lines“ in the used Superfish model (b). 35

4.11 $\mathrm{H_{con}}$ as a function of $\mathrm{E_{max}}$ plotted to visualise the relation between the maximal electric field in the centre of the cavity’s cell and the magnetic field magnitude at the connection gap $\mathrm{H_{con}}$ (a). $\mathrm{H_{con}}$ as a function of $\mathrm{l_{drift\ tube}}$ to illustrate the dependence between the magnetic field magnitude at the connection and the drift tube length $\mathrm{l_{drift\ tube}}$ (b). 36

4.12 Superfish simulation models: Empty single cell cavity to validate the plausibility of the computed quality factors by a comparison with an old measurement (a); Single cell cavity with the mounted cylinder insert and an unshielded connection gap (b); The same model as in (b) without the connection gap to represent a perfectly shielded gap area (c). 37

4.13 Specific resistivity ρ of the NbTi55 alloy used for the flanges as a function of the temperature. 39

4.14 Specific resistivity σ of the AlMgSi alloy used for the vacuum gaskets as a function of the temperature. 39

4.15 CST simulation models of an empty single cell cavity (a) and a cavity with the mounted cylinder insert (b). For both models the external quality factor of the input coupler’s antenna is simulated as a function of the antenna penetration depth to investigate possible deviations between both models. 41

4.16 Comparison of the external quality factor as a function of the input coupler’s antenna penetration depth between the models of an empty single cell cavity and a cavity with the mounted cylinder insert. 41

4.17 Comparison of the external quality factor as a function of the input coupler’s antenna penetration depth between a simulation of an empty cavity and before recorded measurement points. 42

4.18 Thin field probe antenna design as an attempt to realise an antenna insensitive to length deviations (a). Shortened version of the adjustable antenna for the power coupling and therefore a cost efficient approach for the production at DESY (b). Comparison of the external quality factors as a function of the antenna length between both antenna designs. By the vertical dotted lines the length required for the desired external quality factor of $2.5 \cdot 10^{12}$ is marked (c). 43
4.19 Flange of a so called “HighQ antenna“ for the testwise power coupling during the production of 9-cell TESLA-shape cavities. This flange is used as the socket of the new field probe antenna (a). A shortened version of DESY’s input coupler’s antenna mounted on the HighQ flange. The antenna is used as a field probe during the performance tests (b). 44
4.20 Section of the Superfish simulation model used to find possible additional resonances at the operation frequency of the cavity. The picture shows the longest investigated antenna length. The red dot marks the point where the magnetic field magnitude is evaluated (a). Second resonance at the cavity’s operating frequency for an antenna length of 42.87 mm (b). Electric field distribution in the cylinder insert for a 5 mm longer field probe antenna (c). 45
4.21 Normalised magnetic field magnitude at the red evaluation point in figure 4.20a as a function of the field probe antenna length (including the diameter adapter) simulated as an approach to detect possible unwanted resonances at the operating frequency of the setup. 46
4.22 Alteration of the electric and the magnetic field distribution of the cavity by the cylinder insert. To investigate the impact of the cylinder insert on the field distribution the field density is evaluated along the depicted “field evaluation line“ for an empty reference cavity, a cavity with the mounted short cylinder insert ($l_c = 104.75\,\mathrm{mm}$) and one with the long insert ($l_c = 115.98\,\mathrm{mm}$). The plotted field densities are computed by Superfish. For the pictures of the field distributions CST Microwave Studio is used. 47
4.23 Comparison of the field distribution in the connection gap region of an actually displaced connection and a virtually displaced connection by the added coaxial line. The evaluation points are located at the left surface at the entrace of the connection gap as marked by a cross in the magnification windows. The magnitudes of the cylinder insert are bisected for the evaluation since the insert provides a field magnitude at the evaluation point twice as high as in an actually displaced connection. 49
4.24 Comparison of the field distribution in the connection gap region of an actually displaced connection and a virtually displaced connection by the added coaxial line. The evaluation points are located in the centre of the entrace of the connection gap as marked by a cross in the magnification windows. The magnitudes of the cylinder insert are bisected for the evaluation since the insert provides a field magnitude at the evaluation point twice as high as in an actually displaced connection. 51

4.25 Superfish simulation model of an empty single cell cavity used as a reference for the losses along the inner drift tube surface (Segment A) (a). Assignment of the surface segments in the models to represent the impact of the cylinder insert. In the picture the longer cylinder version is shown (b). 53
4.26 Surface Regions of the connection gap: Region 1: End of the drift tube (Nb); Region 2: Flange surface of the test cavity (NbTi55); Region 3: Vacuum gasket (AlMgSi); Region 4: Flange surface of the cylinder insert (NbTi55) (a). NbTi55 cavity flange (b). Aluminium vacuum gasket (c). 55
4.27 Position deviations of the cylinder insert: angle deviation (**blue**); centre point deviation (**orange**) (a), Position of the “field evaluation circle“ of the CST simulation model (b). Evaluation of the magnetic field magnitude deviations for the different deviation cases (c). 56
4.28 CAD model of the cylinder insert for the manufacturing. The Niobium part (RRR 47) is highlighted in red. The green section is made out of a NbTi55 alloy (By courtesy of D. Klinke) (a). Top view of the cylinder insert after the manufacturing (b). 57
4.29 The Niobium RF seal used as an attempt to shield the connection gap. By this seal the critical magnetic field of the connection should be increased (By courtesy of M. Schmoekel) (a). View through the test cavity on the mounted RF seal during the clean room assembly (By courtesy of M. Schmoekel) (b). 58

5.1 The cavity setup consisting of the field probe antenna, the cylinder insert, the test cavity and the input coupler mounted in a frame. On top, the socket of the field probe antenna mounted on the flange of the cylinder insert is shown. At the bottom, the housing of the input coupler is marked. 60
5.2 Arrangement of the temperature sensors mounted in vicinity of the vacuum gaskets of the investigated connection and the connection of the field probe antenna (a). Longitudinal cut of the cylinder insert connection to illustrate the longitudinal position of the temperature sensors (b). 61
5.3 Reference warmup curve based on the pressure change (a). Exemplary data fit of the channel Ch00 of the second vertical test to the reference curve (b). 62
5.4 Reference warmup curve based on the pressure change of the Helium bath together with the measurements of three temperature sensors in the bath before the offset correction (a). The same curves after the offset correction (b). 63
5.5 Q_0 vs. E_{acc} curve of the first vertical test to investigate the field limitation of a connection with an unshielded vacuum gasket. Additionally, the curve of a measurement of the empty test cavity is plotted for comparison. 63
5.6 Q_0 vs. E_{acc} curve of the second vertical test plotted in orange in comparison to a before measured curve of the empty test cavity. Due to a to low amount of samples recorded during the ring down, the measured points are extensively deviating from the actual values and can not be used for the further evaluation. 65

5.7 The power transmitted into the measurement setup P_{cavity} as a function of the power recieved at the field probe $P_{\text{transmitted}}$. The decreasing fraction of P_{cavity} recieved at the field probe for an increasing power P_{cavity} is caused by the increasing surface losses due to the surface warmup. The cause of the unstable behaviour for powers P_{cavity} above 30 W remains unknown. 66
5.8 Power transmitted into the setup P_{cavity} measured at the begin and the end of each time interval in relation to the signals of the temperature sensors in vicinity of the vacuum gaskets. On the top left corner a sketch of the temperature sensor locations is shown. 68
5.9 Comparison of the measured temperature sensor signals as a function of P_{cavity}. The different warmup regions are highlighted in the depiction of the sensor locations. . . 68
5.10 Detailed view of one of the temperature sensors mounted in vicinity of the test connections vacuum gasket (a). Depiction of the configuration of the used temperature sensors. Adapted from: [KMP94, p. 2, Figure 1] (b). 69
5.11 Seperated measurements of each temperature sensor as a function of P_{cavity} The sensors Ch00 - Ch03 are arranged symetrically in vicinity of the test connections vacuum gasket and the sensors Ch04 - Ch07 close to the gasket of the field probe antenna. 70

List of Tables

2.1 Roots x_{mn} of the Bessel functions J_0, J_1, J_2 and J_3. 7

2.2 Roots x'_{mn} of the Bessel functions derivatives J'_0, J'_1, J'_2 and J'_3. 7

4.1 Required cylinder lengths in dependence of the diameter to provide a magnetic field magnitude twice as large as at the reference field evaluation point. 34

4.2 Comparison of the intrinsic quality factors between the simulation and the measurements. For the calculation of the relative error the measurement values were used as reference. 40

4.3 Evaluation of the deviations of the cavity's TM_{010} resonant frequency caused by the short and the long cylinder insert. The resonant frequency $f_r = 1299.26491\,\mathrm{MHz}$ of an empty cavity is used as reference. 47

4.4 Relative error of the cavity parameters E_{pk} and H_{pk} caused by the short and the long cylinder insert. For the reference values a simulation model of an empty cavity is used. 47

4.5 Results of the data fit of the **electric** field magnitudes along the field evaluation lines. 50

4.6 Results of the data fit of the **magnetic** field magnitudes along the field evaluation lines. 50

4.7 Results of the average error computation for the **electric** field magnitudes along the evaluation lines depicted in figure 4.23 of the connection gap. 50

4.8 Results of the average error computation for the **magnetic** field magnitudes along the evaluation lines depicted in figure 4.23 of the connection gap. 50

4.9 Results of the data fits of the **electric** field magnitudes along the field evaluation lines after the evaluation point shift. 52

4.10 Results of the data fits of the **magnetic** field magnitudes along the field evaluation lines after the evaluation point shift. 52

4.11 Comparison of the average relative errors of the radially recorded **electric** field magnitudes between the following two cases. For the first case the field evaluation point is located at the left connection surface of the gap entrance as marked in figure 4.23 and in the second case (case II) in the centre of the gap entrance as marked in figure 4.24. The improvement factor indicates the error reduction of case II in comparison to case I. 52

4.12 Comparison of the average relative errors of the radially recorded **magnetic** field magnitudes between the following two cases. For the first case the field evaluation point is located at the left connection surface of the gap entrance as marked in figure 4.23 and in the second case (case II) in the centre of the gap entrance as marked in figure 4.24. The improvement factor indicates the error reduction of case II in comparison to case I. 52
4.13 Comparison of the proportional surface losses of the segments marked in figure 4.25b of the short and the long cylinder insert. The increase of the particular losses is visualised by the “increasement factor“. 54
4.14 Comparison of the proportional surface losses of the different regions in the connection gap between the following RF simulation models: An empty reference cavity, a cavity with a the short cylinder as well as one with the long cylinder insert. 54
4.15 Impact evaluation of minor cylinder insert centre point deviations (illustrated in figure 4.27a) to the extrema of the magnetic (H) field magnitudes along the field evaluation circle marked in figure 4.27b. The respectively evaluated deviations are marked by a cross. 56

5.1 Manually recorded data points at the beginning and the end of each input power ($P_{forward}$) interval. The power transfered into the cavity P_{cavity} is calculated on basis of $P_{forward}$ and $P_{reflected}$. 66

List of Abbreviations

AICD addapted insert connection design.

CERN Conseil européen pour la recherche nucléaire.

CUCD commonly used connection design.

DC direct current.

DESY Deutsches Elektronen-Synchrotron.

European XFEL X-Ray Free-Electron Laser.

FLASH Free-electron LASer in Hamburg.

HF Hochfrequenz.

LAACG Los Alamos Accelerator Code Group.

PETRA III Positron-Elektron-Tandem-Ring-Anlage.

PLL phase locked loop.

RF radio frequency.

RRR residual resistance ratio.

SNR signal-to-noise ratio.

TE transverse electric.

TESLA TeV-Energy Superconducting Linear Accelerator.

TM transverse magnetic.

UHV ultra-high vacuum.

List of Symbols

B_{c1} Lower critcal magnetic field magnitude of a Type II superconductor.

B_{c2} Upper critcal magnetic field magnitude of a Type II superconductor.

B_c Critical external magnetic field magnitude.

B_{eff} Effective external magnetic field magnitude.

B_e External magnetic field magnitude.

B_i Interior magnetic field magnitude.

B_{con} Magnetic flux in the centre of the connection gap entrance.

Δ Superconducting energy gap.

D Demagnetisation factor.

E_z Electric field distribution in logitudinal direction.

E_{acc_sim} Average accelerating field of the simulation.

E_{acc} Average accelerating field.

E_{max_meas} Maximal electric field of the measurement.

E_{max_sim} Maximal electric field of the simulation.

E_{max} Maximal electric field.

E_{pk} Surface peak electric field.

Γ Reflection coefficient.

H_{con} Magnetic field in the centre of the connection gap entrance.

H_{pk} Surface peak magnetic field.

J_v Bessel functions.

K_n Thermal conductivity in the normal conducting state close to $\mathrm{T_c}$.

K_s Thermal conductivity in the superconducting state.

M Magnetisation.

N_{eff} Effective number of free charge carriers.

P_{cavity} Power stored in the cavity.

P_{ext} Power dissipation of the power coupling circuit.

$P_{forward}$ Power transfered into the cavity.

$P_{reflected}$ Power reflected at the input coupler.

$P_{transmitted}$ Power recieved by the field probe antenna.

Q_0 Intrinsic quality factor.

Q_L Loaded quality factor.

Q_{ext} External quality factor.

Q_t External quality factor of the field probe.

R_a Shunt impedance.

R_{nl} Non-linear contribution to the surface resistance.

R_{res} Residual resistance.

R_s Surface resistance.

T_0 Period time of the fundamental mode resonant frequency.

T_{cav} Transition time through the cavity.

T_c Transition temperature.

V_{acc} Accelerating voltage.

W Energy stored in the cavity.

X_s Surface reactance.

β_{ext} Coupling parameter for the input coupler.

β_t Coupling parameter for the field probe antenna.

c_0 Vacuum speed of light.

χ Magnetic susceptibility.

δ_{eff} Skin depth of the anomalous skin effect.

δ_0 Skin depth.

f_c Cut-off frequency.

γ Factor to describe the scattering characteristics of electrons at the conductor surface.

h Longitudinal length of the pillbox cavity.

k_B Boltzmann constant.

k Factor for the calculation of $\mathrm{E_{acc}}$.

$l_{drift\ tube}$ Length of the drift tube.

λ_0 Wave length in free space.

λ_L London penetration depth.

λ_c Cut-off wave length.

λ_w Resulting wavelength in a waveguide.

ℓ Mean free path of an electron before scattering.

μ_r Relative permeability.

n_n Normal conducting fraction of charge carriers.

n_s Superfluid fraction of charge carriers.

ω_0 Angular frequency.

p Factor for the calculation of $\mathrm{H}_{\mathrm{con}}$.

σ_n Conductivity of the normal fluid component.

σ_s Conductivity of the superfluid component.

σ_{eff} Electrical conductivity of the anomalous skin effect.

σ_{dc} Electrical conductivity.

ε_r Relative permittivity.

x'_{mn} Roots of the Bessel functions deviatives.

x_{mn} Roots of the Bessel functions.

ξ_0 Coherence length.

1 Introduction

The Deutsches Elektronen-Synchrotron (DESY) in Hamburg develops and operates large accelerator facilities for scientific research. These accelerators like the Free-electron LASer in Hamburg (FLASH), the Positron-Elektron-Tandem-Ring-Anlage (PETRA III) and the European X-Ray Free-Electron Laser (European XFEL) are used for nano and material science, for the investigation of chemical reactions and molecular biology. Originally, the related accelerator technology was developed for high energy physics applications. Independent of their research fields all of these facilities have in common, that they use cavities to provide high electric fields for the acceleration of electron bunches. Mainly for mechanical reasons the accelerating lines of these facilities are seperated into nine cell cavity units as depicted in figure 1.1. So called drift tubes with the length of an integer multiple of the operating frequency's wavelength connect the idividual cavities.

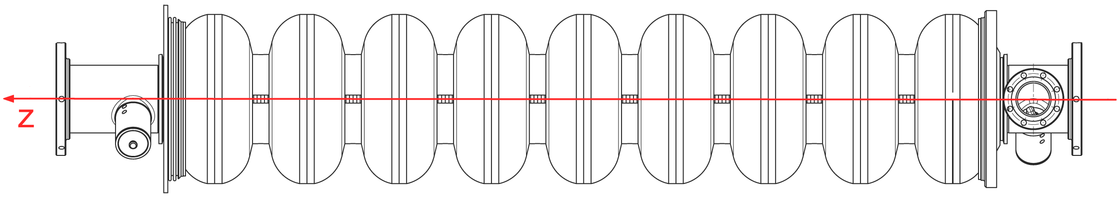

Figure 1.1: Depiction of a 9-cell accelerating cavity. [AESS12, p. 3, Figure 2].

To achive a high power efficiency most modern particle accelerators operate with cavities built of superconducting Niobium. For an economical operation the temperature has to be 2 K. Even in the superconducting state with zero direct current (DC) resistance, still minor surface power losses in case of an exposure to an electro-magnetic field exist. Either these losses by the related surface warmup or a material dependent critical magnetic field causing a breakdown of the superconductivity (called quench) are limiting the maximal possible field density in the cavity. Furthermore, surface defects like scratches or contaminations may limit the field density. For the operating mode the highest magnetic field magnitude is located at the equator of each cell (figure 1.2). Therefore, this region should be the field limiting element of the cavity unit. The field limitation of the connection area is usually far below the possible magnetic field magnitudes at the cells equator due to the geometry and the used materials. Since the cavities are operated below the cut-off frequency of the drift tubes the field density along the tube is exponentially decaying. For this reason the field density at the connection is usually low. To avoid that the connection area becomes the field limiting element of the cavity a minimal drift tube length ensuring the required field decay, must not be underrun.

Within this thesis the radio frequency (RF) field limitations of commonly used superconducting radio frequency (SRF) cavities at DESY as well as an attempt to increase this critical field density is investigated. To avoid any mechanical changes on the test cavity, a cylinder in the center of the drift tube is used to turn it into a coaxial line and thereby increase the field density at the connection. By increasing the field density the drift tube length and hence the distance between the iris and the connection can be virtually reduced.

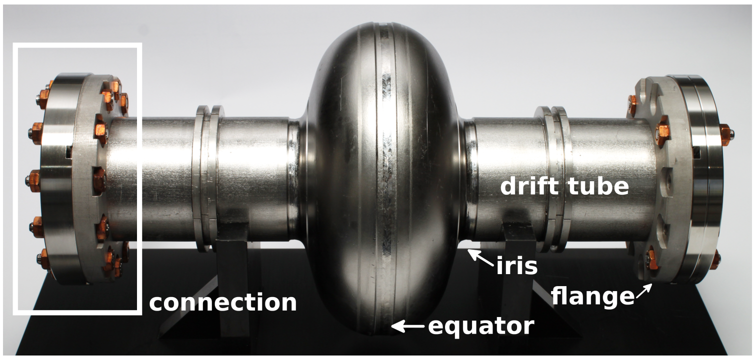

Figure 1.2: Single cell cavity used for development purposes.

The first chapter summarises the theoretical fundamentals required for the development as well as the evaluation of the connection displacement model and the subsequent performance tests. Within this chapter the theoretical fundamentals of cavities, a set of figures of merit for the classification of different cavity models, the basics of superconductivity and the needed theory for the power coupling for the later performance tests is explained. In the following chapter the motivation for the development of the connection displacement model in form of the cylinder insert is outlined and an overview of former similar investigations is given. Subsequently, the development process of the cylinder insert is described followed by a validation of the model to ensure the behaviour of an actually displaced connection can be mapped by the cylinder insert. Furthermore, an expected Q_0 degradation of the setup mainly caused by the additional losses at the normal conducting vacuum gasket is investigated. This investigation is needed to guarantee that impedance matching can be ensured within the adjustment range of the input coupler. Based on this information the required antenna lengths for the input coupler and the field probe antenna can be determined. At last, the performed performance tests are described in the order of their outcarrying, to give a comprehensible overview of the setup changes after each test. Finally, the results of the thesis are summarised in the conclusion.

2 Theoretical Background

This chapter outlines the theoretical fundamentals of superconducting accelerating cavities required for the development process of the cavity connection displacement model as well as the subsequent performance tests. The functionality and the dimensioning will be explained by means of the elementary cavity shape, the so called pillbox cavity. Afterwards, the acceleration process of electron bunches is described as a short introduction to the operation of cavity resonators in an accelerating facility. For a validation of the model a set of commonly used figures of merit is introduced. They are used for an eigenfrequency independent comparison of different cavity shapes. [PKH08, p. 37]
To investigate a potential degradation of the intrinsic quality factor Q_0 of the test cavity caused by the added cylinder insert, the required theory for the calculation of the surface resistance of normal- and superconductors is explained. Furthermore, the basics of superconductivity are presented for the explanation of material and geometry dependent field limitations. Afterwards, a short overview of commonly used surface treatments to avoid field and quality factor limitations caused by mechanical damages or microscopic contaminations of the Niobium surface is given [PKH08, p. 120]. At last, the desired coupling characteristics of the power coupler and the field probe antenna for the later performance tests are described.

2.1 The Pillbox Cavity

A pillbox cavity is a circular waveguide closed at both openings by conducting end plates shown in figure 2.1. For the pillbox shape the RF field density is limitted by multipacting [PKH08, p. 37]. Hence, it has no practical application in accelerating facilities [PKH08, p. 37]. Multipacting describes the phenomenon of by an RF field released and accelerated electrons hitting and thereby ionising the inner surface of the cavity. Due to the ionising electrons are released and will subsequently also participate in this process. Consequently, any additional RF power will be absorbed by this effect heating up and potentially damaging the inner surface. Multipacting can be preserved by altering the pillbox shape to an eliptical form. [PKH08, p. 179]
Although the pillbox cavity has no practical application it is nevertheless the ideal shape to exemplify the dimensioning and the functionality of accelerating cavities since for the pillbox cavity the field distribution can be analytically calculated [PKH08, p. 37]. For TESLA-shape cavities this is impossible. The TESLA-shape is an eliptical cavity design commonly used for SRF cavities at DESY but originally developed for a potential usage in the TeV-Energy Superconducting Linear Accelerator (TESLA) described in detail in [Pro93]. In the following the dimensioning of a pillbox cavity for a given resonant frequency is explained.

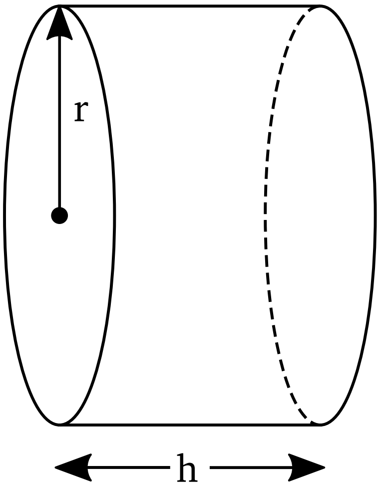

Figure 2.1: A pillbox cavity with a radius r and a longitudinal length h.

In case a RF driven waveguide will be shortcutted on one end, a standing wave will emerge from the superposition of the forwarded wave and its reflection. For this standing wave the normal component of the magnetic field and the tangential component of the electric field will be zero at the shortcutted waveguide end as well as at integer multiples of $\lambda_w/2$. Where λ_w [Peh12, p. 37, eq. (1.142)] is the resulting wavelength of the standing wave in the waveguide. [Peh12, p. 147]

$$\lambda_w = \frac{\lambda_0}{\sqrt{\mu_r\,\varepsilon_r}} \cdot \frac{1}{\sqrt{1-(\lambda_0/\lambda_c)^2}} \tag{2.1}$$

Since under vacuum conditions the relative permeability μ_r and the relative permittivity ε_r equals one, the equation for the calculation of the waveguide wavelength can be simplified as follows:

$$\lambda_w = \frac{\lambda_0}{\sqrt{1-(\lambda_0/\lambda_c)^2}}. \tag{2.2}$$

Thereby, the wavelength λ_0 is the wavelength in free space of the desired resonance frequency and λ_c the so called cut-off wavelength. Below the related cut-off frequency there is no propagation along the waveguide and the field magnitude is exponentially decaying. The slope of this decay can be described by equation (2.3) [Mei66, p. 119, eq. (336);(337)]. The field decay along the drift tube mentioned in the introduction can be described approximately by this equation. [Mei66, p. 119]
A minor deviation must be expected because of the different field distribution at the entrance of the drift tube:

$$|\underline{A}(z)| = |\underline{A}(0)| \cdot e^{\pm\alpha\, z} \quad \text{where} \quad \alpha = \frac{2\,\pi}{\lambda_c}\sqrt{1-\left(\frac{\lambda_c}{\lambda_0}\right)^2}. \tag{2.3}$$

For a circular waveguide the cut-off frequency f_c is given by equation (2.4) [ROKS53, p. 240, eq. (5-41)]. The value $\mathrm{x_n}$ is the root of the Bessel function or its deviation related to the dominant mode. For the dominant mode of a circular waveguide ($\mathrm{TE_{11}}$) x_n equals 1.8412.

$$f_c = \frac{x_n}{2\,\pi\,r\sqrt{\mu_0\,\varepsilon_0}} \tag{2.4}$$

The on one end shortcutted circular waveguide can be turned into a pillbox cavity by mounting a second plate alongside the wave guide. In case of an external excitation through a hole in one of the plates or by a coupling antenna the field density in the cavity will reach its maximum if the additional plate is located at a distance to the first plate of an integer multiple p of $\lambda_w/2$. For the related resonance frequencies the $\mathrm{TM_{01p}}$ modes will be excited in the cavity.[Peh12, p. 148]

In a pillbox cavity transverse magnetic modes $\mathrm{TM_{mnp}}$ as well as transverse electric modes $\mathrm{TE_{mnp}}$ can be excited [Wan08, pp. 25-27]. The different modes of each type are distincted by a set of numbers (mnp) in the subscript of each mode given by the following nomenclature:

- the index m expresses the of full period variations along the angle Θ,
- the second index n is the number of zeros along the cavity's radius excluding a possible zero in the centre,
- The last subscript index describes the number of half period variations in the cavity's cell in z direction (the beam axis) [Wan08, pp. 25-27].

For the acceleration of electrons the TE modes have no practical application in a pillbox cavity, since they have no longitudinal electric field usable for the beam acceleration. Only the $\mathrm{TM_{0np}}$ monopole modes can be used in principle since the longitudinal component of E must not vanish at the beam axis. Usually the monopole mode with the lowest eigenfrequency will be used. Modes of higher order may be excited by the beam with the disadvantage of a deflecting impact on the beam itself. [PKH08, p. 41]
To enable the beam to passage through the cavity, drift tubes shown in figure 2.2a have to be added on both ends of the cavity. For these drift tubes a diameter with a related cut-off frequency above the mode used for the acceleration has to be chosen to avoid that the cavity field can propagate out of the cavity. Due to the operation below the cut-off frequency the field density is exponentially decaying alongside the drift tube. This decay is illustrated in figure 2.2b for the drift tube of a TESLA-shape single cell cavity. Since the added drift tubes alter the field, the actual distribution can only be approximately calculated. For the analytical dimensioning the impact of the drift tubes needs to be neglected. If a higher precision is required, computer codes are used to compute the related field distribution. [PKH08, p. 41]

For the acceleration of electrons usually the monopole mode with the lowest resonant frequency $\mathrm{TM_{010}}$ is used. Like all transverse magnetic modes this mode is independent from the cavity's length since the magnetic field in z-direction is zero [Wan08, pp. 24-25]. For this mode the peak electric field is located along the beam axis [Wan08, p. 25]. The resonant frequencies of all TE and

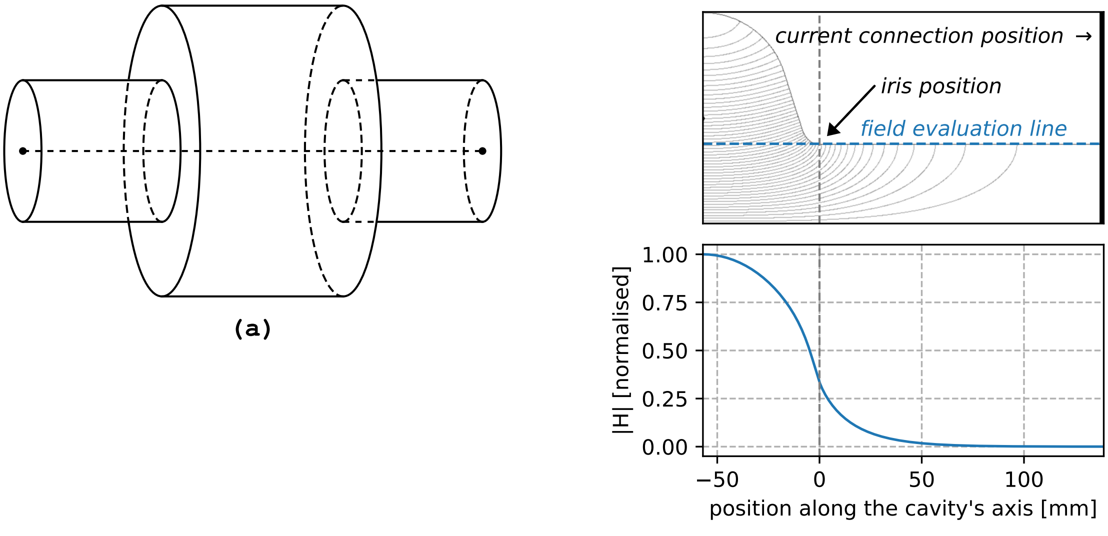

(a)

(b)

Figure 2.2: Model of a pillbox cavity together with the required drift tubes (a). Exponential decay of the magnetic field in the drift tube of a single cell cavity evaluated along the sketched “field evaluation line“. In the cavity cut the distribution of the electric field is shown (b).

TM modes can be derived by equation (2.5) [Dav19, p. 347, eq. (14.69)] for the TE modes and by equation (2.6) [Dav19, p. 346, eq. (14.64)] for the TM modes. [Dav19, pp. 346-347]

$$f_r(TE) = c_0 \cdot \sqrt{\left(\frac{x'_{mn}}{2\pi r}\right)^2 + \frac{1}{4}\left(\frac{p}{h}\right)^2} \tag{2.5}$$

$$f_r(TM) = c_0 \cdot \sqrt{\left(\frac{x_{mn}}{2\pi r}\right)^2 + \frac{1}{4}\left(\frac{p}{h}\right)^2} \tag{2.6}$$

Where x_{mn} are the roots of the Bessel functions in figure 2.3 in equation (2.7) [Jac82, p. 123, eq. 3.82, 3.83] and x'_{mn} the related roots of their derivatives. The roots of the Bessel functions J_0, J_1, J_2 and J_3 are listed in table 2.1 and for their derivatives in table 2.2.

$$\begin{aligned} J_v(x) &= \left(\frac{x}{2}\right)^v \sum_{i=0}^{\infty} \frac{(-1)^j}{j!\Gamma(j+v+1)} \left(\frac{x}{2}\right)^{2j} \\ J_{-v}(x) &= \left(\frac{x}{2}\right)^{-v} \sum_{i=0}^{\infty} \frac{(-1)^j}{j!\Gamma(j-v+1)} \left(\frac{x}{2}\right)^{2j} \end{aligned} \tag{2.7}$$

For the numerical computation of the needed Gamma function in 2.8 [Pap11, p. 442, eq. II-295] the method `gamma()` of the Python `math` library was used.

$$\Gamma(\alpha) = \int_0^{\infty} t^{\alpha-1} \cdot e^{-t} dt \quad (\alpha > 0) \tag{2.8}$$

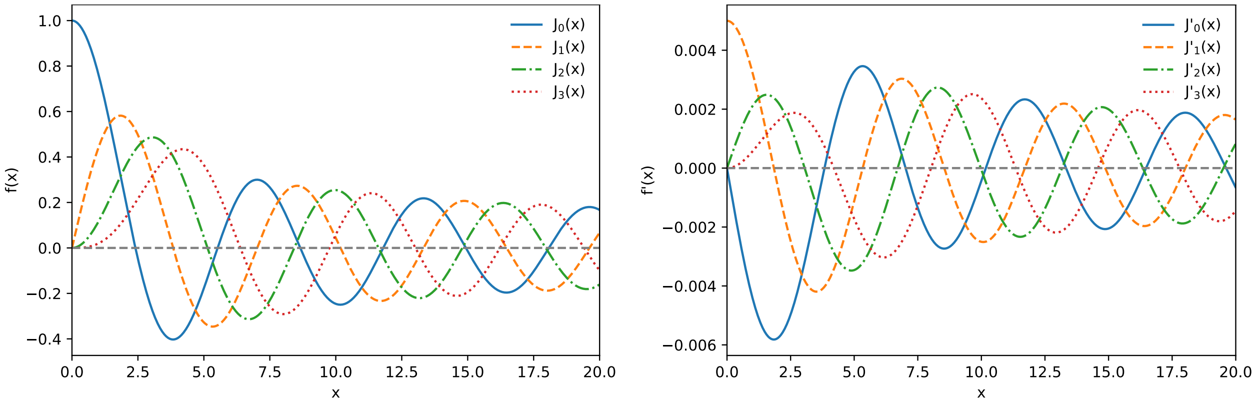

(a) **(b)**

Figure 2.3: Bessel functions J_0, J_1, J_2 and J_3 (a). Derivatives of the Bessel functions J'$_0$ to J'$_3$ (b).

Table 2.1: Roots x_{mn} of the Bessel functions J_0, J_1, J_2 and J_3.

m	n = 1	n = 2	n = 3	n = 4
0	2.4048	5.5201	8.6537	11.7915
1	3.8317	7.0156	10.1735	13.3237
2	5.1356	8.4172	11.6198	14.7960
3	6.3802	9.7610	13.0152	16.2235

Table 2.2: Roots x'_{mn} of the Bessel functions derivatives J'$_0$, J'$_1$, J'$_2$ and J'$_3$.

m	n = 1	n = 2	n = 3	n = 4
0	0.0000	3.8317	7.0156	10.1735
1	1.8412	5.3314	8.5363	11.7060
2	3.0542	6.7061	9.9695	13.1704
3	4.2012	8.0152	11.3459	12.9331

The radius r of the pillbox cavity can be calculated by using the formula 2.6. Since for the TM_{010}-Mode the component p equals 0, the part $1/4(p/h)^2$ vanishes we have:

$$r = \frac{c_0\, x_{mn}}{2\pi f_r(TM_{010})}. \tag{2.9}$$

For the dimensioning of the longitudinal length h [PKH08, p. 43, eq. (2.38)] of each pillbox cell the velocity of the accelerated electrons is assumed to be c_0 [PKH08, p. 42]. The time an electron needs to passage the cavity T_{cav} is then given by $T_{cav} = h/c_0$. To maximise the kick an electron recieves during the passage of the cavity needs to equal one half of an RF-period $T_0/2$ as follows [PKH08, p. 42]:

$$h = \frac{\pi\, c_0}{\omega_0}. \tag{2.10}$$

The effective accelerating voltage V_{acc} [PKH08, p. 42, eq. (2.36)] from the perspective of an accelerated electron is given by the line integral of E_z [PKH08, p. 42]:

$$V_{acc} = \left| \int_0^h E_z(\rho = 0, z)\, e^{i\,\omega_0\, z/c} dz \right|. \tag{2.11}$$

The average accelerating field E_{acc} [PKH08, p. 43, eq. (2.38)] from the perspective of an electron is given by [PKH08, p. 43]:

$$E_{acc} = \frac{V_{acc}}{h}. \tag{2.12}$$

2.2 Electron Bunch Acceleration

Within this section the acceleration process of electron bunches in TESLA-shape cavities depicted in figure 2.4 is described. For the acceleration the cavities are operated in the so called π-mode. In this mode the field in every second cell points in the oposite direction shown by the orange curve. If an electron bunch travels through one of the cells with an electric field pointing in the contrary direction the bunch would be consequnetly decelerated. However, since the length of the cavity cells equals the distance an electron bunch with almost the vacuum speed of light c_0 travels within half of an oscillation period, a continious acceleration illustrated by the blue curve can be achieved. An appropriate synchronisation to the phase of the electro-magnetic field is needed for this purpose. [PKH08, p. 3]

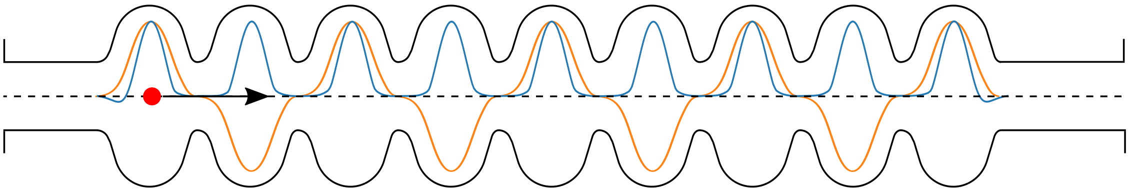

Figure 2.4: 9-cell accelerating cavity: The orange curve illustrates the electric field distribution in its zenith. The blue curve shows the ideal distribution from the perspective of an electron bunch (red) accelerated along the dotted beam axis by the electric field.

2.3 Cavity Validation

For a comparison of different cavity shapes during the development a set of eigenfrequency independent figures of merit were defined [PKH08, pp. 43-44].
To evaluate the power efficiency of accelerating cavities, the intrinsic quality factor Q_0 [PKH08, p. 45, eq. (2.47)] is used. Q_0 is defined as the ratio between the energy W stored in the cavity multiplied by the angular frequency ω_0 and the in the surface dissipated power P_{cavity} as follows [PKH08, p. 45]:

$$Q_0 = \frac{\omega_0 \, W}{P_{cavity}}. \tag{2.13}$$

Besides Q_0 the shunt impendance R_a [PKH08, p. 47, eq. (2.62)] is an important quantity to characterise the cavity's efficiency. The definition used for accelerating cavities is different from the shunt impedance in other fields like for example the circuit theory. For the acceleration mode a large shunt impedance is desired since in this case the losses are low. [PKH08, p. 47]

$$R_a = \frac{V_{acc}^2}{P_{cavity}} \tag{2.14}$$

The possible surface field magnitudes of the electric and the magnetic field of superconducting cavities are both limited. The peak surface magnetic field H_{pk} is given by the magnitude at which the surface loses its superconducting state, described in detail in section 2.5.2. The peak surface electric field E_{pk} is limitted by possible field emission in high field regions. For this reason the fractions E_{pk}/E_{acc} and H_{pk}/E_{acc} have to be minimised during the cavity development to optimise the performance. [PKH08, p. 43]

2.4 The Residual Resistance Ratio

Atoms in a conductor are arranged in a lattice structure. Within the lattice the valence electrons of the involved atoms can move freely due to a low bound between the valence electrons and their related atomic nucleus. The freely moving valence electrons are responsible for the thermal and electrical conductivity of the conductor. Both, the electrical and the thermal conductivity are dependent on the scattering characteristics of the valence electrons within the lattice. Electrons are scattered by lattice defects like material impurities and missing or interstitial atoms in the lattice structure. Furthermore, scattering occurs because of temperature dependent lattice vibrations called Phonons. For this reason, the mean free path ℓ an electron travels before scattering and thereby the related conductivity increases for lower temperatures. The slope of this increase depends on the second scattering contributor, the material impurities. For this reason the so called residual resistance ratio (RRR) is used as an indicator of the material purity as well as the thermal and electrical characteristics at low temperatures. [PKH08, pp. 57-59]

The RRR is defined as the fraction between the specific resistivity at room temperature (293.15 K) and at 4.2 K in the normal conducting state [Wan08, p. 418].

2.5 Estimation of the Surface Losses

To predict the surface losses and the related intrinsic quality factor Q_0 of the measurement setup via RF simulations the surface resistance R_s of each surface must be known. The surface resistance depends besides to the frequency mainly on the conductivity state (normal or superconducting) and the material purity. In this section the theory for the calculation or computation of the surface resistance for the different states is explained. Furthermore, field and temperature dependent conductivity state changes of superconducting materials are presented since related phenomenons may occur in the investigated connection area of the cavity at higher RF fields.

2.5.1 Surface Impedance of Normal Conductors

Currents induced by RF fields are only present in the surface layer of a conducting material since these surface currents shield the electric field from the bulk of the conductor [PKH08, p. 78]. This phenomenon is known as the normal skin effect. The related penetration depth of the magnetic field component the so called skin depth δ_0 [PKH08, p. 78, eq. (4.4)] dependent on the frequency and the specific material conductivity σ_{dc} is given by [PKH08, p. 78]:

$$\delta_0 = \frac{1}{\sqrt{\pi\, f\, \mu_0\, \sigma_{dc}}}. \tag{2.15}$$

For the evaluation of the particular surface losses the surface impedance $\underline{Z}_s$ [PKH08, p. 78 eq. (4.7)] of the conductor is requiered:

$$\underline{Z}_s = \frac{\tau_n}{\sigma_{dc}} = \sqrt{i\, \omega_0\, \mu_0} = R_s + i\, X_s. \tag{2.16}$$

The imaginary part of $\underline{Z}_s$ represents the phase difference between the current in the material and the RF field [PKH08, p. 78]. This phase difference and therefore the impact of the surface reactance X_s is low for frequencies below $\omega_0 \approx 10^{11}$ Hz [Jac82, p. 337]. Thus for the given area of application X_s can be neglected. The remaining surface resistance R_s [PKH08, p. 79 eq. (4.9)] can be calculated by [PKH08, p. 79]:

$$R_s = \frac{\sqrt{\pi\, f\, \mu_0}}{\delta_0} = \frac{1}{\sigma_{dc}\, \delta_0}. \tag{2.17}$$

This relation between the surface resistance and the reciprocal of the product of the specific conductivity and the skin depth is only valid as long as the mean free path ℓ of electrons in the skin layer $\ell << \delta_0$. Especially for conductors with a high purity and therefore a low amount of lattice defects, the condition $\ell << \delta_0$ is no longer fulfilled. In this case the electrons are only for a part of their path in the region of the penetration depth of the RF field if the electron travels perpendicular to the conductors surface as illustrated in figure 2.5. [Hum71, p. 83], [PKH08, p. 79], [DG02, p. 114]

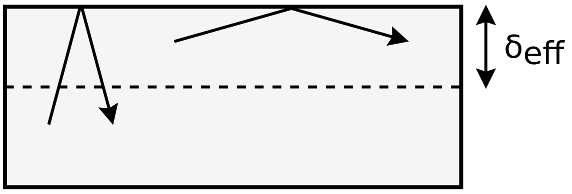

Figure 2.5: Trajectories of electrons close to the conductor's surface for the case $\ell > \delta_0$. Adapted from: [DG02, p. 114, Fig. 5.9].

Only the fraction of electrons traveling nearly parallel to the surface will be scattered. This reduces the efficiency of carrying RF currents and hence increases the surface resistance R_s since the effectiveness of shielding the electric field from the bulk of the conductor decreases. The lowered shielding capability yields to an increasing effective skin depth δ_{eff} in equation (2.18) [DG02,

p. 114 eq. (5.2.30)]. This effect is known as the anomalous skin effect. [Hum71, p. 83], [PKH08, p. 79], [DG02, p. 114]

$$\delta_{eff} = \left(\frac{c_0^2\,\ell}{2\,\pi\,\omega\,\gamma\sigma_{dc}} \right)^{1/3} \tag{2.18}$$

Since the effective number of free charge carriers $N_{eff}= N\delta_{eff}/\ell$ will be reduced by this effect also the conductivity σ_{eff} [DG02, p. 114 eq. (5.2.29)] changes as follows [DG02, p. 114]:

$$\sigma_{eff} = \gamma\,\sigma_{dc}\frac{\delta_{eff}}{\ell}. \tag{2.19}$$

The factor γ describes the scattering characteristic of the electrons on the conductor surface. It varries in the range from $\gamma = 8/9$ for specular reflection to $\gamma = 1$ for diffuse reflection. [DG02, p. 114]

For the anomalous skin effect the surface impedance $\underline{Z}_s$ [DG02, p. 115, eq. (5.2.32)] is given by:

$$\underline{Z}_s = R_s + i\,X_s = \frac{1 - i\,\sqrt{3}}{\delta_{eff}\,\sigma_{eff}} = \left[\left(\frac{2\,\pi\,\omega_0}{c_0^2} \right)^2 \frac{\ell}{\gamma\,\sigma_{dc}} \right]^{1/3} (1 - i\sqrt{3}) \tag{2.20}$$

and there is no dependence on the mean free path ℓ and the temperature for the effective conductivity and the surface resistance existing [DG02, p. 115].

2.5.2 Surface Resistance of Superconductors

In 1911 Kamerlingh Onnes investigated the electrical conductivity of metals at low temperatures. To avoid a decreased conductivity by impurities he studied the conductivity of high purity Mercury at temperatures below 4.2 K. Due to the limited accuracy of the measurement setup it was not surprising that he could not measure any resistance, but when he increased the impurities the resistance stayed zero. In following experiements he lowered the temperature stepwise and noticed that at some point the resistance drops down to zero. He concluded that the conductor merged into a new (superconducting) state at a transition temperature T_c. This behaviour could not be explained by the theory at that time. [Ric65, pp. 1-3]

In the following time, mainly two theories were developed to explain the superconducting phenomenon. Within this section a compendium of these theories required for the calculation of the surface resistance in the superconducting state is given.

The Two Fluid Model

The two fluid model was an early approach of C. J. Gorter and H. B. G. Casimir [GC34, p. 963] to explain superconductivity by introducing two different densities of charge carriers. The density n_n for a representation of a normal conducting component and n_s as a frictionless superconducting part. Consequently, for the calculation of the surface impedance the two fluid model destinguishes between two conductivity types: the conductivity of the normal fluid σ_n [PKH08, p. 86 eq. (4.36)] and σ_s [PKH08, p. 86 eq. (4.36)] as the superfluid component. [Kle17, p. 10], [PKH08, p. 86], [Ric65, p. 6]

$$\sigma_n = \frac{n_n\, e^2\, \tau}{m_e} \quad \text{and} \quad \sigma_s = \frac{n_s\, e^2}{m_e\, \omega}. \tag{2.21}$$

In contrast to normal conductors, for superconductors the skin depth is given by the frequency independent London penetration depth λ_L [Tho04, p. 26 eq. (2.13)], [Tho04, p. 26]:

$$\lambda_L = \sqrt{\frac{m_e}{\mu_0\, n_s\, e^2}}. \tag{2.22}$$

The surface impedance $\underline{Z}_s = R_s + j\, X_s$ can be calculated by the surface resistance R_s [PKH08, p. 86 eq. (4.38)] and the surface reactance X_s [PKH08, p. 86 eq. (4.39)]:

$$R_s = \frac{1}{2}\, \sigma_n\, \omega^2\, \mu_0^2\, \lambda_L^3, \tag{2.23}$$

$$X_s = \omega\, \mu_0\, \lambda_L. \tag{2.24}$$

Except for temperatures close to T_c the surface impedance is dominated by the imaginary part [PKH08, p. 86]. In the superconducting state the surface resistance is proportional to the normal conductivity of the material since the fraction of normal conducting charge carriers increase exponentially until T_c is reached [Jun12, p. 12].

The Microscopic Theory of Bardeen, Cooper and Schrieffer

Similar to the two fluid model the BCS theory introduced in 1957 by Bardeen Cooper and Schrieffer [BCS57] explains the superconducting phenomenon by two different charge carriers [Jun12, p. 13]. According to the BCS theory below the transition temperature T_c an exponentially increasing fraction of electrons is bound in so called cooper pairs. Divergent to the remaining unbound electrons the cooper pairs can travel frictionless through the lattice without beeing scattered. [PKH08, p. 72]
Predictions of the surface resistance based on the two fluid model show a decreasing resistance for higher material purities. However, in a comparison to measurements of different material purities it can be noticed that the lowest surface resistance is related to an intermediate material purity with a RRR of about 10 in case of Niobium. The reason for this discrepancy is that the two fluid model does not consider the impact of the coherence length ξ_0, the electron mean free path before scattering ℓ and the superconducting energy gap Δ. [Kle17, p. 14], [Jun12, p. 13]
Here, the coherence length ξ_0 describes the length upwards two electrons bound in a cooper pair can interchange so called virtual phonons. These phonons are called virtual because they exist only for the transistion between the two electrons without any effect on the atom lattice. For the formation of cooper pairs the binding caused by these virtual phonons needs to be larger than the

electrostatic repulsion of the electrons. Thereby, the coherence length can be seen simplified as the cubic expansion of a cooper pair. [BK13, pp. 125-126]
The energy gap Δ correlates to the pairing energy of a cooper pair [PKH08, p. 70]. Approximately, it can be derived by the constant in equation (2.25) [EH00, p. 321, eq. (10.96)] where k_B depicts the Boltzmann constant.

$$\frac{\Delta(0)}{k_B\,T_c} = 1.76 \quad \text{at } T = 0 \tag{2.25}$$

For the estimation of the surface resistance by means of the BCS theory, expressions developed by Mattis and Barden presented in [MB58] are used. With these expressions $\mathrm{R_s}$ can be estimated for a magnetic flux below 15 mT. Since no simple analytic formula for the solving exists, for the solving usually a numeric computer code developed by J. Halbritter [Hal70] is used. However, for the extreme values of the material purity the contribution $\mathrm{R_{BCS}}$ to the surface resistance can be approximated by equation (2.26) [Jun12, p. 14, eq. (2.11)] for the “dirty limit“ if the mean free path before scattering $\ell << \xi_0$ and by equation (2.27) [Jun12, p. 14, eq. (2.12)] for the “clean limit“ when $\ell >> \xi_0$. [Jun12, pp. 13-14]

$$R_{BCS} = \mu_0^2\,\omega^2\,\sigma_0\,RRR \cdot \lambda(T,\ell)^3 \frac{\Delta}{k_B\,T} ln\left(\frac{\Delta}{h\,\omega}\right) \frac{e^{-\Delta/k_B\,T}}{T} \tag{2.26}$$

$$R_{BCS} \simeq \frac{3\,\Delta}{2\,k_B\,T} \mu_0^2\,\omega^2\,\sigma_0\,RRR \frac{\lambda(T,\ell)^4}{\ell} ln\left(\frac{1.2\,T\,\Delta\,\xi_0^2}{h^2\,\omega^2\,\lambda(T,\ell)^2}\right) e^{-\Delta/k_B\,T} \tag{2.27}$$

For all equations $\lambda(T,\ell)$ [Kle17, p. 14, eq. (2.24)] describes the effective penetration depth regarding the impact of the coherence length ξ_0 and the mean free path before scattering ℓ [Kle17, p. 14]:

$$\lambda(T,\ell) = \lambda_l \sqrt{1 + \frac{\xi_0}{\ell}} \tag{2.28}$$

The two fluid model as well as the BCS based expressions by Mattis and Bardeen predict zero surface resistance for $T = 0$. However, during measurements a temperature independent contribution to the residual resistance R_{res} can be observed. These residual losses are caused for example by absorbed gases like Hydrogen possibly induced during chemical polishing. The resulting surface resistance is consequently given by equation (2.29) [Kle17, p. 15 eq. (2.28)]. [Kle17, p. 15]

$$R_s = R_{BCS}(T) + R_{res} \tag{2.29}$$

Sometimes an additional parameter R_{nl} is used to model the impact of a non-linear surface resistance. Currently, no widely accepted theory exists to explain this contribution. [Jun12, p. 14]

2.5.3 The Meissner Effect

In contrast to a perfect conductor a superconducting material exposed to an external magnetic field and subsequently cooled below T_c expells the magnetic flux through its interior as soon as the transistion temperature is reached. This phenomenon is called the Meissner effect. It is caused by so called supercurrents on the surface of the conductor, shielding the magnetic field from the interior. The Meissner effect is responsible for the famous levitation phenomenon. A coin made of a superconducting material will begin to levitate above an external magnetic field when its temperature falls below T_c. This happens because the magnetic field configuration on the surface shields the magnetic field from the interior and repels the external field. [PKH08, pp. 81-83]
However, in a perfect conductor cooled down to its perfect conducting state and afterwards exposed to an external magnetic field the magnetic flux in the interior does not change since perfect shielding from external magnetic flux is implied for perfect conductivity. [PKH08, p. 81]
The behaviour of the different conductivity cases is illustrated in figure 2.6. Additionally, the behaviour of both conductivity types if the external field vanishes is shown.

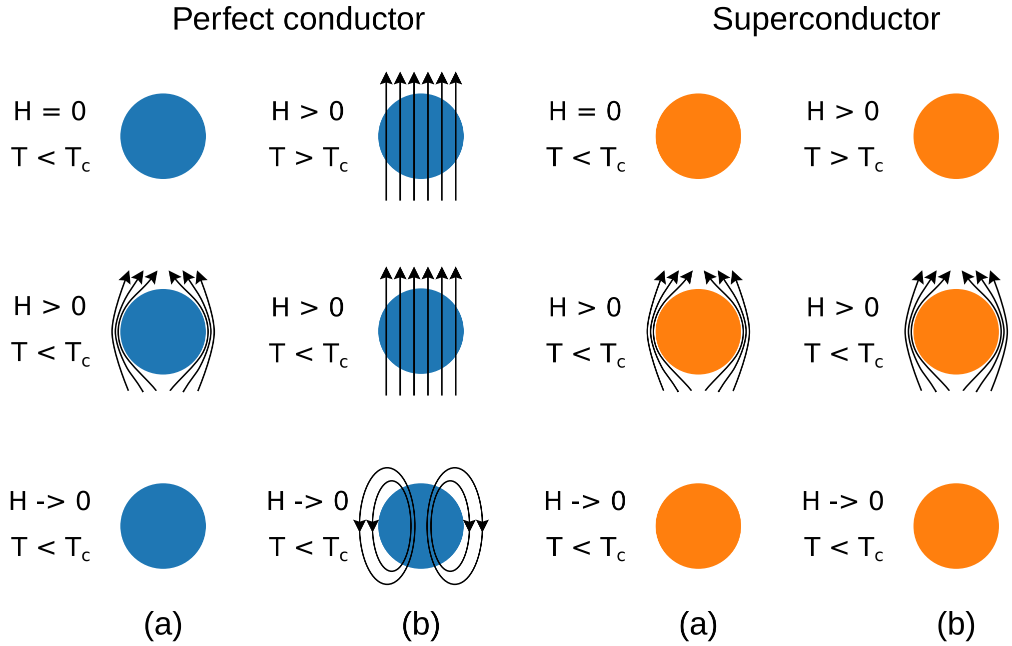

Figure 2.6: Screening of an external applied magnetic field by a perfect conductor or a superconductor (a) Trapping of the magnetic flux in the perfect conductor or rather expulsion of the flux in case of a superconductor (Meissner effect) (b). Adapted from: [Kle17, p. 11, Figure 2.2] and [PKH08, pp. 82-83, Figure 4.3/4.4]

2.5.4 Field Limitation of Superconductors

Superconducting materials lose their superconductivity at some point in the presence of a magnetic field. This point depends besides on the used material also on the geometry and the pressure. In dependence on the characteristics of the conductor above the transition temperature T_c, superconductors are distinguished into the following two types. [EH00, pp. 284-285]

Type I Superconductivity

For type I superconductors like Lead, Mercury, Indium and Aluminium the external magnetic field is shielded completely from the interior by the surrounding magnetic field of the superconductor until a critical external field magnitude B_c is reached. As soon as this point is exceeded, the superconductor immidiately becomes normal conducting as illustrated in figure 2.7a. The (negative) magnetisation of the superconductor increases until the critical field magnitude is reached and then goes down to zero. Therefore, the magnetic field density inside the conductor is given by $B_i = B_e + \mu_0\, M = 0$. Since the magnetic susceptibility $\chi = \mu_0\, M/B_e$ equals -1 a type I superconductor is an ideal diamagnet. [EH00, pp. 284-285]

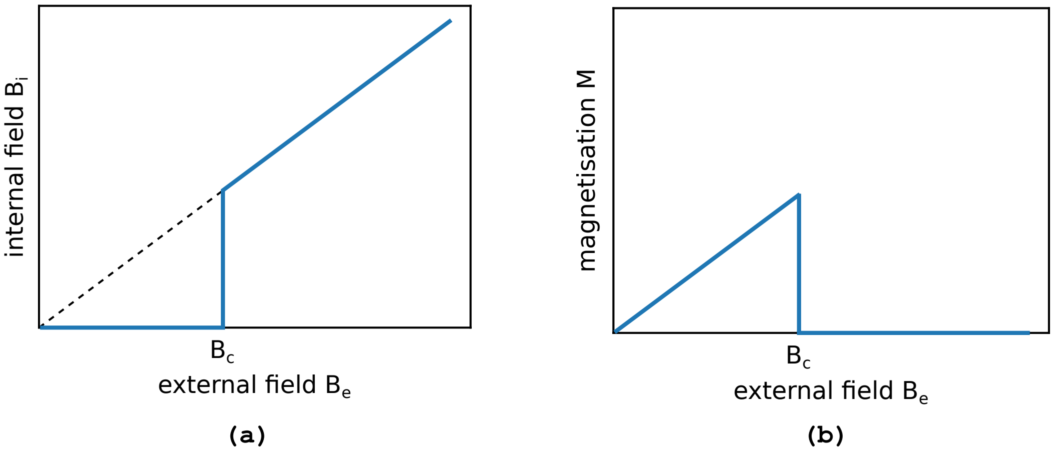

Figure 2.7: Magnetic field magnitude B_i in the interior of the (super)conductor as a function of the magnitude of an external (magnetic) field (a). Magnetisation of the (super)conductor in dependence of an external (magnetic) field (b). Adapted from: [EH00, p. 284, Abb. 10.8]

Depending on the geometry of the superconductor, the external magnetic field may ingress already partially with a linear slope starting at a point below the critical magnetic field B_c. The effective magnetic field magnitude B_{eff} is given by equation (2.30) [EH00, p. 285 eq. (10.2)] since $M \,||\, B_e$. D depicts the demagnetisation factor. [EH00, pp. 285-286]

$$B_{eff} = B_e - D\, \mu_0\, M \tag{2.30}$$

For thin disks parallel to the external magnetic field D is 0 and hence B_{eff} equals B_e. The magnetisation M for superconductors is given by $M = -B_{eff}/\mu_0$. Therfore, for a spherical superconductor with $D = 1/3$ the effective magnetic field is given by $B_{eff} = B_a/(1-D) = 3\, B_e/2$. Since $B_e < B_{eff}$ a spherical superconductor becomes normal conducting already at an external magnetic field magnitude of $B_e = 2\, B_c/3$. As soon as the superconductor becomes normal conducting the magnetic field can penetrate the conductor and B_e equals $Beff$. Consequently, the conductor becomes superconducting again. This intermediate state between superconductivity and normal conductivity for the range of $B_e = 2\, B_c/3$ to B_c is illustrated in figure 2.8. [EH00, pp. 285-286]

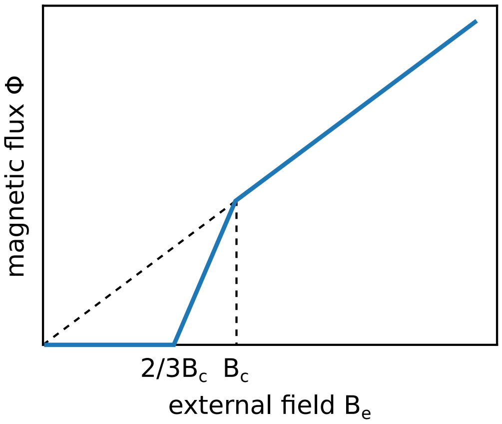

Figure 2.8: Magnetic flux in the center of a spherical supercondcutor as a function of an external magnetic field B_e. Adapted from: [EH00, p. 286, Abb. 10.10]

Type II Superconductivity

Superconductors of type II like some alloys or transition metals have two different critical magnetic field magnitudes. Above the lower critical value normal conducting flux tubes through the conductor emerge as illustrated in figure 2.9. The surrounding material stays meanwhile superconducting until an upper critical magnitude is reached and the superconductor becomes entirely normal conducting. Both field limits are temperature dependent. For some materials the magnitude of B_{c2} can be several hundred times higher then B_{c1}. The range between these two limits is known as the Shubnikov-phase. [EH00, pp. 287-289]

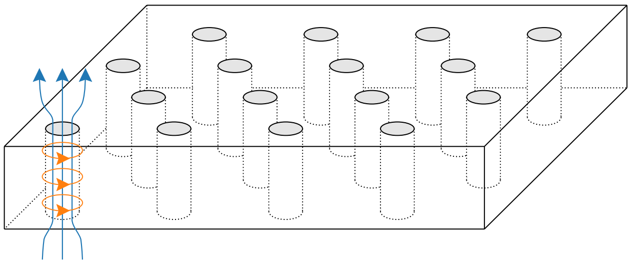

Figure 2.9: Distribution of normal conducting (gray) and superconducting regions in the Shubnikov-phase. For one of the flux tubes the distribution of the magnetic field lines (blue) and the related shielding currents (orange) is illustrated. The shown arrangement of the flux tube in perfect crystals is known as the Abrikosov-structure. Adapted from: [EH00, p. 289, Abb. 10.14]

The internal magnetic field of a type II superconductor as a function of an external magnetic field as well as the related magnetisation curve of the superconductor is illustrated in figure 2.10. Similar to type I superconductors the magnetic field cannot enter the conductor until the critical value B_{c1} is reached. However in the Shubnikov state the internal field in the superconductor increases exponentially until a saturated state is reached and the conductor becomes completely normal conducting. [EH00, pp. 287-288]

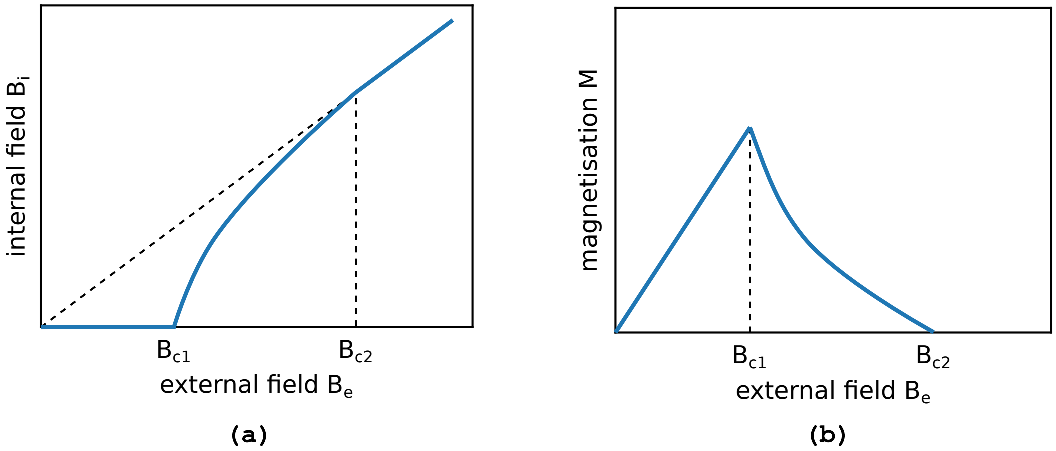

Figure 2.10: Magnetic field in a type II superconductor as a function of an external magnetic field (a). Related magnetisation M in dependence of the external magnetic field(b) (Below B_{c1} the conductor is in the Meissner state). Adapted from: [EH00, p. 288, Abb. 10.12]

2.6 Thermal Conductivity of Superconductors

Besides the electrical conductivity also the characteristics of the thermal conductivity are altered in the superconducting state. At temperatures near 0 K the thermal conductivity of superconductors is dominated by the contribution of the unbound electrons. The contribution of the phonons is negliable low in this temperature region. As mentioned in section 2.5.2 for superconductors below T_c an exponentially increasing fraction of the electrons is bound in cooper pairs. Since these cooper pairs are not affected by lattice vibrations they cannot transport thermal energy. Thus, the thermal conductivity drops sharply below T_c. However, the electron bound in cooper pairs are no longer effective for scattering of the remaining phonons. For this reason the thermal conductivity will increase again at some point for decreasing temperatures until a maximum is reached determined by the mean free path of the phonons. The scattering characteristic of the phonons depends on the crystal grain size of the material. In case of Niobium this effect can be used to generate a thermal conductivity peak near 2 K illustrated in figure 2.11. [PKH08, p. 75]

For the normal conducting state the relation between electric and thermal conductivity is described by the Wiedemann-Franz law. Based on this law the relation in 2.31 [PKH08, p. 75, eq. (3.51)] between the RRR and the thermal conductivity in the superconducting state K_s can be approximately derived. [PKH08, p. 75]

$$RRR = 4\,K_s\left[\frac{W}{m\,K}\right] \tag{2.31}$$

2.7 Surface Treatment

The RF performance of Niobium surfaces in the superconducting state can be extensively effected even by minor microscopic contaminations or scratches potentially caused during the manufactu-

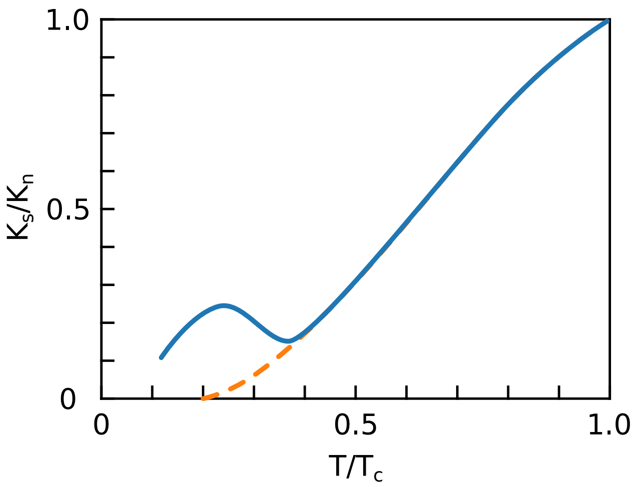

Figure 2.11: Replication of the thermal conductivity (normalised by the thermal conductivity in the normal conducting state K_n close to T_c) according to the BCS theory (orange; dashed) and of a measured Niobium sample (blue) as a function of the temperature. Addapted from: [PKH08, p. 76, Figure 3.12]

ring. These contaminations may limit the performance by magnetic heating or possible electron field emission. For this reason a set of surface treatments had been developed in the past to reduce the related limitations followed by a clean room assembly of class 10-100 to avoid a new contamination. The clean room class indicates the number of particles with a size of more than 0.5 μm per cubic foot of air. [PKH08, p. 120]

2.7.1 Etching

As a first step after the fabrication a layer of about 100 μm is removed by chemical etching (BCP). During this procedure surface damages as well as contaminations can be removed. Unfortunately by the etching process itself a Hydrogen contamination of the surface called “Q disease“ because of the related increasing surface losses may be caused. Such contaminations can be avoided by using an appropriate BCP acid solution at a temperature below 18 °C. [PKH08, pp. 120-121]

As an alternative to chemical etching the Niobium can be electropolished in a bath of sulphuric and 40 % hydroflouric acid by using the Niobium surface as the anode and a cathode made of Aluminium. This procedure provides an almost perfect surface smoothness but a longer polishing time is required in comparison to chemical etching. During the procedure a sulfur contamination of the surfaces is caused which needs to be removed by ultrasonic rinsing. Also a hydrogen contamination can not be avoided. For this reason the surface has to be annealed for several hours at 800 $°C$ under vacuum conditions. [PKH08, p. 121]

2.7.2 Rinsing

Independent of the used etching procedure the surfaces need to be rinsed by ultra pure water for a couple of hours. To allow a reusage of the water in a closed loop the rinsing water needs to be filtered to remove dissolved particles. To achive even better results sometimes the rinsing process is carried out with a high water pressure of about 100 bar. After the rinsing process the components are prepared for the clean room assembly. [PKH08, p. 121]

2.8 Antenna Coupling

For the performance tests single cell TESLA-shape cavities are used. To transmit the required power into the cavity it is connected to an input coupler mounted at one of the drift tubes. In the center of the second drift tube a so called field probe antenna is installed to measure the power transmitted through the cavity [PKH08, p. 145]. A depiction of this setup is shown in figure 2.12. In contrast to the operation in an accelerating facility during the performance test impedance matching should be ensured between the input coupler and the cavity to avoid power reflections at the input coupler. Hence, the external quality factor Q_{ext} of the input coupler needs to equal the intrinsic quality factor Q_0 of the cavity. Since the external quality factor depends on the power leaking back into the coupler if the input power is switched off, impedance matching can be achieved by varying the penetration depth of the input coupler's antenna. Due to the operation of the cavity below the cut-off frequency of the drift tube the coupling strength increases exponentially as a function of the antenna penetration depth. [PKH08, p. 146-147]

Impedance matching between the input coupler and the cavity is only established during the performance tests. For the operation in an accelerator the input coupler is extensively overcoupled to allow a power coupling also to slightly detuned cavities. Because of the low losses, superconducting cavities usually show intrinsic quality factors Q_0 in the range of 10^{10} to 10^{11}. These high quality factors are leading to a very narrow bandwidth Δf of the cavity. Therefore a phase locked loop (PLL) is required to lock and track the resonant frequency of the cavity.

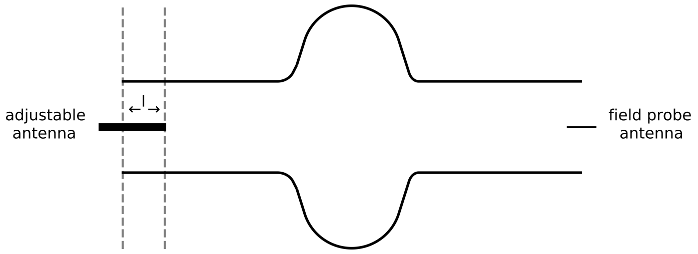

Figure 2.12: Depiction of the coupling antennas of a single cell cavity. The adjustable antenna with an adjustment range l is used for the power coupling. By means of the field probe antenna the transmitted power through the cavity can be measured.

The measurement setup of the performance tests is simplified depicted by the model in figure 2.13. To provide the required input signal an RF generator is used. By means of a circulator reflected power at the input coupler in case of an impedance mismatch is transmitted into a matched load to prevent possible damage of the RF generator. [Wan08, pp. 139-140]

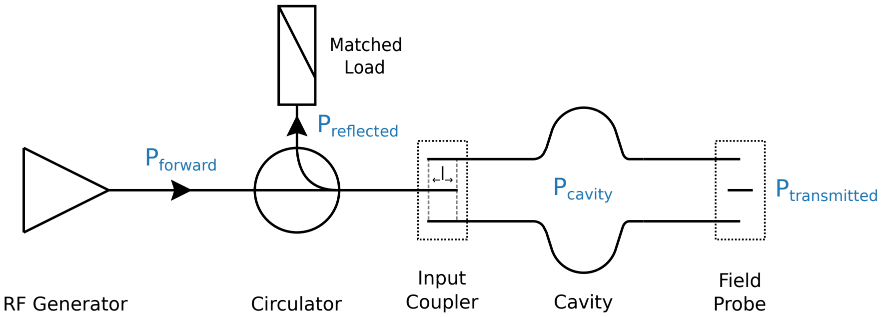

Figure 2.13: Simplified block diagram of the measurement setup. The RF generator is used to provide the input power. By means of the circulator reflected power at the input coupler in case of an impedance mismatch is transmitted into a matched load. Thereby possible damage of the RF generator can be prevented. The field probe antenna is used to measure the transmitted power through the cavity. Adapted from: [Wan08, p. 141, Figure 5.3(a)]

The behaviour of this model can be described in steady state by an equivalent circuit shown in figure 2.14a. In this circuit the RF generator is represented by an ideal current source together with an impedance $\underline{Z}_0$. Transformers are used to model the coupling characteristics of the input coupler and the field probe antenna. The cavity is represented by a lossy parallel oscillating circuit. To simplify the following calculations the oscillating circuit and the load behind the second transformer representing the field probe can be transformed into the circuit containing the current source as shown in figure 2.14b. [Wan08, pp. 139-144]

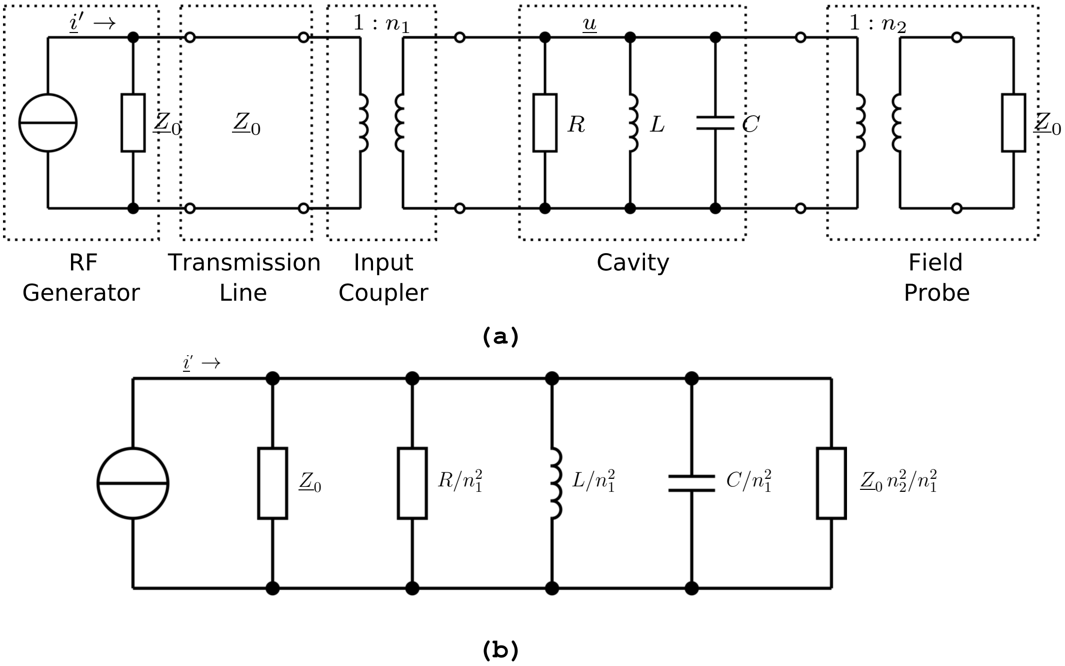

Figure 2.14: Equivalent circuit of the measurement setup in steady state. Adapted from: [Wan08, p. 144, Figure 5.6] (a). Equivalent circuit of figure 2.14a with all components transformed into the circuit representing the RF generator. Adapted from: [Wan08, p. 145, Figure 5.7] (b).

The power dissipation of the oscillating circuit in figure 2.14b (P_{cavity}) [Wan08, p. 145], the power coupling circuit (P_{ext}) and the field probe ($P_{transmitted}$) [Wan08, p. 145] in dependence on the alternating voltage $\underline{u}$ are given by:

$$P_{cavity} = \frac{n_1^2 u^2}{2\,R} \tag{2.32}$$

$$P_{ext} = \frac{u^2}{2\,\underline{Z}_0} \tag{2.33}$$

$$P_{transmitted} = \left(\frac{n_1}{n_2}\right)^2 \frac{u^2}{2\,\underline{Z}_0} \tag{2.34}$$

The stored energy W [Wan08, p. 145] in the oscillating circuit can be calculated by:

$$W = \frac{n_1^2\,C\,u^2}{2} \tag{2.35}$$

The related quality factors Q_0, Q_{ext} and Q_t can be calculated as follows [Wan08, p. 145]:

$$Q_0 = \frac{\omega_0\,W}{P_c} = \omega_0\,R\,C \tag{2.36}$$

$$Q_{ext} = \frac{\omega_0\,W}{P_{ext}} = \omega_0\,n_1^2\,\underline{Z}_0\,C \tag{2.37}$$

$$Q_t = \frac{\omega_0\,W}{P_{transmitted}} = \omega_0\,n_2^2\,\underline{Z}_0\,C \tag{2.38}$$

The total dissipated power $\mathrm{P_L}$ [Wan08, p. 145] of the cavity is given by:

$$P_L = P_{cavity} + P_{ext} + P_{transmitted} \tag{2.39}$$

The power $\mathrm{P_L}$ leads to the “loaded“ quality factor Q_L [Wan08, p. 145, eq. (5.33)] of the cavity:

$$Q_L = \frac{\omega_0\,W}{P_L} \tag{2.40}$$

The introduced Q values are related by equation (2.41) [Wan08, p. 145, eq. (5.31)]:

$$\frac{1}{Q_L} = \frac{1}{Q_0} + \frac{1}{Q_{ext}} + \frac{1}{Q_t} \tag{2.41}$$

This loaded quality factor Q_L [PKH08, p. 147, eq. (8.6)] can be determined by switching of the RF power to measure the time constant τ_L of the cavity's ring down process [PKH08, p. 147]. $\mathrm{Q_L}$ can then be calculated by:

$$Q_L = \tau_L \, \omega_0 \tag{2.42}$$

The so called coupling parameters β_{ext} [PKH08, p. 148, eq. (8.12)] for the input coupler and β_t [PKH08, p. 148, eq. (8.12)] for the field probe antenna are defined as follows [PKH08, p. 148]:

$$\beta_{ext} = \frac{Q_0}{Q_{ext}} \tag{2.43}$$

$$\beta_t = \frac{Q_0}{Q_t} \tag{2.44}$$

By inserting the expressions in equation (2.41), the intrinsic quality factor $\mathrm{Q_0}$ can be calculated by:

$$Q_0 = Q_L \, (1 + \beta_{ext} + \beta_t) \tag{2.45}$$

In case of an impedance match between the input coupler and the cavity, the reflection coefficient Γ is 0 [Wan08, p. 145, eq. (5.34)], which means, that there are no power reflections at the input coupler hence the complete forward power can be transfered into the cavity [Wan08, pp. 145-146]:

$$\Gamma = \frac{\beta_{ext} - \beta t - 1}{\beta_{ext} + \beta t + 1} \tag{2.46}$$

Due to the normally weakly coupled field probe antenna ($\beta_t << 1$) its impact on the power losses can usually be neglected [PKH08, p. 148]. For this case the reflected power $P_{reflected}$ [Wan08, p. 143, eq. (5.28)] at the input coupler is given by:

$$P_{reflected} = P_{forward} \, \Gamma^2 = P_{forward} \left(\frac{\beta_{ext} - 1}{\beta_{ext} + 1} \right)^2 \tag{2.47}$$

and the power transfered into the cavity P_{cavity} [Wan08, p. 144, eq. (5.29)]:

$$P_{cavity} = P_{forward} \, (1 - \Gamma^2) = P_{forward} \frac{4 \, \beta_{ext}}{(1 + \beta_{ext})^2} \tag{2.48}$$

3 Motivation

To minimise the drift tube length between the cavity iris and the flange, the critical RF field density of the connection area must be known. In this thesis a model to investigate the field limitation and the related minimal drift tube length of commonly used connections of 1.3 GHz TESLA-Shape cavities at DESY is implemented and tested. These connections are consisting of two flanges shown in figure 3.1a with a vacuum gasket (figure 3.1b) in between. Screws positioned symmetrically around the flanges are used to hold the connection together. To ensure ultra-high vacuum (UHV) tightness a normal conducting Aluminium gasket is used. These gaskets provide a high reliability at room temperature as well as at the operating temperature of 2 K. For the flanges a NbTi55 alloy instead of Niobium is used to provide the required material hardness. In comparison to Niobium this alloy has the disadvantage of comparatively large surface losses and a low critical flux of just about 10 mT [GHH$^+$75]. Both materials were chosen since the connection was originally designed for low field areas. Because of the normal conducting gasket and the used flange material a low field limit of the connection can be expected. For this reason, an attempt to increase the critical field by shielding the connection gap with a RF seal is investigated as well in the scope of this thesis.

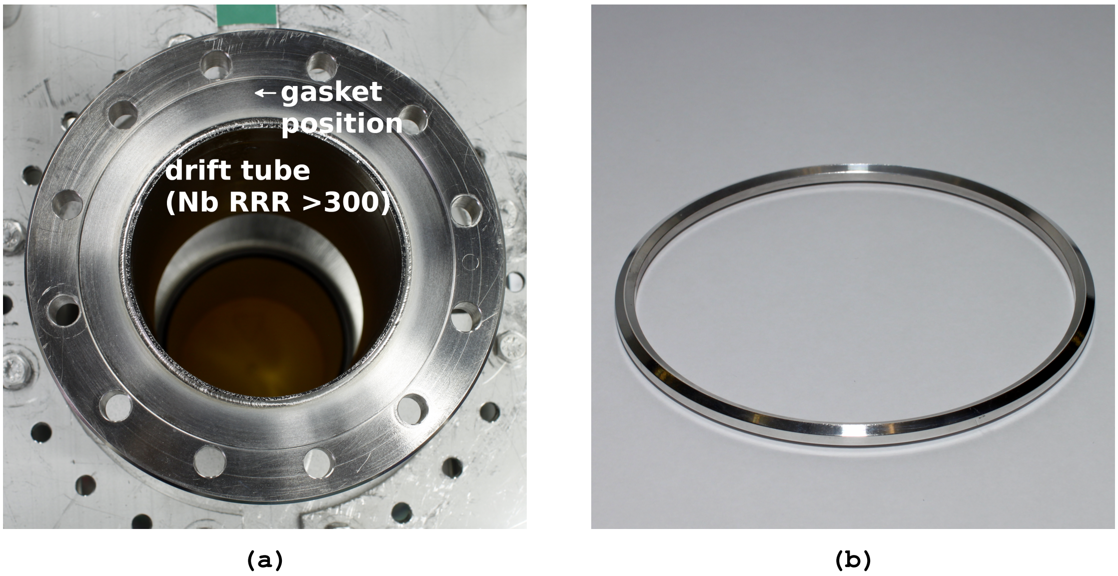

(a) (b)

Figure 3.1: Commonly used NbTi55-flange for SRF cavities at DESY (a). Aluminium vacuum gasket with high surface losses in case of an RF field exposure in comparison with superconducting Niobium (b).

To avoid any mechanical changes on the cavity used for the tests, a cylinder in the center of one of the drift tubes is used to turn it into a coaxial line. This setup is depicted in figure 3.2. By means of this modification the field density at the connection can be increased and the connection can be virtually displaced just by the field density increase. The critical field density of the connection and the related minimal drift tube length can then be found via a stepwise increase of the RF power until the breakdown occurs. The related average accelerating field will yield by a subsequent alignment with an appropriate RF simulation model to the critical magnetic field at the connection. The dimensioning and the validation of the connection displacement model in form of the cylinder insert is the target of this thesis.

3.1 Model Requirement Analysis

Besides by the critical field density of the connection, the minimal drift tube length is mechanically limited since some space is required for the flange as well as the later mounting of the connection. This mechanical limit for the drift tube length was defined to be 30 mm. To allow an investigation of the critical field density up to this limit, the cylinder insert must be able to provide the same field density in the connection area as at a connection located 30 mm away from the iris. For the development of the cylinder insert a field density twice as high as at this mechanical reference point was chosen so that also a cavity with a comparatively low gradient can be used for the later performance tests. To allow a straightforward assembly of the cylinder insert, the outer radius of the insert should be at least 10 mm lower than the inner radius of the drift tube of the cavity. The material as well as the geometry of the cylinder insert's socket flange have to be similar to the corresponding counterpart of the cavity's flange of the investigated connection type. Hence, it is fabriacated out of the NbTi55 alloy. The cylinder insert should be developed for the use in a TESLA-shape single cell cavity depicted in figure 3.2.

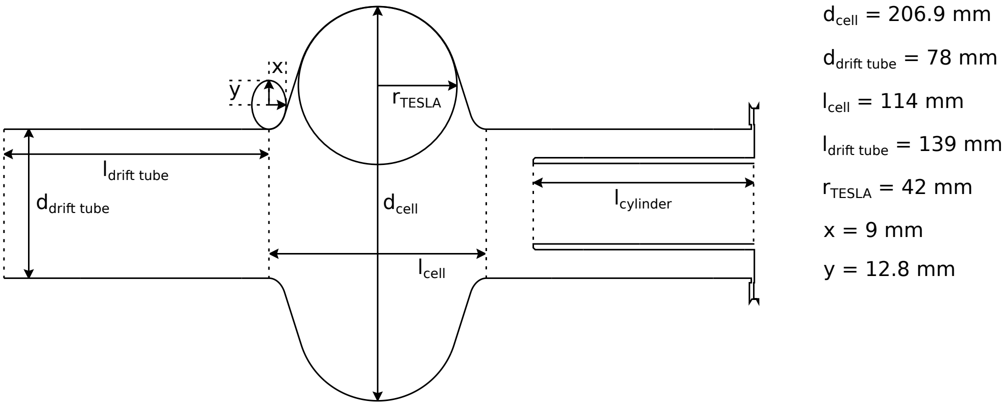

Figure 3.2: Geometry of the TESLA-shape test cavity with the mounted cylinder insert. Adapted from: [Edw95, p. 122, Figure 4.2]

To ensure that the connection displacement model realised by the afore mentioned cylinder insert maps the behaviour of an actually displaced connection correctly, the impact on the figures of merit of the test cavity have to be low. Those figures of merit are the peak surface fields E_{pk} and H_{pk}, the intrinsic quality factor Q_0, the resonant frequency $f(TM_{010})$ and the field distribution in the input coupler's drift tube as well as the cell. Furthermore, the field distribution inside the connection gap needs to be compared for the following cases. First, the so called propagation case of an actually displaced connection. Second, the virtually displaced connection by the usage of the cylinder insert.

3.2 Former Investigations

Field limitations for different vacuum gasket types and materials had been previously investigated in 1976 at the Kernforschungszentrum Karlsruhe as an attempt to develop a superconducting connection for the use in a SRF particle separator for the Conseil européen pour la recherche nucléaire (CERN). Depending on the operating mode the gaskets located on the equator of a cavity's cell had to withstand highest magnetic field magnitudes without a significant decrease of the quality factor. Ring-shaped gaskets made of Niobium or Lead have been tested, but showed either high losses or caused grooves on the connection surfaces. At last, a design shown in figure 3.3 separating the functions of the RF-contacting and the UHV-tightness was successfully tested at a magnetic flux of $3 - 5\,\mathrm{mT}$ [KCS+07]. A good RF contact have been established by special shaped “lips“ to break through the oxyde layer of the connection surfaces during the mounting process. UHV-tightness was ensured by Indium wires between each flange and the Niobium gasket. Additionally UHV-tightness had to be warranted at room temperature as well as at $2\,\mathrm{K}$ in a superfluid Helium environment.[GLR77]

Later attempts for connections able to withstand a magnetic flux of up to $30\,\mathrm{mT}$ (for the use in a superstructure configuration) have been developed at DESY and Jefferson Lab. Since commonly used NbTi55 (according to XFEL specification [XFE10]) flanges have a low critcal flux of about $10\,\mathrm{mT}$ [GHH+75] and a comparatively low thermal conductivity of about $0.05\,\mathrm{W\,m^{-1}\,K^{-1}}$ [Col86] a Nb-1Zr alloy had been considered for the flanges together with a vacuum gasket made of ultra pure Niobium to realise the connection. [KCS+07, BCS+99]

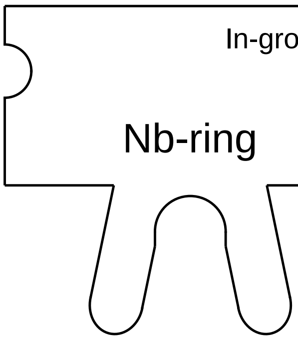

Figure 3.3: Depiction of a cut of a circular superconducting gasket for the use in a SRF particle separator. The gasket is combining the functionality of a vacuum gasket and a RF seal. UHV-tightness is ensured by Indium wires located in the grooves on both sides of the gasket. To ensure a good RF contact special shaped “lips“ to scratch through the oxide layer during the mounting process are used. Adapted from: [GLR77, Fig. 3]

4 Development of the Cylinder Insert

Within this chapter first the development process of the cylinder insert to fullfill the requirements listed in section 3.1 is described. Afterwards the dimensioning of the connection displacement model in form of the cylinder insert is compared by RF simulations to a model of an actually displaced connection. This validation is performed to ensure that a connection displacement can be mapped by the dimensioned model within an acceptable uncertainty. Finally, the manufacturing of the cylinder insert for the following performance tests is outlined.

4.1 Selection of the RF Simulation Software

Due to the axial symmetry, a 2D code is used for the development of the cylinder insert. The usage of a 2D code enables the possibility of a high resoluting mesh and a simultaneously low computation time. For this application the Poisson Superfish collection of programs[1] of the Los Alamos Accelerator Code Group (LAACG) is chosen because of the wide dispersion and the comprehensive documentation.

This collection of programs can be used for the computation of 2D static electric and magnetic field (Poisson) or RF field problems (Superfish) [LAA]. Both programs are using a triangular mesh in either cartesian or axially symetric cylindrical coordinates [LAA]. Additionally, Superfish is able to compute the surface losses of superconducting materials. This capability is important for the investigation of a possible degradation of the quality factor Q_0 investigated in section 4.7. The fine mesh of $\sim 0.33\,\text{mm}$ per mesh cell enables a precise evaluation of the field distribution in fine geometry structures like the connection gap illustrated in the magnification in figure 4.1. A detailed documentation of the Poisson Superfish collection of programs can be found in: [BY06].

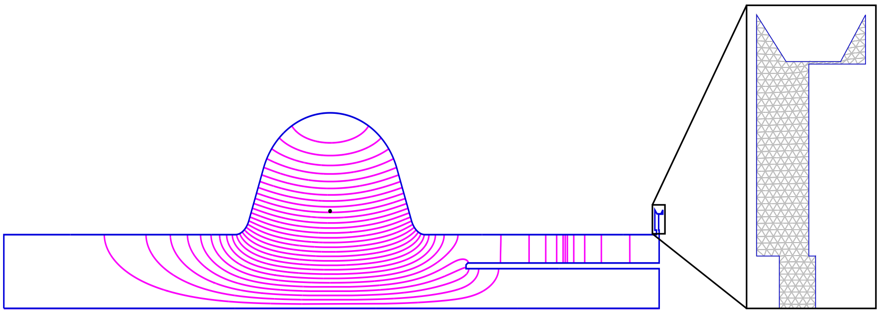

Figure 4.1: Superfish simulation model of a single cell cavity with the mounted cylinder insert. In the magnification the connection gap is shown to illustrate the mesh cell distribution.

---

[1] LAACG Poisson Superfish: `https://laacg.lanl.gov/laacg/services/download_sf.phtml`

4.2 Influence of the Connection Gap Width

Divergent to the commonly used connection design (CUCD) for SRF cavites at DESY, a larger gap width of 1.3 mm must be implemented to enable the later usage of the RF seal without any changes on the insert's flange. Independent from the connection design, the real gap width may deviate from the theoretical value due to a varying torque used to tighten the connection screws and the associated pressure on the vacuum gasket. The gap width describes the width, that is free for the whole radial range from the gap entrance on the level of the inner drift tube diameter to the vacuum gasket. Since the CUCD has a gap width of theoretically 0.7 mm an impact on the field magnitude along the gap needs to be investigated to ensure that the caused deviation by the larger gap width is within a tolerable range ($< 20\,\%$). For this investigation at both connection types the field distribution is simulated for the case of an empty drift tube and a distance between the cavity flange and the iris of 30 mm. The radial field distribution along the gap is evaluated following a "field evaluation line" in the center of the adapted insert connection design (AICD) 30.65 mm afar from the iris. For the case of the CUCD this results in a field evaluation close to the second wall of the connection with only a distance of 0.05 mm. Since it can be shown that the distance to the walls has only a minor impact on the magnetic field magnitude along the gap (in section 4.10.2), the radial field evaluation at the same distance to the iris is considered to be the more important criteria. For both simulation models the drift tube with the associated connection together with a magnification of the connection gap and the "field evaluation lines" are shown in figure 4.2.

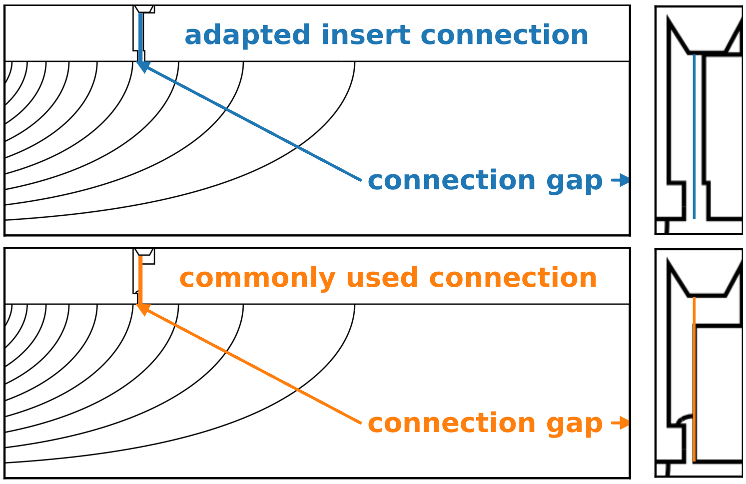

Figure 4.2: Sections of the used SF simulation models to illustrate the position of the field evaluation lines used for the comparison of the field distribution along the connection gap.

The recorded field magnitudes along the "field evaluation lines" are plotted in figure 4.3. They are normalised by the maximum value of the evaluated magnitudes of the CUCD. Because of the non-linearity of the CUCD close to the gap entrance described in detail in section 4.10.2, only the area with a radial distance from the axis greater than 42 mm is used for the evaluation. For this interval the recorded values were fitted to the linear function by the Python method `numpy.polyfit()` of the `numpy` library. For the CUCD the function: $f_{CUCD}(x) = -0.014327\,x + 1.595336$ is computed and for the AICD: $f_{AICD}(x) = -0.015668\,x + 1.590760$. The relative error of the mean distance between the two functions of the evaluated interval is 7.06 % by using the CUCD as the reference.

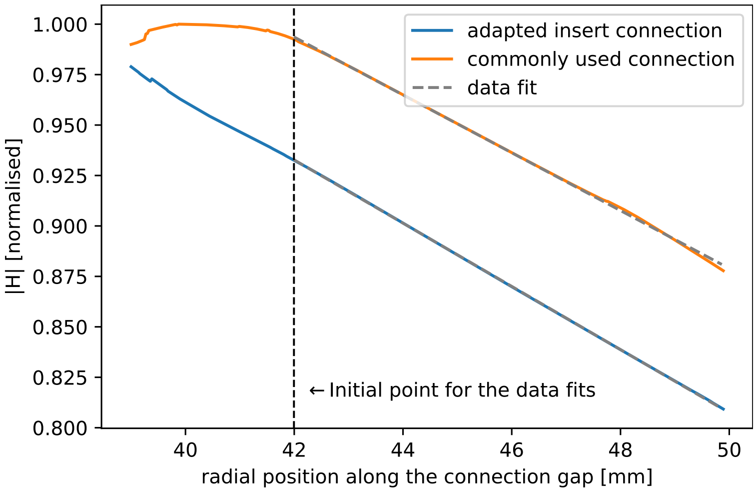

Figure 4.3: Comparison of the radial decay of the magnetic field along the connection gap of the commonly used connection (CUCD) and the connection design adapted for the use of the RF seal (AICD).

Furthermore, the proportional losses at the surface of the vacuum gasket are compared. Since the Aluminium vacuum gasket is normal conducting it can be expected, that it is the field limitting element of the connection area because its losses warm the surrounding superconducting flanges. Therefore, a comparison of the simulated surface losses at the gasket between both connection types can serve as a good indicator for the usability of the AICD. For the comparison both fractions are normalised by the total power losses of the respective simulation model. For the CUCD a material independent fraction of the losses of $1.43 \cdot 10^6$ and for the AICD of $1.31 \cdot 10^6$ is simulated by Superfish. This yields to a relative deviation between both designs of 8.82 % by using the CUCD as the reference.

4.3 Automisation of a Stepwise Cylinder Length Increase

To find the minimal required length of the cylinder insert to provide the desired field magnitudes at the connection gap, the cylinder insert's length can be increased stepwise for a defined range in a simulation series. For each simulation the absolute values of the RF field components at the evaluation point in the center of the connection gap entrance marked in figure 4.4 as well as the resonance frequency of the setup have to be recorded. By a subsequent alignment of the evaluated field data with the magnitudes in a simulation model of an actually displaced connection, the minimal required cylinder length can be found. Furthermore, the sensitivity of the insert to length deviations and possible resonances close to the operating frequency (1.3 GHz) of the cavity in the affected drift tube can be investigated by this simulation series. Since Superfish does not provide an appropriate method for the simulation series, this task is automised by an external C-program. This program is developed to run on Linux based operating systems. For this purpose some kind of emulation or translation software is needed to run the Superfish codes designed for Microsoft

Windows on a Linux system. For this task the WineHQ project[2] is used. The sequence of the program is ilustrated in figure 4.5. External operations are marked in color to provide a clean view on the functionality. Operations executed without a translation of WineHQ are highlighted in blue the remaining ones in orange. For executions of external software, the function `system()` of the library `stdlib.h` is used to ensure the main program pauses until the execution of the external part is finished. For the simulation the program Autofish is used. Autofish combines the execution of the mesh generator Automesh the RF solver Fish as well as the postprocessor SFO [BY06, pp. 147-148 (SFCODES.DOC)]. By starting at the lowest cylinder length of the defined range, the program first deletes potentially present old Autofish simulation results [*.SFO].

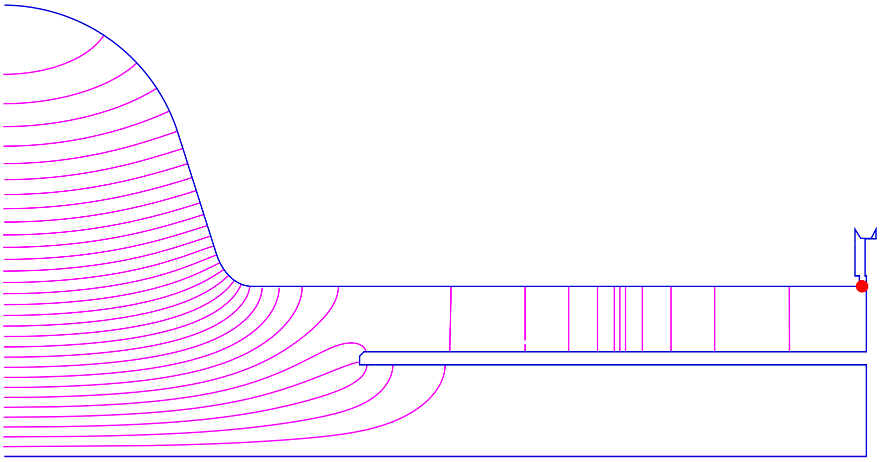

Figure 4.4: Section of a Superfish simulation model of a single cell cavity with the mounted cylinder insert to illustrate the position of the field evaluation point (red) in the center of the connection gap entrance.

They are deleted and not only overwritten to detect possibly failed simulation steps. In case of a failed simulation and therefore missing simulation results, the event of missing result files would yield to an error message during the data evaluation. Simulations may potentially fail since the mesh generator sometimes has problems of mapping geometry components in the range of the dimensions of the mesh cells. An obvious attempt to solve this issue is to decrease the dimensions of the mesh cells and thereby increase the total number of cells. Unfortunately, this approach is limited by a maximal number of cells before Autofish aborts the simulation. Without a deletion an aborted simulation would yield to an evaluation of old results. Afterwards a simulation model [.af] with the current cylinder geometry is generated followed by an execution of Autofish.

When the simulation is finished, old results of the evaluation software SF7 are deleted since new results would be named with an additional increasing number at the end of the filename.

---

[2] Website of the WineHQ project: https://www.winehq.org/

This would yield again to evaluation of old results. Subsequently, SF7 is executed for the evaluation of the field distribution in the Autofish results. The necessary commands for the SF7 data evaluation have to be predefined in an external file. For the given application, the file contains the position of the field evaluation point in the center of the connection gap entrance. Finally, the results of the Autofish and the SF7 field evaluation are read out to be exported for a following visualisation. The resonance frequency is stored in the .SFO-file generated by Autofish. The magnitude of the electric and the magnetic field of the field evaluation point are stored in the SF7 result files [.TBL]. Afterwards, the cylinder length is increased and the described sequence starts again until the upper range limit is reached. This stepwise increase until the limit is reached is represented by the control variable “i“ in the flowchart. By default the step width is integer but it can be reduced by the use of a downscaling factor. The source code of the developed C-program is enclosed on the CD in the appendix. With the help of the developed C-program, potential additional resonances in the drift tube of the cylinder insert are investigated. For this, a stepwise cylinder length increase is simulated for the range from 0 mm to 140 mm with a step width of 0.05 mm. The recorded values for the field magnitudes at the evaluation point and the resonant frequency of the cavity are plotted in figure 4.6 as a function of the cylinder length. For all parameters the absolute values normalised to the maximum value of the simulated range are plotted. By this simulation series one additional resonance at the operating frequency of the cavity was found for a cylinder length of 44.64 mm. The field distribution in the setup for this cylinder length is shown in figure 4.7a together with the distribution of a 50 mm long cylinder insert in figure 4.7b for a comparison. This resonance is uncritical for the given application as long as the used cylinder length is differing enough from the length related to this resonance. As visible in the plots, the field magnitudes in the connection gap are insensitive to minor length deviations. This is important for a practical usage of this model. The required cylinder length to provide a field magnitude at the connection gap twice as large as at the actually displaced connection is found by a second C-program described in the following section.

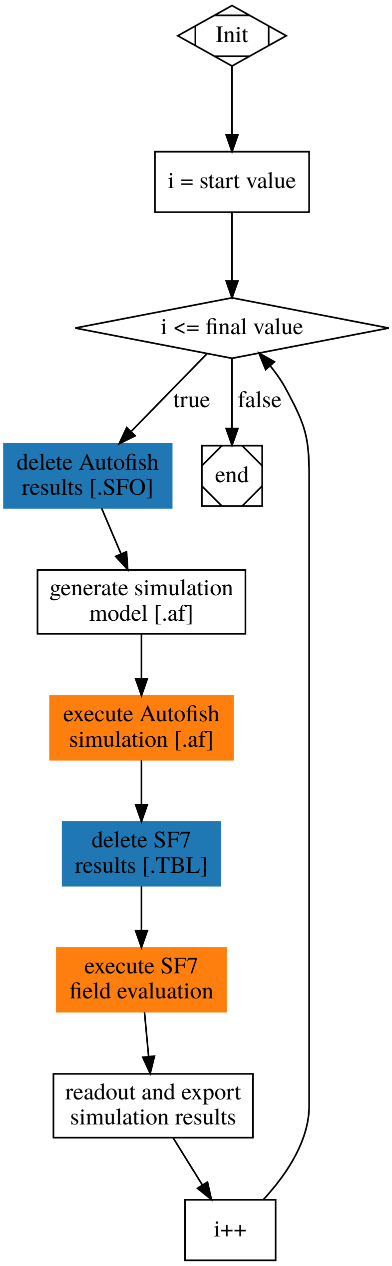

Figure 4.5: Flowchart of the automised simulation series for a stepwise cylinder length increase.

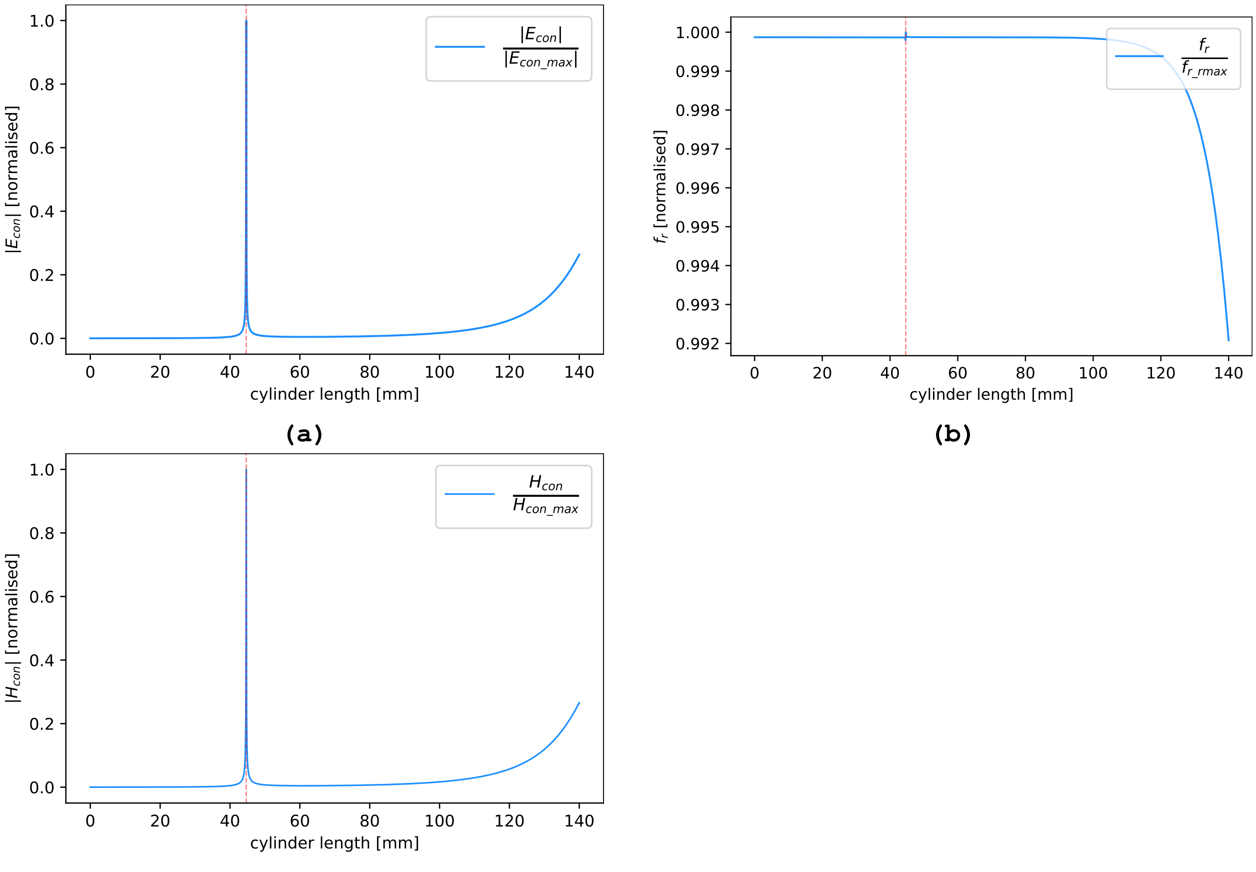

(a) **(b)** **(c)**

Figure 4.6: Absolute value of the electric field magnitude at the connection gap entrance E_{con} as a function of the cylinder length (a). Resonance frequency f_r as a function of the cylinder length (b). Absolute value of the magnetic field magnitude at the connection gap entrance H_{con} as a function of the cylinder length (c). All values are normalised by the maximum value of the simulated range.

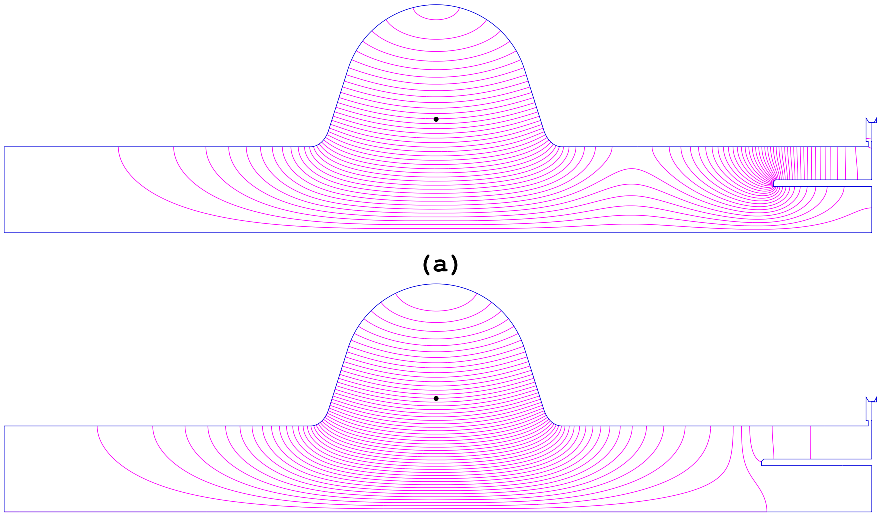

(a) **(b)**

Figure 4.7: Electric field distribution of the second resonance in the drift tube at 1.3 GHz for a cylinder length of 44.64 mm (a). For comparison the distribution for a cylinder with a length of 50 mm (b).

4.4 Optimisation of the Cylinder Length

For a precise adjustment of the cylinder length to the desired field magnitude in the connection area an optimisation algorithm is required. Since Superfish does not provide the possibility of optimisation for this kind of geometry the bisection method is implemented in an external C-program. In principle both field components can limit the field magnitude in the connection area. The magnetic causing surface losses and the electric field component by possible multipacting. The requirement to provide a field density in the connection area twice as large as in an actually displaced connection to the mechanical limit can only be fulfilled for one of the field components. This is the case because of the differences of the field distribution in a coaxial line and an empty drift tube driven below its cut-off frequency. For the given case, the magnetic field component is considered to be the more critical factor. Therefore, the magnetic field magnitude in the center of the gap entrance of an actually displaced connection is evaluated by the model shown in figure 4.9 to serve as the reference value for the optimisation. For the applicability of the bisection method the related cylinder length to the desired field magnitude must be inside of a predefined interval. This interval will then be iteratively bisected. At which after each bisection the interval half containing the searched length is defined as the new interval for the next bisection. The iteration stops as soon as the size of the interval satisfies a predifined error tolerance [MR91, pp. 786-787].

The bisection method is implemented as follows. Once initialised, the program starts an infinity loop in which first the related cylinder length of the next bisection of the current interval is calculated. Based on this cylinder geometry afterwards a new simulation model is generated. In the next step similar to the program for an automised cylinder length increase in section 4.3 old simulation results are deleted for a possible detection of failed simulations. Subsequently, Autofish is executed followed by a deletion of the SF7 results and a field evaluation by SF7. Finally, the results are read out and the relative error of the current value is calculated. The correct interval half for the next cycle is selected by a comparison of the current

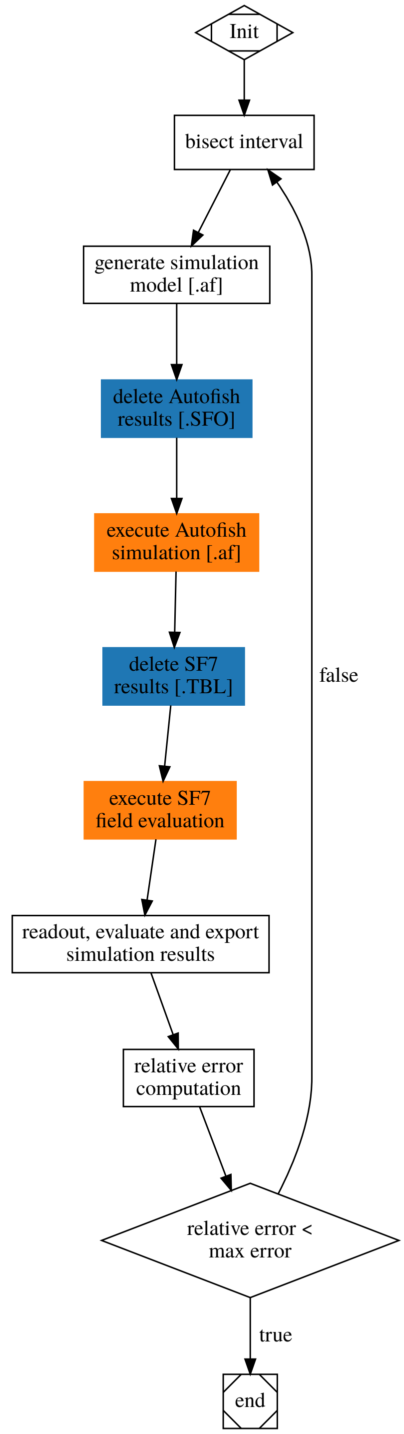

Figure 4.8: Flowchart of the cylinder length optimisation process.

evaluated field magnitude with the reference magnetic field magnitude. If the current magnitude is smaller then the reference magnitude, the point of the interval bisection is assigned as the lower boundary point. Otherwise the point of the bisection is assigned to the upper boundary point of the interval. Afterwards the next cycle is started or the infinity loop is aborted in case the predefined error tolerance is satisfied. The source code of the developed C-program is enclosed on the CD in the appendix. A flowchart illustrating the implementation of the cylinder length optimisation by the bisection method is shown in figure 4.8. Again, external executed operations without a translation of WineHQ are highlighted in blue and the remaining ones in orange. The needed interval boundaries can be chosen on basis of the results for the stepwise cylinder length increase. Due to the large slope of the field density the position of the second resonance a practical usage of this resonance for a defined field magnitude at the connection gap is not possible. Therefore this resonance should be outside of the chosen interval boundaries. By this C-program an optimal cylinder length of 115.98 mm was found to provide the desired magnetic field magnitude in the center of the connection gap entrance marked in figure 4.4. Additionally, the program was used to find the cylinder length required to provide the same magnitude as at the reference connection position. In this case a cylinder length of 104.75 mm is needed. The second length is used for comparisons between both designs in the following sections to detect potential advantages of a shorter version of the cylinder insert.

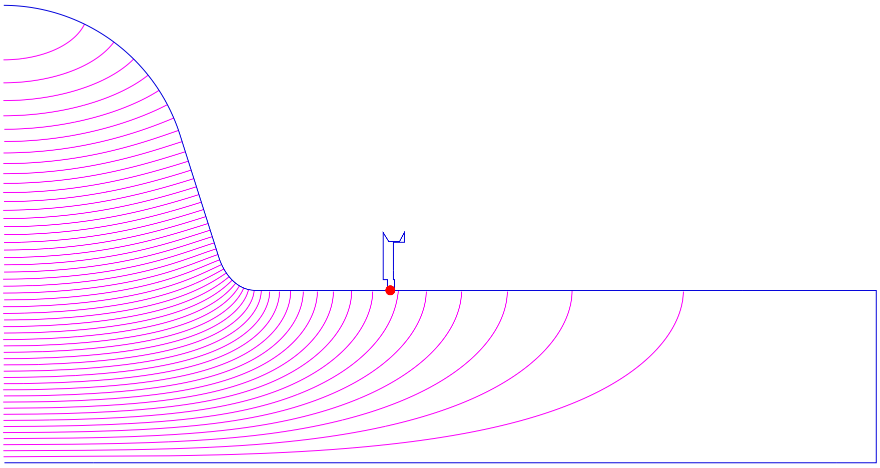

Figure 4.9: Section of a Superfish simulation model of an actually displaced connection to illustrate the position of the field evaluation point (red) in the center of the connection gap entrance.

4.5 Selection of the Cylinder Diameter

The selection of the cylinder insert's diameter depends on several factors. To allow a simple mounting process without risking scratches on the inner surface of the drift tube in case of a contact with the insert, the diameter should not be to close to the inner diameter of the drift tube. The radius difference of the insert and the drift tube is also important since the impact of minor geometry deviations of the cylinder's center point or the angle (see section 4.12) would increase. On the other hand, the possibility of a later upgrade to a double-walled and thereby actively Helium cooled version should be preserved, which requires a comparatively large diameter. Both mentioned problems in conjunction with a large cylinder diameter are less profound if they come with the benefit of an extensive possible length reduction. This is investigated by using the program for the cylinder length optimisation for the diameters 20, 24 and 28 mm. The results of this investigation are listed in table 4.1. Due to the marginal length differences an outer diameter of 24 mm is chosen as a compromise between the mentioned requirements.

Table 4.1: Required cylinder lengths in dependence of the diameter to provide a magnetic field magnitude twice as large as at the reference field evaluation point.

inner diameter	**outer diameter**	**cylinder length**
17.00 mm	20.00 mm	117.16 mm
21.00 mm	24.00 mm	115.98 mm
25.00 mm	28.00 mm	115.49 mm

4.6 Field Magnitude Conversion

During the performance tests, a direct measurement of the magnetic field magnitude at the connection gap is not possible. For this reason, the field magnitude is determined on basis of the measured average accelerating electric field $\mathrm{E_{acc\_meas}}$ by means of an alignment with an appropriate simulation model as follows. First, the average accelerating electric field $\mathrm{E_{acc\_sim}}$ given by the integral:

$$E_{acc} = \frac{1}{l_{cell}} \int_0^{lcell} E_z(z)\ cos(\phi) dz, \qquad \text{where } \phi = \frac{\omega_0 \cdot z}{c_0} - \phi_0 \tag{4.1}$$

needs to be computed for the simulation model. $E_z(z)$ plotted in figure 4.10a corresponds to the amplitude of the electric field along the z-axis of the cavity, which is evaluated along the “field evaluation line$_1$“ in figure 4.10b. The offset ϕ_0 represents the time an accelerated electron bunch needs for the distance between the flange and the center of the cell to experience the maximum possible acceleration under the simplified assumption the electron travels with the vacuum speed of light $\mathrm{c_0}$.

For the evaluated electric field magnitudes along the “field evaluation line$_1$“, E_{acc_sim} is computed with the Python function `np.trapz` of the `numpy` library.
For the used model, with a stored energy in the setup W of 48.7 mJ, a value of 2.03 MV/m is computed for E_{acc_sim}. The following analysis can be simplified by operating with a factor k defined in equation (4.2). Both, the average accelerating electric field E_{acc_sim} and the maximal electric field in the center of the cavity's cell depend on the stored energy in the cavity. Therefore the factor k does not depend on the normalisation.

$$k = \frac{E_{max}}{E_{acc}} \tag{4.2}$$

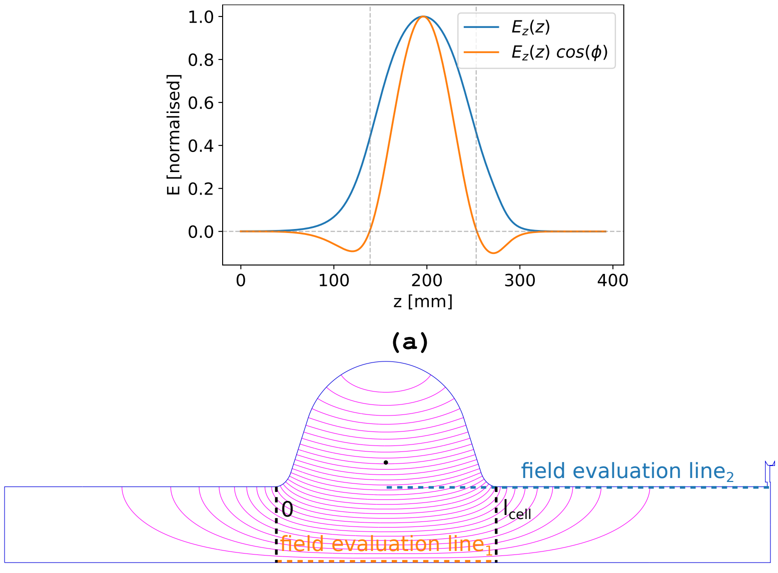

(a)

(b)

Figure 4.10: $E_z(z)$ equates the electric field distribution along the z-axis of the cavity. The product $E_z(z)\, cos(\phi)$ corresponds to the effective electric field from the perspective of an electron bunch synchronised to the phase traveling through the cavity. The grey dashed lines illustrate the evaluation range for the computation of E_{acc_sim} (a). Positions of the “field evaluation lines“ in the used Superfish model (b).

For the used model a value for E_{max_sim} of 3.55 MV/m is evaluated. Hence, a factor k of 1.75 can be calculated. Within the given accuracy k is independent of the presence of the cylinder in the model shown in figure 4.10b. By means of the factor k the value of E_{max_meas} can be calculated during the performance tests. Finally the critical magnetic field density in the centre of the gap entrance H_{con} can be calculated by the relation in equation (4.3) with the help of a second factor p. In the given case p equals $1.368 \cdot 10^{-4}\,\Omega^{-1}$).

$$H_{con}[A/m] = E_{max}[V/m] \cdot p[\Omega^{-1}] \tag{4.3}$$

The dependence of the maximal electric field magnitude E_{max} and the magnetic field magnitude at the connection gap H_{con} as well as the magnetic flux B_{con} is shown in figure 4.11a. The minimal distance between the iris and the connection gap ($l_{drift\ tube}$) can be found by an iterativ comparison of p with the particular element of an array containing the magnetic field magnitudes evaluated along the “field evaluation line$_2$“ in figure 4.10b normalised by the product of $1/E_{max\_sim}$ and the ratio $E_{breakdown}/E_{max\_meas}$. Whereat $\mathrm{E_{breakdown}}$ equates the maximum possible E-field magnitude of the test cavity depending on the individual gradient. For the given case and a known value $\mathrm{E_{breakdown}}$ the minimal drift tube length can be read from the plot in figure 4.11b.

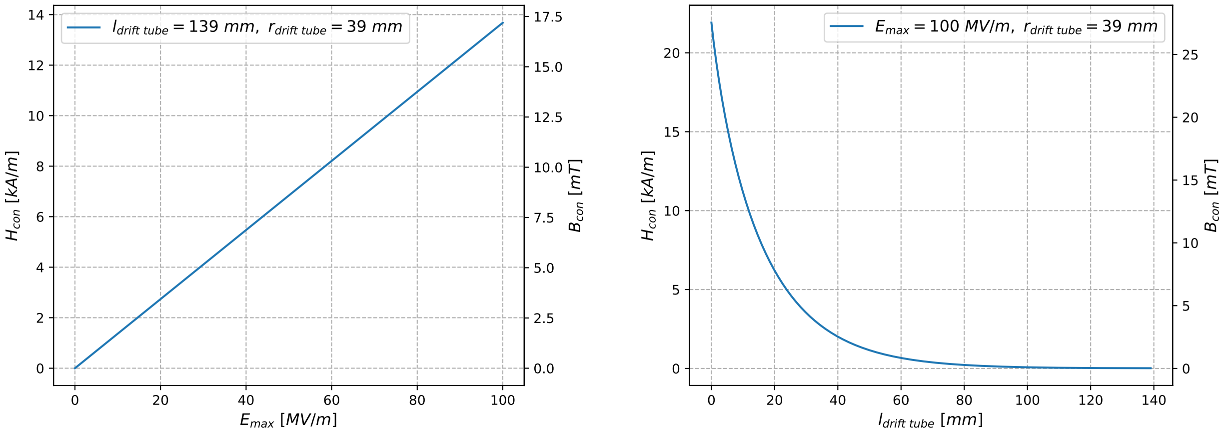

(a) **(b)**

Figure 4.11: H_{con} as a function of E_{max} plotted to visualise the relation between the maximal electric field in the centre of the cavity's cell and the magnetic field magnitude at the connection gap H_{con} (a). H_{con} as a function of $l_{drift\ tube}$ to illustrate the dependence between the magnetic field magnitude at the connection and the drift tube length $l_{drift\ tube}$ (b).

4.7 Investigation of a Possible Q_0 Degradation

An increasing field density at the normal conducting Aluminium vacuum gasket as well as the affected drift tube and the cylinder insert may extensively reduce the intrinsic quality factor of the setup. If this quality factor decrease expells the adjustment range of the input coupler's antenna it would become impossible to ensure impedance matching. Since the maximal power $P_{forward}$ of the performance test stand is limited, it may not be possible to reach the critical field magnitude of the test cavity because of a too high fraction of reflected power at the input coupler. Also, the coupling of the field probe antenna would be to low. This would yield to a decreased signal-to-noise ratio (SNR) of the measured signal and hence a larger measurement error. To prevent these problems during the performance tests, the quality factor degradation is investigated by Superfish simulations for the following cases. To validate the plausibility of the simulated quality factors a model of an empty single cell is used. The computed quality factor of this reference model can then be compared to measurements carried out earlier. A model of the same cavity with the mounted cylinder insert should represent the performance test measurement of an unshielded connection gap. By removing the connection gap the case of a perfectly shielded gap by the RF seal should be mapped. The Superfish models for the three cases are shown in figure 4.12.

4.7.1 Determinition of the Surface Resistances

To simulate the quality factor of the models, the surface losses at the particular model segments are computed. For this computation the surface resistance of each used material is required. Depending on the conductivity type (normal or superconducting) and the particular available parameters they were seperately determined as discribed in the following.

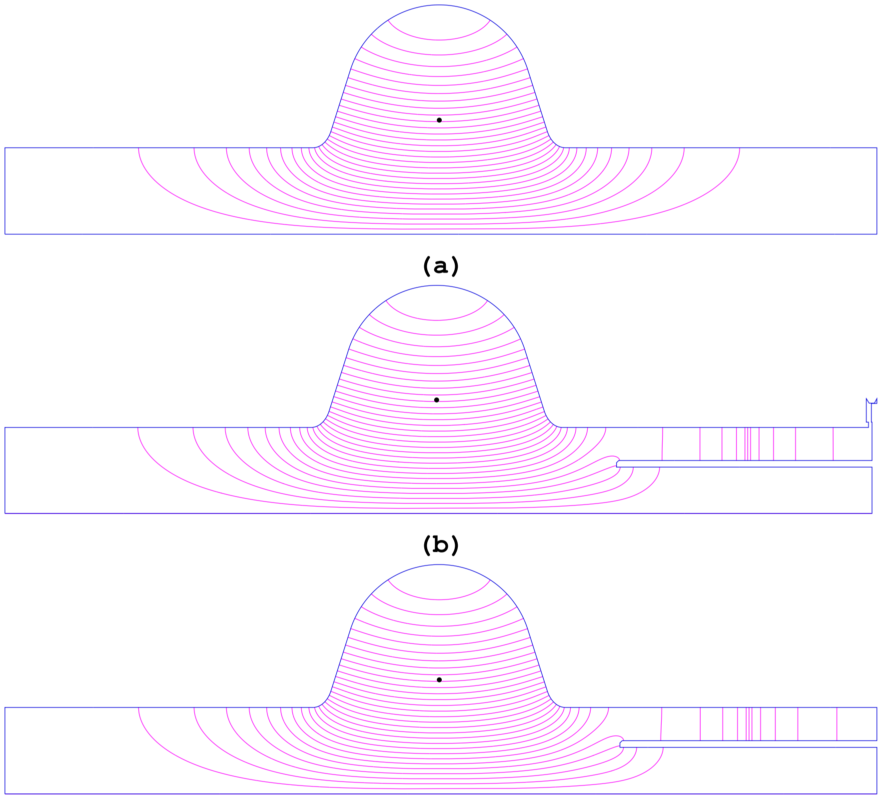

(a)

(b)

(c)

Figure 4.12: Superfish simulation models: Empty single cell cavity to validate the plausibility of the computed quality factors by a comparison with an old measurement (a); Single cell cavity with the mounted cylinder insert and an unshielded connection gap (b); The same model as in (b) without the connection gap to represent a perfectly shielded gap area (c).

Niobium Surfaces

In the measurement setup the single cell cavity and cylinder insert except its flange are fabricated out of Niobium. Although the cavity is made out of Niobium with two different purities. According to the manufacturer for the cell an ingot with a RRR of 374 was used. The drift tube has a RRR $\geq$ 300 and the cylinder of 47. For the computation of the surface resistances an adaption of the Halbritter code [Hal70] by Hunter Swan [Swa] named SRIMP from Cornell University is used. Unfortunately, the required values for the coherence length, the London penetration depth the energy of the superconducting gap and the mean free path ℓ of the used ingots are unknown. For this reason the default values of SRIMP associated to a Niobium sample with a RRR of 200 and a temperature of 2 K are used under the assumption that the deviations are low. By SRIMP the following surfaces resistances in dependence on the specific RRR value were computed:

- Nb ($RRR = 374$): 19.467 nΩ,
- Nb ($RRR = 300$): 19.041 nΩ,
- Nb ($RRR = 47$): 13.944 nΩ.

NbTi55 Surfaces

In case of the NbTi55 alloy used for the flanges appropriate measurement data are not available for all required parameters for the SRIMP computation. The coherence length, the London penetration depth, the energy of the superconducting gap and the electron mean free path remain unknown.
For this reason the Piel semi-empirical formula 4.4 [BY06, p. 33 (SFPOSTP.DOX)], an approximation to calculate the surface resistance provided by Superfish is used. This formula can estimate the surface resistance in the superconducting state on basis of the residual resistance and the transistion temperature $\mathrm{T_c}$. [BY06, p. 33 (SFPOSTP.DOX)]

$$R_s[\Omega] \approx 9 \cdot 10^{-5} \frac{f^2(GHz)}{T} e^{-1.83\, T_c/T} \cdot \Omega\, K + R_{residual} \tag{4.4}$$

For the calculation of the surface resistance the specific resistivity of the flange material was measured as a function of the temperature for a range from 298.71 K down to 7.65 K. The measurement was done by A. Ermakov from DESY. The results of this measurement are plotted in figure 4.13.

According to [Wan08, p. 418] the residual resistance is defined as the specific resistivity at 4.2 K in the normal conducting state. Since the needed value at 4.2 K is below the transition temperature of $\sim 9.2\, K$ the measurement points above the transition temperature are fitted to the linear equation. By means of the resulting function $f_{NbTi55} = 8.5678 \cdot 10^{-11}\, x + 5.3453 \cdot 10^{-7}$ a specific resistivity of $\rho_{4.2K} = 5.3489 \cdot 10^{-7}\, \Omega\, m$ can be derived for $T = 4.2\,\mathrm{K}$. By means of equation (4.4) the surface resistance R_s is given by:

$$R_s \approx 9 \cdot 10^{-5} \frac{1.3^2}{2} e^{-1.83 \cdot 9.2/2} \cdot \Omega\, K + 1.3478 \cdot 10^{-11}\, \Omega = 551.7\,\mathrm{n\Omega} \tag{4.5}$$

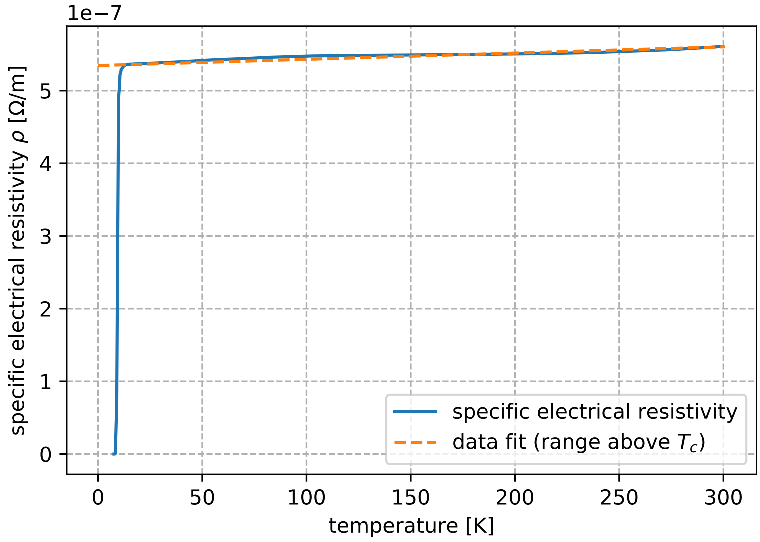

Figure 4.13: Specific resistivity ρ of the NbTi55 alloy used for the flanges as a function of the temperature.

Aluminium Surfaces

To calculate the surface resistance of the Aluminium gasket for a sample of it the specific resistivity was measured in the range from 300.115 K down to 4.233 K by A. Ermakov from DESY. The results of the measurement are shown in figure 4.14.

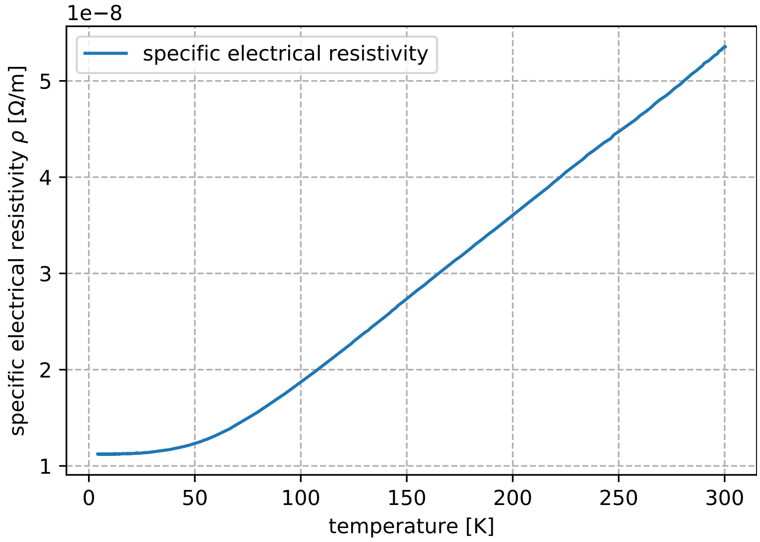

Figure 4.14: Specific resistivity σ of the AlMgSi alloy used for the vacuum gaskets as a function of the temperature.

To decide the applicable form of the skin effect in dependence of the mean free path before an electron will be scattered the RRR of the sample is required. For the given measurement results this leads to a RRR of 4.656. Due to the low RRR the mean free path before an electron will be scattered is limited by material impurities. Hence, it is still in the range of the normal skin effect and the skin depth can be calculated by equation (2.15). The surface resistance is hence given by:

$$R_s = \frac{\sqrt{\pi\, f\, \mu_0}}{\delta} = \frac{1}{\sigma\, \delta} \approx 7.591 \cdot 10^{-3}\Omega. \tag{4.6}$$

4.7.2 Computation of $\mathbf{Q_0}$

Based on the surfaces resistances the losses and the related quality factor are computed by the postprocessor SF0. For the execution of SF0 optionally an additional input file projectname.SEG can be used to define individual surface resistances for the different regions. This assignment as well as a definition of a related computation method is described in detail in [BY06]. To find out the related region numbers, the output file of a former SF0 computation can be used. By assigning the respective surface resistances to the associated regions the intrinsic quality factors of the models in figure 4.12 can be computed. The results are listed in table 4.2 together with the results from the related performance tests in chapter 5.

Table 4.2: Comparison of the intrinsic quality factors between the simulation and the measurements. For the calculation of the relative error the measurement values were used as reference.

setup	Q_0 simulated	Q_0 measured	relative error [%]
empty cavity	$1.426 \cdot 10^{10}$	$3.13 \cdot 10^{10}$	54.44
shielded gasket	$1.423 \cdot 10^{10}$	$9.11 \cdot 10^{7}$	15520.20
unshielded gasket	$2.85 \cdot 10^{8}$	$2.41 \cdot 10^{8}$	18.26

The comparatively large deviations between the simulations and the measurements for an empty cavity and the test setup with an unshielded gasket are most probably caused by the approximated values of the surface resistances used for the simulations. Additionally, former surface treatments carried out at the test cavity are not considered in the simulations. These treatments may have caused a reduction of the RRR at the surface with the consequence of a potentially increased quality factor. The low measured quality factor for the setup with the shielded gasket was due to the performance test experts possibly caused by a particle contamination.

4.8 Computation of $\mathbf{Q_{ext}}$ of the Input Antenna

Due to the predicted Q_0 degradation (in section 4.7) it needs to be verified, that impedance matching can still be ensured within the input coupler's antenna adjustment range. Otherwise the antenna needs to be elongated. For this verification the external quality factor is simulated as a function of the input couplers antenna penetration depth by CST Microwave Studio. CST is used since Superfish can not compute the external quality factor by itself. An approach to approximately compute Q_{ext} can be found in [Bal97]. The simualtion is carried out stepwise for the complete adjustment range of the usually used antenna at DESY of -16.7 to 11.8 mm. The zero point of the antenna is defined as the longitudinal level of the cavities flange marked in figure 4.15. For the simulations, a tetrahedral mesh with about 115000 cells is used to represent also minor diamter changes in the input coupler's antenna housing close to the connection. Within the adjustment range 143 equidistant points are computed. To check the plausibility of the simulations, the results are compared with before recorded measurement points. For these measurements an empty single cell cavity was used. Since the cylinder may have an impact on Q_{ext}, the simulation is repeated for an appropriate model of a cavity with the mounted cylinder insert.

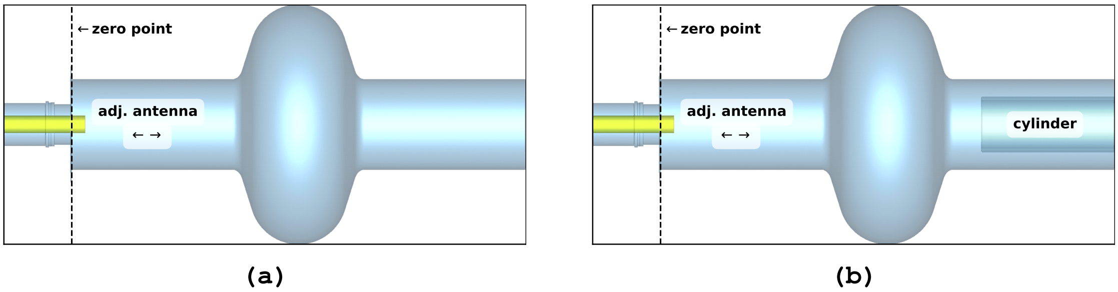

Figure 4.15: CST simulation models of an empty single cell cavity (a) and a cavity with the mounted cylinder insert (b). For both models the external quality factor of the input coupler's antenna is simulated as a function of the antenna penetration depth to investigate possible deviations between both models.

As shown in figure 4.16, almost no deviations between both simulated cases exist. Due to the diameter change at the transition between the antenna housing and the drift tube, the slope of Q_{ext} as a function of the antenna penetration depth is not linear for the range (in a semi-logarithmic plot).

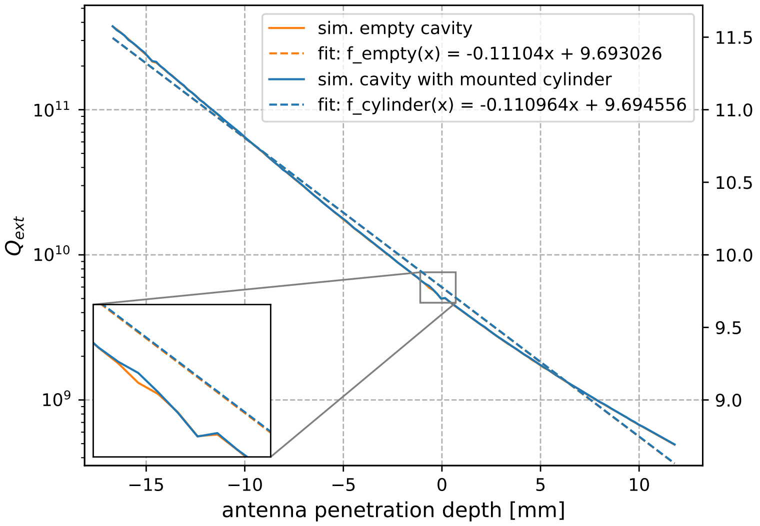

Figure 4.16: Comparison of the external quality factor as a function of the input coupler's antenna penetration depth between the models of an empty single cell cavity and a cavity with the mounted cylinder insert.

Since for all recorded measurement points the antenna does not penetrate the drift tube, the range used for the comparison is reduced to the range of the measured points as shown in figure 4.17.

By this reduction the data points of the simulation and the measurement can be fitted to the linear equation with a small error. The resulting fits can be used to calculate the mean deviation of the penetration depth for a given external quality factor. Thereby a minor deviation of about 0.26 mm can be derived. The smallest external quality factor that can be achieved by the maximal penetration depth is still too high to ensure impedance matching for the simulated intrinsic quality factor $2.85 \cdot 10^8$. For this reason a 12 mm longer antenna related to an external quality factor of $7 \cdot 10^7$ was used for the second performance test. Before the first test, the high Q_0 degradation was unforseen.

The small slope deviation between the fits is probably caused by the low amount of measurement points. Hence, it could be shown, that external quality factor can be precisely computed for the given geometry. Low deviations between the simulations and the measurements are importend for the development of a new field probe antenna design in the next section.

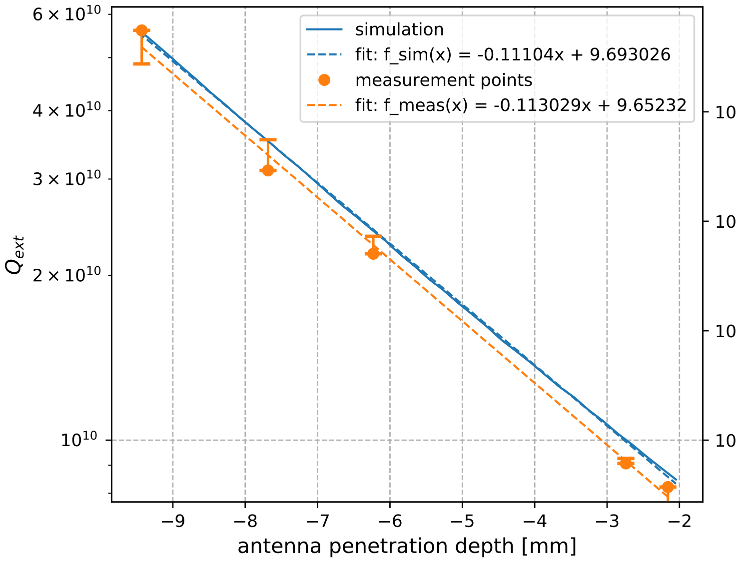

Figure 4.17: Comparison of the external quality factor as a function of the input coupler's antenna penetration depth between a simulation of an empty cavity and before recorded measurement points.

4.9 Field Probe Antenna Design

Alongside the cylinder insert the field density is faster decaying than in the drift tube because of the lower diameter. For this reason the normally used field probe antenna for single cell cavities needs to be replaced by a new design. The required external quality factor of the field probe antenna is a compromise between a large SNR of the measured signal and a low impact on the cavity's field distribution by additional power losses. Hence, the antenna is usually extensively undercoupled [PKH08, p. 145]. According to the operating engineer of the performance test stands, the field probe antenna should provide an external quality factor of $2 - 3 \cdot 10^{12}$ for cavities with a quality factor in the range of 10^{10} to 10^{11}. Since the extensive Q_0 degradation of the setup caused by the additional losses at the vacuum gasket was unknown before the first performance test, the new antenna is designed for an external quality factor of $2.5 \cdot 10^{12}$. For the antenna replacement, two approaches are investigated by RF simulations. The first one, the “thin probe antenna“ is designed to provide a low sensitivity to length deviations. These deviation may be caused during the mounting or the manufacturing of the antenna. This antenna design has a diameter of 3 mm. The second approach, the “thick probe antenna“ is a shortened version of the input coupler’s antenna used at DESY. Hence, this design with a diamter of 15 mm can be cost efficiently produced. Both designs are shown in figure 4.18.

The required antenna length that provides the desired external quality factor are found by a CST Microwave Studio optimisation.

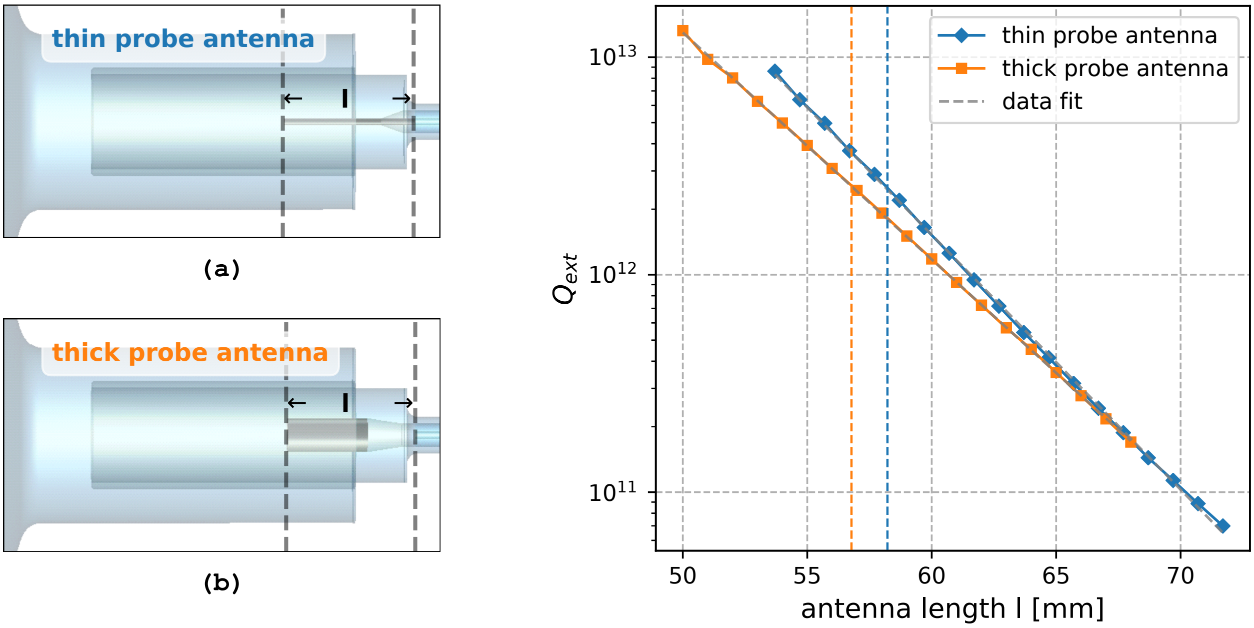

(a)

(b)

(c)

Figure 4.18: Thin field probe antenna design as an attempt to realise an antenna insensitive to length deviations (a). Shortened version of the adjustable antenna for the power coupling and therefore a cost efficient approach for the production at DESY (b). Comparison of the external quality factors as a function of the antenna length between both antenna designs. By the vertical dotted lines the length required for the desired external quality factor of $2.5 \cdot 10^{12}$ is marked (c).

By this procedure an optimal length of 54.52 mm is computed for the “thin probe antenna“ and a length of 56.78 mm for the “thick probe antenna“. In both cases the length of the diameter adapter is included. For both designs Q_{ext} was computed as a function of the antenna penetration depth. Thus, the sensitivity to length deviations can be evaluated. The results are shown in figure 4.18c. Since for both antennas a deviation smaller 1 mm is expected, the length sensitivity of both designs is uncritical. For this reason the “thick probe antenna “ was manufactured at DESY. The real antenna is shown in figure 4.19. Due to the in section 4.7 predicted low intrinsic quality factor, a longer version was produced for future performance tests. This antenna has a length of 77.11 mm for an external quality factor of $3 \cdot 10^{10}$.

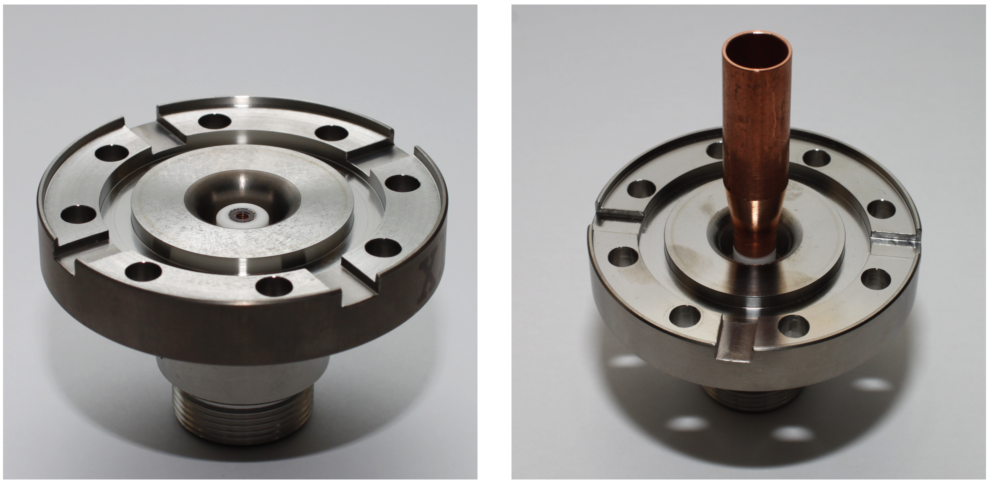
(a) (b)

Figure 4.19: Flange of a so called “HighQ antenna“ for the testwise power coupling during the production of 9-cell TESLA-shape cavities. This flange is used as the socket of the new field probe antenna (a). A shortened version of DESY’s input coupler’s antenna mounted on the HighQ flange. The antenna is used as a field probe during the performance tests (b).

Investigation of Possible Resonances in the Cylinder Insert

The field probe antenna and the cylinder insert are forming a structure similar to a so called coaxial resonator. Depending on the antenna length, this resonator may have a resonance in the range of the operating frequency of the test cavity (1.3 GHz). If this is the case for the desired antenna length the resonance would alter the measured signal and warm the cylinder insert. For this reason an additional resonace at the given frequency needs to be avoided. For this purpose, an adapted version of the C-program for the stepwise cylinder length increase described in section 4.3 is used. Instead of the cylinder, the antenna length is increased stepwise for a range of 0 - 90 mm and a stepwith of 0.1 mm. The low stepwidth is required due to the large quality factor of the setup and the related narrow bandwith. The zeropoint of the antenna length is defined as the end point of the diameter adapter divergent to the former definition (see figure 4.20a). This adapter has a length of 21.17 mm. To spot a potential additional resonance the magnetic field magnitude is evaluated close to the gap area of the field probe antennas flange (the evaluation point is marked by the red dot). By plotting the magnetic field magnitude at the evaluation point as a function of the antenna length possible additional resonances can be spotted. As shown in figure 4.21, by this method one resonance was found for an antenna length of 42.87 mm. The curve is normalised by its maximum value. Under the assumption of a large quality factor of this resonator and a related narrow bandwidth this resonace is uncritical for both computed antenna lengths.

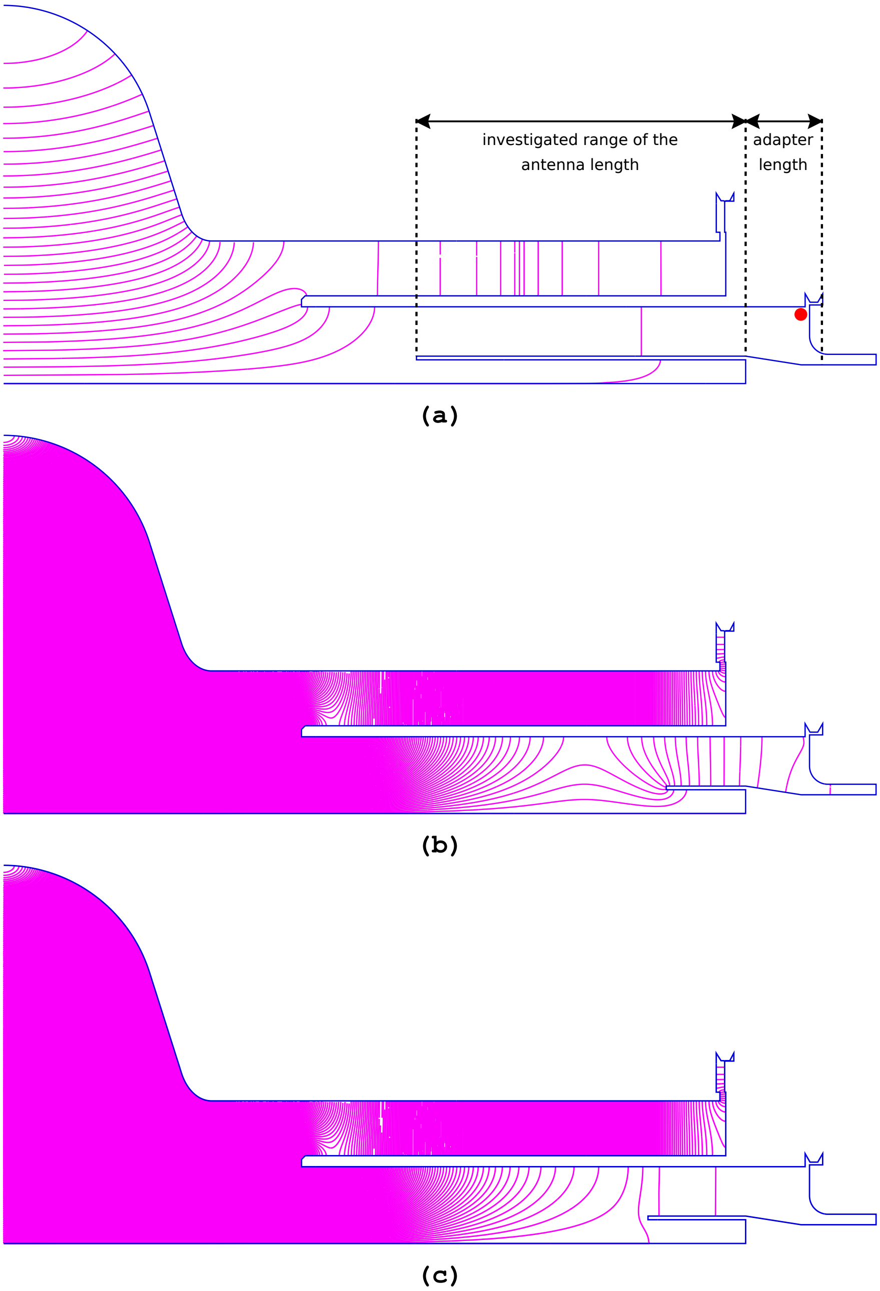

Figure 4.20: Section of the Superfish simulation model used to find possible additional resonances at the operation frequency of the cavity. The picture shows the longest investigated antenna length. The red dot marks the point where the magnetic field magnitude is evaluated (a). Second resonance at the cavity's operating frequency for an antenna length of 42.87 mm (b). Electric field distribution in the cylinder insert for a 5 mm longer field probe antenna (c).

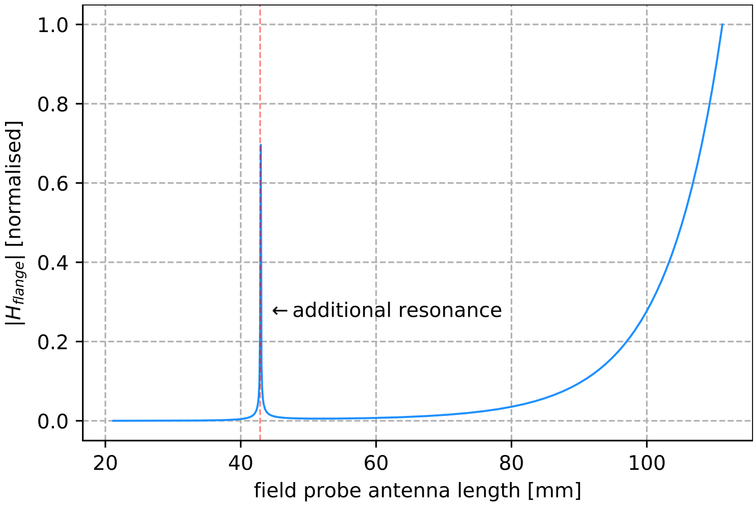

Figure 4.21: Normalised magnetic field magnitude at the red evaluation point in figure 4.20a as a function of the field probe antenna length (including the diameter adapter) simulated as an approach to detect possible unwanted resonances at the operating frequency of the setup.

4.10 Model Validation

To ensure the mapping of an actual connection displacement by the cylinder insert with an acceptable deviation several validation steps are carried out. The cavity's field distribution by the insert as well as the resonance frequency and the peak surface field magnitudes is evaluated by RF simulations. Due to the differences of the field distribution in a coaxial line and an empty drift tube driven below its cut-off frequency, possible deviations in the connection gap are computed to spot potential unexpected quench causing regions. At last, the impact of minor position deviations is simulated to evaluate the practical usability of the cylinder insert.

4.10.1 Field Distribution in the Test Cavity

To investigate the impact of the cylinder insert on the electric and magnetic field distribution both field components are evaluated along a field evaluation line located at the inner surface of the drift tube shown in figure 4.22. These field evaluations are carried out for a simulation model of an empty reference cavity, a cavity with a cylinder insert with a length l_c of 104.75 mm and one with an insert with a length of 115.98 mm. The shorter insert provides a magnetic field magnitude at the connection similar to a connection located at the mechanical limit and the large one a magnitude twice as high. For the simulation of the different field distribution cases Superfish is used. Due to the more descriptive images an appropriate CST Microwave Studio model is used for the field visualisation. Furthermore, deviations of the TM_{010} resonant frequency, the peak surface electric and magnetic field magnitudes are evaluated to detect possible deviations. The results are shown in table 4.3 and 4.4. Since all deviations are below 1 % they are uncritical and hence neglectable for the given application.

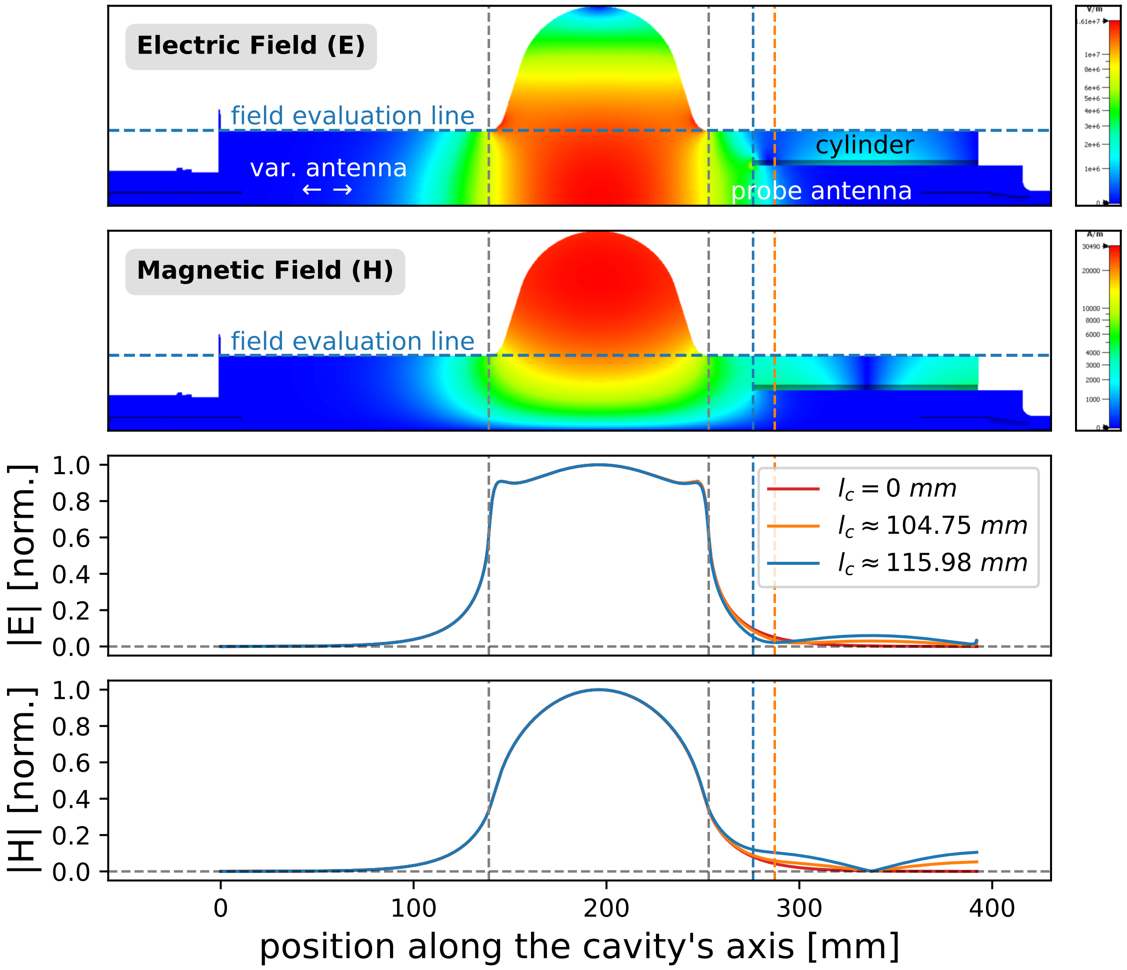

Figure 4.22: Alteration of the electric and the magnetic field distribution of the cavity by the cylinder insert. To investigate the impact of the cylinder insert on the field distribution the field density is evaluated along the depicted "field evaluation line" for an empty reference cavity, a cavity with the mounted short cylinder insert ($l_c = 104.75\,\text{mm}$) and one with the long insert ($l_c = 115.98\,\text{mm}$). The plotted field densities are computed by Superfish. For the pictures of the field distributions CST Microwave Studio is used.

Table 4.3: Evaluation of the deviations of the cavity's TM_{010} resonant frequency caused by the short and the long cylinder insert. The resonant frequency $f_r = 1299.26491\,\text{MHz}$ of an empty cavity is used as reference.

cylinder insert	f_r [MHz]	absolute error [MHz]	relative error [%]
104.75 mm	1299.18532	0.07959	0.006126
115.98 mm	1298.89482	0.37009	0.028485

Table 4.4: Relative error of the cavity parameters E_{pk} and H_{pk} caused by the short and the long cylinder insert. For the reference values a simulation model of an empty cavity is used.

	104.75 mm cylinder insert [%]	115.98 mm cylinder insert [%]
E_{pk}	0.205149	0.093851
H_{pk}	0.221405	0.117429

4.10.2 Field Distribution in the Connection Gap

The field distribution in an empty drift tube driven below its cut-off frequency is different from the distribution in a coaxial line. For this reason, the distribution in the connection gap needs to be compared between an actually and a virtually displaced connection by the cylinder insert. Furthermore, the impact of the position of the field evaluation point for the cylinder length optimisation program is investigated. By this investigation deviations of the provided field magnitudes of an actually and a virtually displaced connection caused by an unfavourable positioned field evaluation point can be avoided. For these comparisons suitable Superfish simulation models are used. The cylinder length optimisation program is used to compute the optimal cylinder length to provide a field magnitude in the connection area twice as high as at the mechanical position limit. Although the field evaluation point is located at the left surface of the connection gap entrance marked by a cross in figure 4.23. For both models, the radial field distribution inside the connection gap is evaluated along three field evaluation lines from the gap entrance on the level of the radius of the inner drift tube surface to the vacuum gasket. The first of these three field evaluation lines is longitudinally located at the surface of the first flange, the second one in the centre of the gap and the third one at the surface of the second flange. The simulated field magnitudes of the model with the cylinder insert are bisected for the further evaluation. This is necessary because of the requirement of a twice as high field magnitude.
The simulation results of the electric and the magnetic field magnitudes are plotted as a function of the radial position along the connection gap in figure 4.23. To evaluate the average deviation between both models the simulated field magnitudes are fitted to the linear equation by the Python function `numpy.polyfit()` of the library `numpy`. The computed functions are listed in table 4.5 and table 4.6. Due to the non-linearities at the gap entrance and the low contribution to the losses in the gap area by the end piece of the Niobium drift tube the first 2.39 mm are excluded from the fit. On basis of the fits, the average relative error is computed for the recorded radial field magnitudes in the connection gap by using the model of an actually displaced connection as reference. The results for the electric field magnitudes are listed in table 4.7 and for the magnetic field magnitudes in table 4.8.

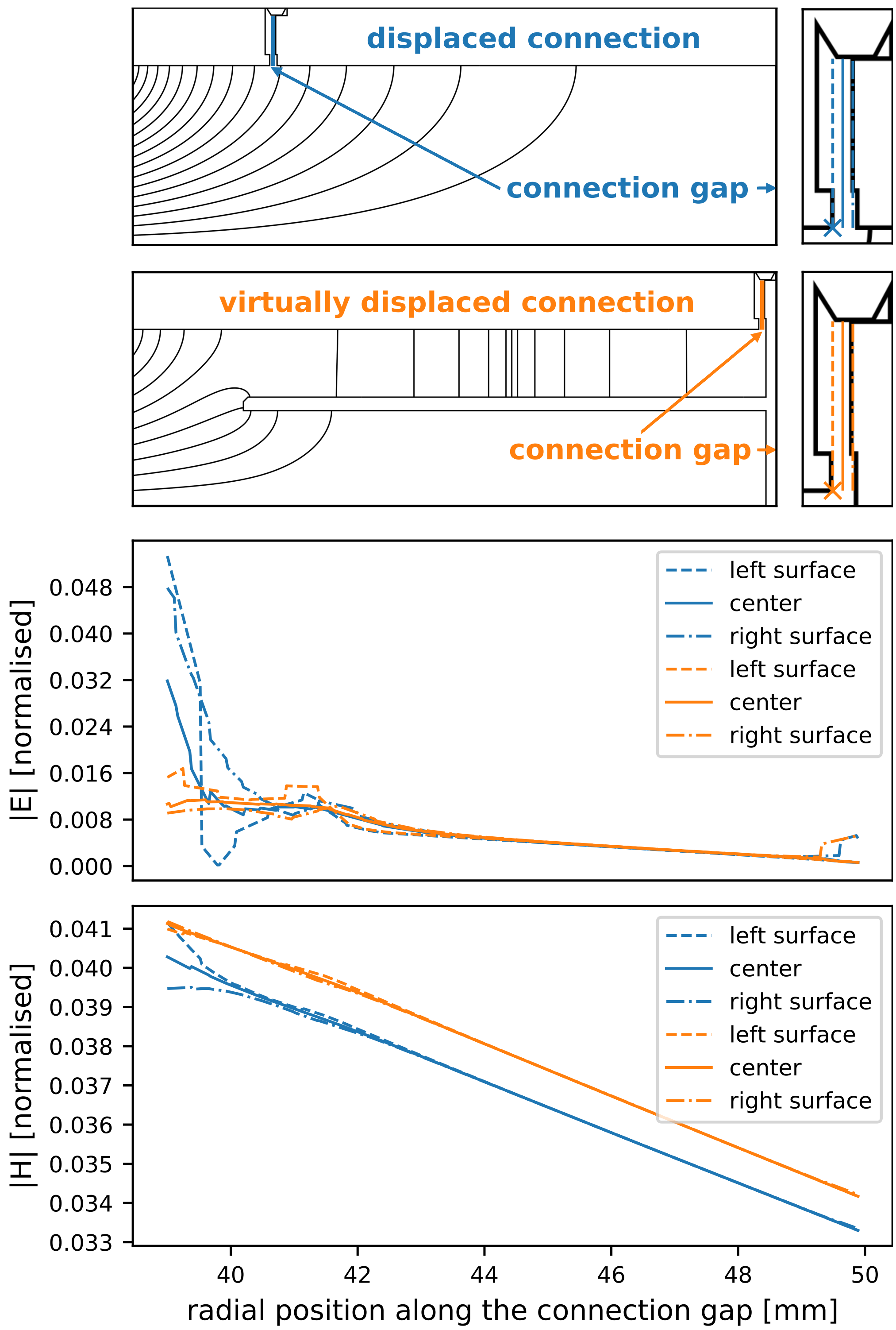

Figure 4.23: Comparison of the field distribution in the connection gap region of an actually displaced connection and a virtually displaced connection by the added coaxial line. The evaluation points are located at the left surface at the entrace of the connection gap as marked by a cross in the magnification windows. The magnitudes of the cylinder insert are bisected for the evaluation since the insert provides a field magnitude at the evaluation point twice as high as in an actually displaced connection.

Table 4.5: Results of the data fit of the **electric** field magnitudes along the field evaluation lines.

longitudinal position	fits for an actually displaced connection	fits for a virtually displaced connection
left surface	-0.00094694 x + 0.04714593	-0.00111132 x + 0.0549252
center	-0.00099447 x + 0.04948011	-0.00103959 x + 0.05165737
right surface	-0.00097094 x + 0.04873953	-0.00083798 x + 0.04271664

Table 4.6: Results of the data fit of the **magnetic** field magnitudes along the field evaluation lines.

longitudinal position	fits for an actually displaced connection	fits for a virtually displaced connection
left surface	-0.00064686 x + 0.06556019	-0.00066249 x + 0.0672129
center	-0.00063918 x + 0.0651979	-0.00065514 x + 0.06686598
right surface	-0.00063082 x + 0.06480682	-0.00064946 x + 0.06660179

Table 4.7: Results of the average error computation for the **electric** field magnitudes along the evaluation lines depicted in figure 4.23 of the connection gap.

longitudinal position	average relative error [%]
left surface	8.189005
center	3.066693
right surface	0.46665

Table 4.8: Results of the average error computation for the **magnetic** field magnitudes along the evaluation lines depicted in figure 4.23 of the connection gap.

longitudinal position	average relative error [%]
left surface	2.604868
center	2.607311
right surface	2.624685

By taking a closer look to the magnetic field magnitudes in figure 4.23, it can be noticed that the main deviation between both models is caused by the non-linear field decay above the position of the field evaluation point. For this reason, the field evaluation point is shifted to the centre of the connection gap as marked by a cross in figure 4.24 and the evaluation process is repeated. The results of the data fits are listed in table 4.9 for the electric field magnitudes and in table 4.10 for the magnetic field magnitudes. In table 4.11 and table 4.12 the results for the average relative error for both evaluation points are listed for a comparison. Furthermore, an “improvement factor“ to indicate the deviation reduction by the evaluation point shift is listed.

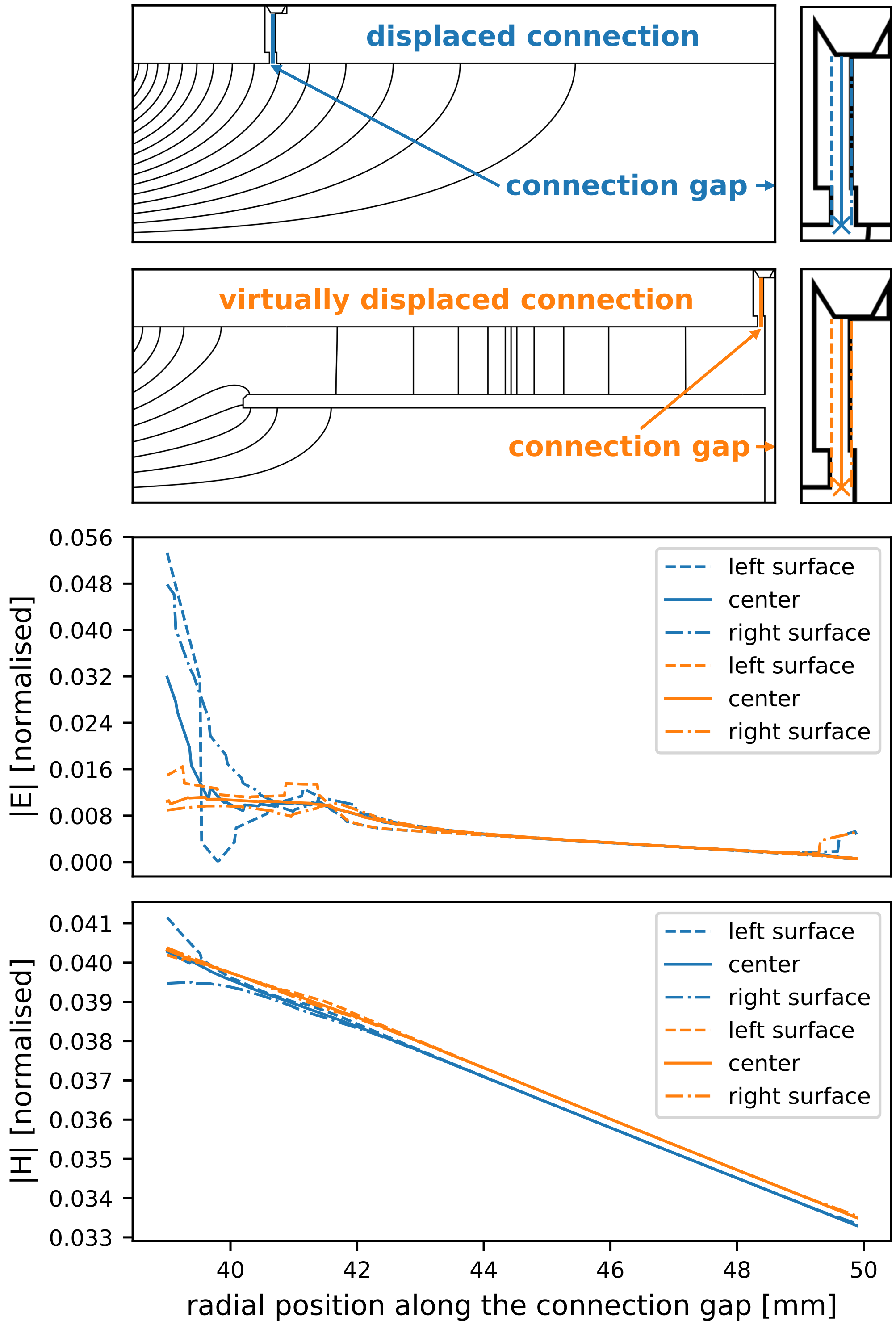

Figure 4.24: Comparison of the field distribution in the connection gap region of an actually displaced connection and a virtually displaced connection by the added coaxial line. The evaluation points are located in the centre of the entrace of the connection gap as marked by a cross in the magnification windows. The magnitudes of the cylinder insert are bisected for the evaluation since the insert provides a field magnitude at the evaluation point twice as high as in an actually displaced connection.

Table 4.9: Results of the data fits of the **electric** field magnitudes along the field evaluation lines after the evaluation point shift.

longitudinal position	**fits for an actually displaced connection**	**fits for a virtually displaced connection**
left surface	-0.00094694 x + 0.04714593	-0.00108964 x + 0.05385415
centre	-0.00099447 x + 0.04948011	-0.00101932 x + 0.05065002
right surface	-0.00097094 x + 0.04873953	-0.00082164 x + 0.04188365

Table 4.10: Results of the data fits of the **magnetic** field magnitudes along the field evaluation lines after the evaluation point shift.

longitudinal position	**fits for an actually displaced connection**	**fits for a virtually displaced connection**
left surface	-0.00064686 x + 0.06556019	-0.00064956 x + 0.06590122
centre	-0.00063918 x + 0.0651979	-0.00064236 x + 0.06556101
right surface	-0.00063082 x + 0.06480682	-0.00063679 x + 0.065302

Table 4.11: Comparison of the average relative errors of the radially recorded **electric** field magnitudes between the following two cases. For the first case the field evaluation point is located at the left connection surface of the gap entrance as marked in figure 4.23 and in the second case (case II) in the centre of the gap entrance as marked in figure 4.24. The improvement factor indicates the error reduction of case II in comparison to case I.

longitudinal Position	**average relative error [%]**		**improvement factor**
	case I	**case II**	
left surface	8.189005	6.08859	1.34
centre	3.066693	1.054247	2.91
right surface	0.46665	2.408424	0.19

Table 4.12: Comparison of the average relative errors of the radially recorded **magnetic** field magnitudes between the following two cases. For the first case the field evaluation point is located at the left connection surface of the gap entrance as marked in figure 4.23 and in the second case (case II) in the centre of the gap entrance as marked in figure 4.24. The improvement factor indicates the error reduction of case II in comparison to case I.

longitudinal Position	**average relative error [%]**		**improvement factor**
	case I	**case II**	
left surface	2.604868	0.602666	4.32
centre	2.607311	0.604081	4.32
right surface	2.624685	0.621287	4.22

By the evaluation point shift the average relative error can be reduced to values below 7 % for the electric field magnitudes. However, for the field magnitudes along the cylinder inserts flange surface the error increased by a factor of about five. In case of the magnetic field magnitudes a average relative error below 0.7 % can be achieved. The errors of both field components are considered to be uncritical for the usability of the connection displacement model in form of the cylinder insert.

4.11 Alteration of the Surface Losses

Due to the added cylinder insert the field distribution in the affected drift tube of the cavity is changed. Therefore, the proportional surface losses of the different surface regions in the drift tube and the connection gap are evaluated to spot potential unexpected quench causing regions. For this evaluation the following cases are simulated by Superfish. To serve as a reference a model of an empty single cell cavity with the geometry of the later test cavity is used. The impact of the cylinder insert is mapped by two models for two different cylinder lengths. In the first model of the short cylinder insert the cylinder has a length of 104.75 mm to provide a magnetic field magnitude at the connection gap similar to the reference point. The second model (of the long cylinder insert) for a field magnitude at the connection twice as large. Although, the cylinder has a length of 115.98 mm. Thus also the proportional losses of both cylinder models can be compared. To ensure a clear arrangement, the evaluation is separated in the drift tube area and the connection gap.

4.11.1 Proportional Surface Losses in the Drift Tube

To investigate the surface losses in the drift tube the models are subdivided into the segments marked in figure 4.25. The related losses of each segment can be extracted from the .SFO results file, generated after the execution of Autofish. To derive the proportional losses, the extracted losses are normalised by the total dissipated power in the reference model. The results are listed in table 4.13. For the segment A in the reference model a proportional power loss of 0.149402 % can be derived.

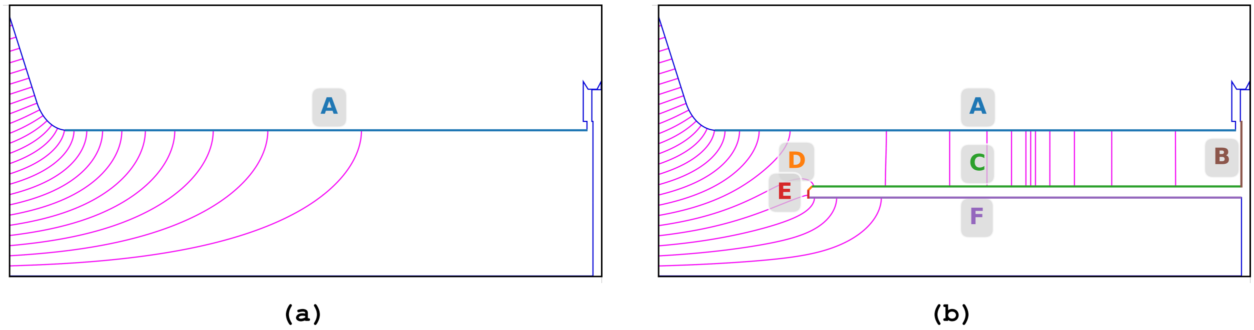

Figure 4.25: Superfish simulation model of an empty single cell cavity used as a reference for the losses along the inner drift tube surface (Segment A) (a). Assignment of the surface segments in the models to represent the impact of the cylinder insert. In the picture the longer cylinder version is shown (b).

In case of the short cylinder insert the losses alongside the drift tube increase by 19.94 % and for the long version by 89.40 %. Due to the low distance to the helium bath the increases are assumed to be uncritical. Only the losses on the outer cylinder surface may become a field limitting factor since the cylinder is only indirectly cooled by the Helium bath over the flange socket. Nevertheless, this design is chosen instead of an actively Helium cooled version realised by a double-walled cylinder. The reason for this decision is the highly increasing manufacturing effort.

Table 4.13: Comparison of the proportional surface losses of the segments marked in figure 4.25b of the short and the long cylinder insert. The increase of the particular losses is visualised by the “increasement factor“.

Segment	proportional surface losses [%]		increasement factor
	short cylinder insert	long cylinder insert	
A	0.179196	0.282965	1.58
B	0.007447	0.029736	3.99
C	0.025692	0.127023	4.94
D	0.000483	0.002005	4.15
E	0.000441	0.001757	3.98
F	0.000405	0.001543	3.81

4.11.2 Proportional Surface Losses in the Connection Gap

Similar to the different segments in the drift tube, the proportional losses are evaluated for the field exposed regions in the connection gap. The gap region is divided in the surface regions marked in figure 4.26a. This partitioning is chosen due to the different materials. Region 1 represents the end of the drift tube consisting of Niobium. The regions 2 and 4 are related to the two NbTi55-flanges (figure 4.26b) of the connection and region 3 represents the Aluminium (AlMgSi) vacuum gasket (figure 4.26c). The computed proportional losses for the different regions are listed in table 4.14. They are normalised by the total dissipated power in an empty reference cavity. The stored energy in the setup is identical for all three cases. For models containing a cylinder insert a large fraction of the dissipated power is related to the Aluminium vacuum gasket. This is the case because of the large surface resistance of the gasket in comparison to the superconducting surfaces. For this reason it is expected, that the losses at the gasket are the field limiting factor of the setup since they may indirectly cause a quench in the nearby flange surfaces. The rest of the listed values are considered to be inconspiciuos.

Table 4.14: Comparison of the proportional surface losses of the different regions in the connection gap between the following RF simulation models: An empty reference cavity, a cavity with a the short cylinder as well as one with the long cylinder insert.

region	material	proportional surface losses [%]		
		empty reference cavity	short cylinder insert	long cylinder insert
1	Nb	0.000000	0.001676	0.006694
2	NbTi55	0.000003	0.141089	0.559966
3	AlMgSi	0.026150	1239.077491	4920.264335
4	NbTi55	0.000004	0.179655	0.717362

(a) (b) (c)

Figure 4.26: Surface Regions of the connection gap: Region 1: End of the drift tube (Nb); Region 2: Flange surface of the test cavity (NbTi55); Region 3: Vacuum gasket (AlMgSi); Region 4: Flange surface of the cylinder insert (NbTi55) (a). NbTi55 cavity flange (b). Aluminium vacuum gasket (c).

4.12 Impact of Minor Position Deviations

Position deviations of the cylinder insert caused by manufacturing or the mounting process can not be entirely avoided. Therefore, a potential caused error on the measurement results for the critical magnetic field magnitude is investigated for the cases of a horizontal angle deviation of α equals 1°. As well as a deviation of the cylinders radial centre point of 1 mm. Both cases (illustrated in figure 4.27a) are simulated by CST Microwave Studio seperat and together (in the same direction). For the evaluation, the field deviations is recorded along a circle shown in figure 4.27b located a the end of the drift tube. A distance of 1 mm to the side walls is used to avoid problems caused by evaluating mesh cells close to the model boundaries. The simulation results for the evaluated cases are plotted in figure 4.27c. For the simulations a tetrahedral mesh with about $8 \cdot 10^5$ mesh cells is used for a precise mapping of the comparetively low geometry changes.

For the subsequent evaluation also, the field distribution along the circle for a cylinder insert with no deviations is recorded to serve as a reference. The point of the smallest distance between the cylinder insert and the inner drift tube surface is marked in the plot as the “lowest gap diameter“. For each deviation case the smallest and the largest percental deviation from the average value of the reference simulation are evaluated. The results are shown in table 4.15. The difference between the magnetic field extrema in case of the angle deviation is caused by the different evaluated longitudinal positions of the standing wave in the coaxial line. The assumed deviations should represent an expected possible worst case. In contrast to an expected component spread by a comparison to earlier investigations of superconducting connections in [GLR77], the contributed impact on the total error of the displacement model is considered to be uncritical. The actually caused error during the measurements is probably even much lower due to smaller misalignments.

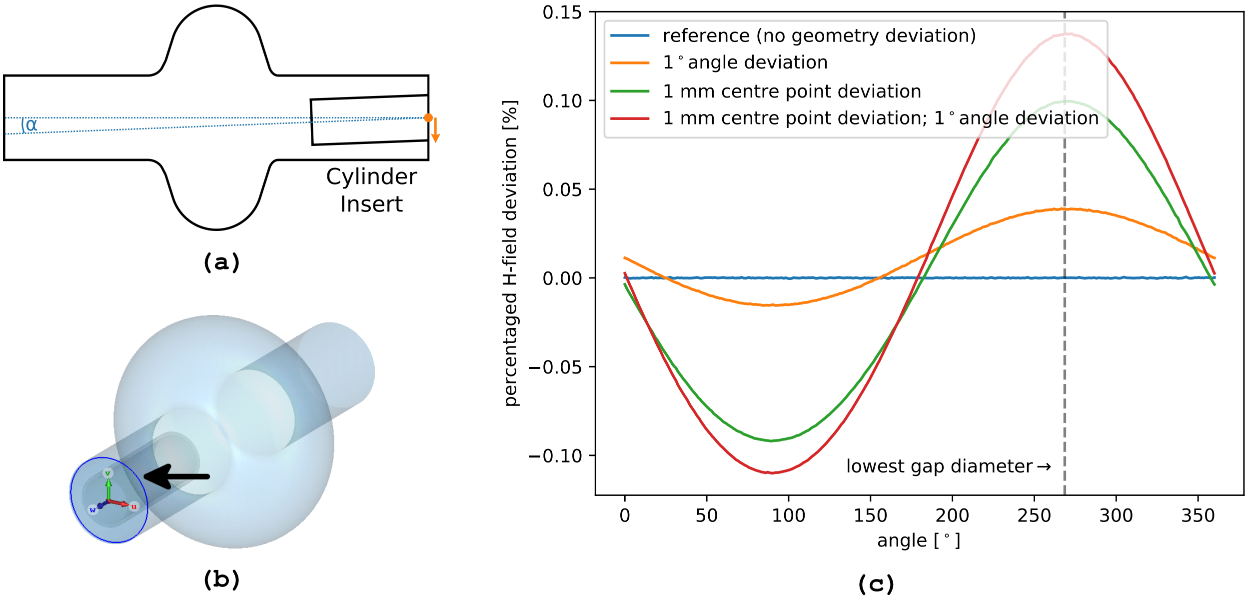

(a)

(b)

(c)

Figure 4.27: Position deviations of the cylinder insert: angle deviation (**blue**); centre point deviation (**orange**) (a), Position of the “field evaluation circle“ of the CST simulation model (b). Evaluation of the magnetic field magnitude deviations for the different deviation cases (c).

Table 4.15: Impact evaluation of minor cylinder insert centre point deviations (illustrated in figure 4.27a) to the extrema of the magnetic (H) field magnitudes along the field evaluation circle marked in figure 4.27b. The respectively evaluated deviations are marked by a cross.

1° angle deviation	1 mm centre point deviation	minimal H-field magnitude devitation	maximal H-field magnitude devitation
	X	-1.56 %	3.9 %
X		-9.20 %	9.96 %
X	X	-11.01 %	13.76 %

4.13 Manufacturing of the Cylinder Insert

For the manufacturing of the developed cylinder the CAD model shown in figure 4.28 designed by D. Klinke from DESY is used. The red section in the model is made out of a Niobium ingot with a RRR of 47. This ingot with a comparetively low purity is used since no material with a higher purity was available. For the flange area highlighted in green a NbTi55 alloy is used. This alloy provides the required material hardness to later ensure vacuum tightness of the connection. The differences in the surface roughness mark the passage from pure Niobium to NbTi55. The softness of the niobium lead to the rough cylinder surface.

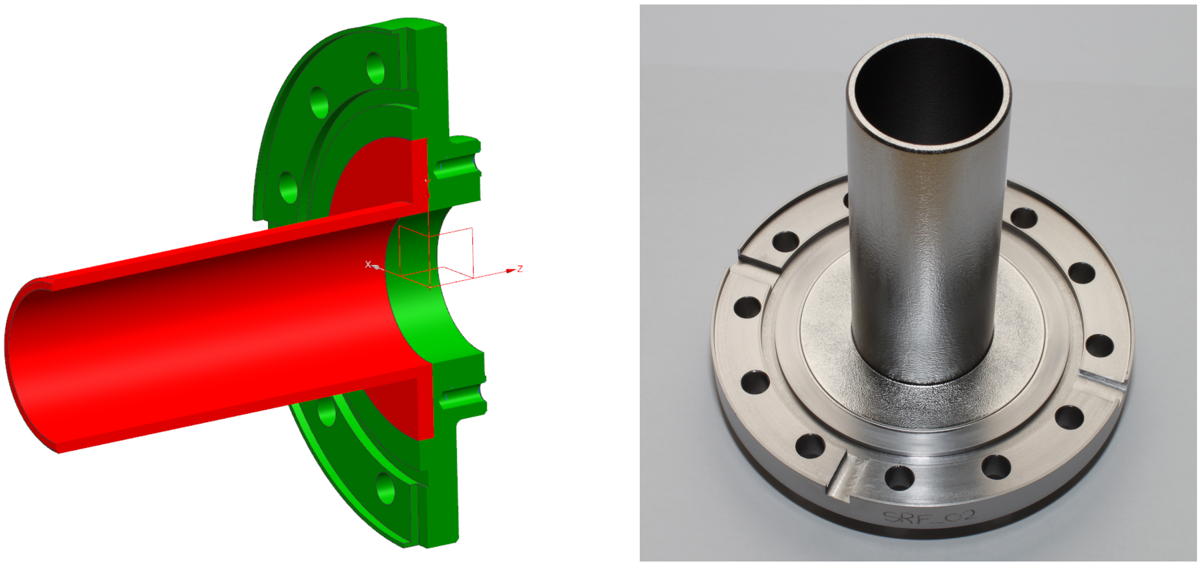

(a) **(b)**

Figure 4.28: CAD model of the cylinder insert for the manufacturing. The Niobium part (RRR 47) is highlighted in red. The green section is made out of a NbTi55 alloy (By courtesy of D. Klinke) (a). Top view of the cylinder insert after the manufacturing (b).

4.13.1 RF Shielding of the Connection Gap

As an attempt to increase the critical magnetic field of the connection, an RF seal shown in figure 4.29 to shield the connection gap was designed by D. Klinke from DESY. The design is based on former approaches to develop a superconducting connection developed in [GLR77] as well as commonly used solutions to ensure an RF contact at room temperature. The “teeth“ are bent alternately in the direction of the flange surfaces. During the mounting process these “teeth“ should scratch through the oxide layer of the flange surfaces as well as of the seal itself to ensure a good RF contact. An expectable particle contamination caused by this scratching process can be hopefully removed by high pressure rinsing (HPR) of the mounted setup before the vertical tests. A Q_0 degradation of the setup caused by higher losses in the connection gap at the vacuum gasket and the NbTi55 flange surfaces in case of a connection displacement can be potentially avoided too, by shielding the gap area.

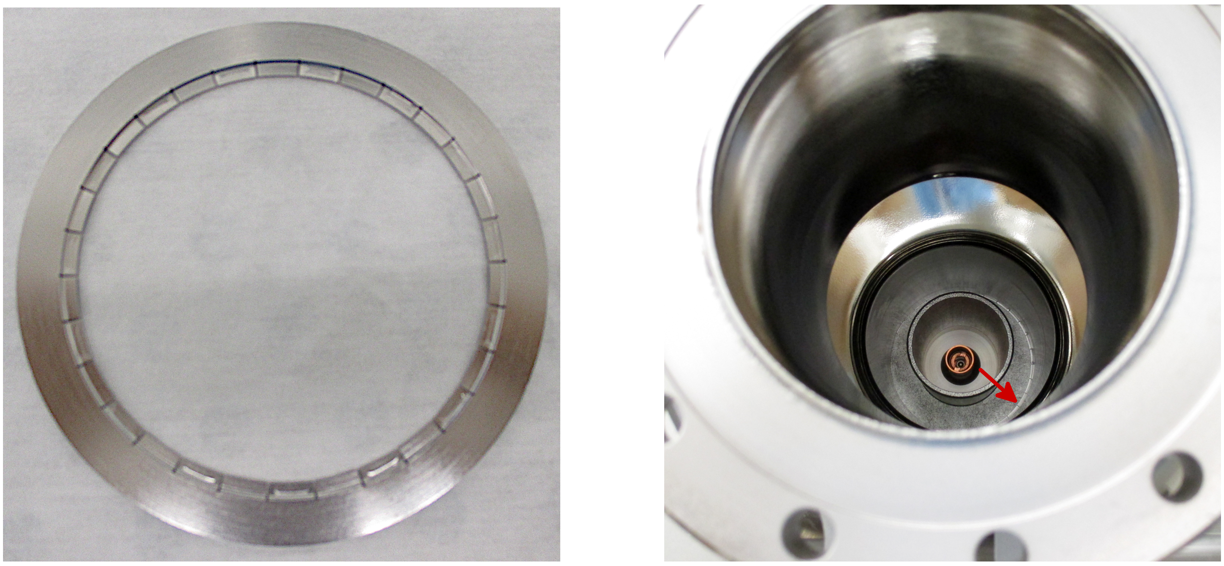

(a) (b)

Figure 4.29: The Niobium RF seal used as an attempt to shield the connection gap. By this seal the critical magnetic field of the connection should be increased (By courtesy of M. Schmoekel) (a). View through the test cavity on the mounted RF seal during the clean room assembly (By courtesy of M. Schmoekel) (b).

5 Vertical Performance Testing

Vertical tests are carried out to evaluate the overall performance of a cavity at the operating temperature. They are called vertical performance tests because the tests cavities are mounted in the required cryostat in vertical postion divergent to the operation in an accelerating facility. During these tests the Q_0 versus E_{acc} curve is recorded as the cavity's main figure of merit. Additionally, possible multipacting or field emissions can be detected. To record the Q_0 vs. E_{acc} curve the input power has to be increased stepwise until the breakdown of superconductivity occurs or a power limit is reached. For each step the average accelerating field and the related intrinsic quality factor of the setup are recorded. For the investigation of the critical magnetic field magnitudes of the different connection types only the breakdown point of this curve is required. By means of this point, the critical magnetic field at the connection can be evaluated by an alignment with an appropriate simulation model. This alignment procedure is described in detail in section 4.6. Within the following chapter, the execution of the vertical tests of a connection with an unshielded connection gap as well as for a connection with a shielded gap by the introduced RF seal is described. During the tests temperature sensors are used as an attempt to detect an asymetrical temperature increase of the vacuum gasket or the cylinder insert. To rule out that the cylinder insert is the field limitting element of the measurement setup a second sound quench detection system is used as well. By this system the origin of a phase change in the Helium bath from the superfluid state below 2.17 K to the normal fluid state can be detected [Bei19, pp. 13-17]. For this purpose, the propagation of the related pressure wave is recorded by a set of microphones and subsequently analysed by the system [Bei19, pp. 13-17]. If no pressure wave can be detected during the breakdown it is expected, that the breakdown must have been caused by the cylinder insert with no contact to the Helium bath. All vertical tests are carried out by M. Wiencek from DESY. The used cavity setup consisting of the field probe antenna, the cylinder insert, a single cell test cavity and the input coupler is shown in figure 5.1. For the test of the shielded vacuum gasket additionally the RF seal is mounted in the tested connection gap.

5.1 Temperature Detection

As an attempt to detect an asymmetrical temperature increase somewhere in the connection gap or of the cylinder insert, temperature sensors similar to the approach presented in [KMP94] are used. The temperature sensors based on calibrated carbon resistors are mounted in vicinity of the vacuum gaskets of the cylinder insert's connection as well as the connection of the field probe antenna as illustrated in figure 5.2b. The temperature sensors are arranged symmetrically on the flanges outer surface as shown in figure 5.2a. To allow a simple disassembly of the sensors after each vertical test,

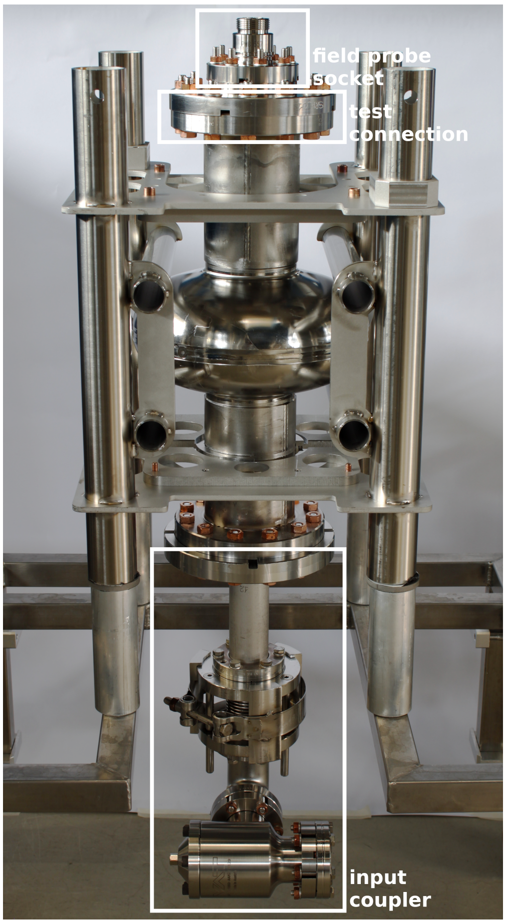

Figure 5.1: The cavity setup consisting of the field probe antenna, the cylinder insert, the test cavity and the input coupler mounted in a frame. On top, the socket of the field probe antenna mounted on the flange of the cylinder insert is shown. At the bottom, the housing of the input coupler is marked.

the sensors are surrounded on the sides by an isolating pad. They are pressed to the surface by a spring and no additional thermally conductive glue is used.

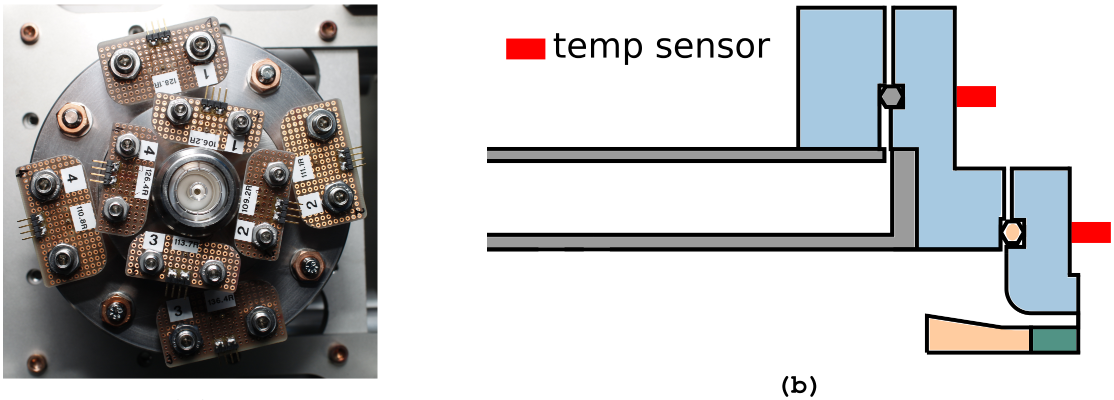

(a)

(b)

Figure 5.2: Arrangement of the temperature sensors mounted in vicinity of the vacuum gaskets of the investigated connection and the connection of the field probe antenna (a). Longitudinal cut of the cylinder insert connection to illustrate the longitudinal position of the temperature sensors (b).

Unfortunately, this assembling procedure has the disadvantage of a high risk of badly coupled sensors. The discribed thermometry system represents a first attempt of measuring asymetrical temperature changes. Due to the comparatively large distance to the origin of the temperature increase, influences on the actual temperature at the origin are only roughly possible. Additionally, minor temperature changes may remain undetected because of the distance. For this reason it is considered to drill holes in the flange close to the vacuum gaskets and glue the sensors to the ground of these holes in later vertical tests. Unfortunately, drilling close to the bearing area of the vacuum gasket endangers the vacuum tightness of the measurement setup because of a possible deformation of the bearing area caused by the drill or during the assembly due to a to low wall thickness.

5.1.1 Sensor Calibration

During the vertical test for each carbon resistor (temperature sensor) sampling points consisting of a timestamp and the voltage across the respective resistor are recorded in varying time intervals of about 2-30 seconds. To determine the related temperature an insitu calibration of the sensors needs to be performed, to avoid an impact of additional measurement components like wires and connectors on the measured voltage across the respective resistor. For the calibration either the pressure trend of the Helium bath during the cooldown or the warmup can be used. Exemplary, the to the pressure change related temperature curve for the warmup of the second vertical test is shown in figure 5.3a for the interval from 2.00 to 2.09 K. Since the instant of time of the measurement points is known for the reference curve as well as for the measured voltages across the temperature sensors, an alignment between the reference warmup curve and each sensor is possible. For the alignment, first the individual voltage change across each sensor needs to be computed. Since the number of recorded data points during the warmup varies between the different sensors as well as the reference curve, the individual voltage change is used to generate an array of equidistant data points from zero to the value of the maximal voltage change. In addition the number of elements has to equal the number of elements of the reference curve. Subsequently, each of these arrays are fitted by the exponential function $f(x) = a\,e^{-b\,x} + c$ with the Python method `curve_fit` of the library `scipy.optimize`. Exemplary, the reference curve together with the related data fit of the sensor Ch00 is shown in figure 5.3b. The computed functions for each of the sensors can finally be used for the evaluation of the recorded voltages across each temperature sensor.

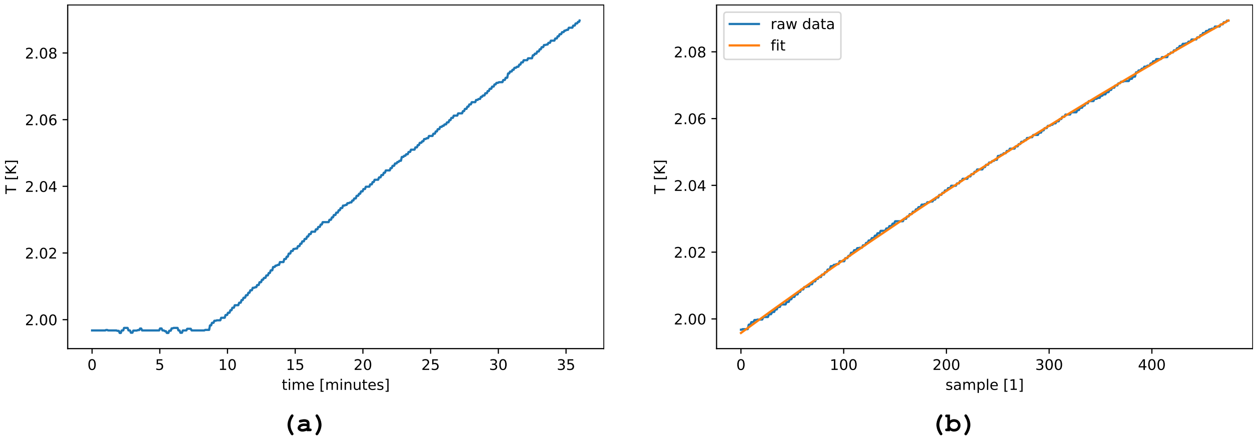

Figure 5.3: Reference warmup curve based on the pressure change (a). Exemplary data fit of the channel Ch00 of the second vertical test to the reference curve (b).

5.1.2 Determination of the Measurement Error

To determine the measurement error three reference sensors measuring the temperature of the Helium bath are used as shown in figure 5.4a. The temperatures are measured with an offset which needs to be matched to the reference curve before the evaluation of the measured error. To correct the offset of the reference channel based on the pressure changes of the Helium bath, the mean value of the time interval before the warmup is used to minimise the noise impact. This approach seems more stable than using a single data point for each curve. The temperature curves with the corrected offset are shown in figure 5.4b. The measurement error is given by the maximal deviation between the data points of the temperature curves and the reference curve.

5.2 First Vertical Test: Unshielded Vacuum Gasket

The first vertical test investigates the field limitation of a connection with an unshielded vacuum gasket. Before this test, the extensive Q_0 degradation mainly caused by the unshielded gasket was unforseen. For this reason the commonly used antenna of the input coupler with an adjustment range of -16.7 mm to 11.8 mm in relation to the zero point marked in figure 4.15 is used. Therefore, the minimal intrinsic quality factor Q_0 for which impedance matching can be achieved is $5 \cdot 10^8$. Furthermore, the field probe antenna designed to provide an external quality factor of $2.5 \cdot 10^{12}$ is used for the same reason. For the measurement the DESY single cell test cavity “1DE20“ is used. The test is carried out at a Helium bath temperature of 2 K.

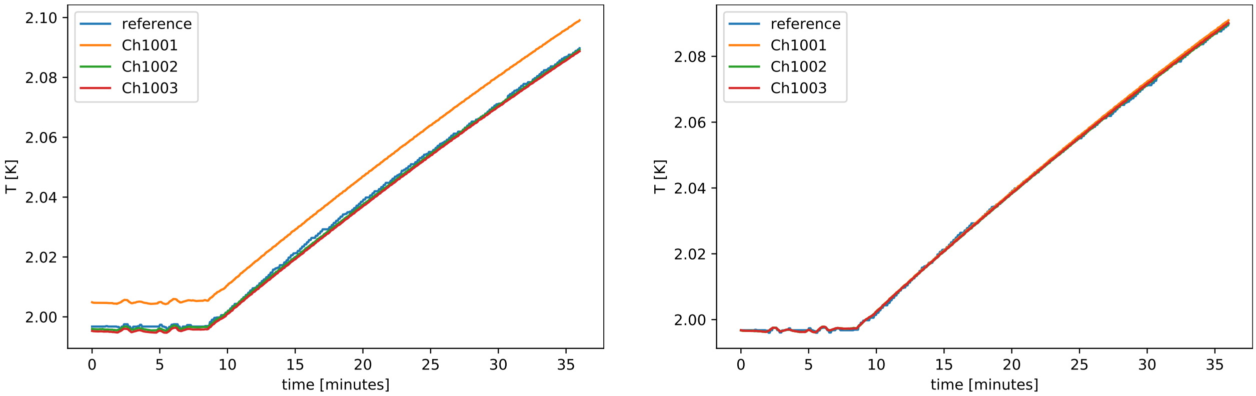

(a) **(b)**

Figure 5.4: Reference warmup curve based on the pressure change of the Helium bath together with the measurements of three temperature sensors in the bath before the offset correction (a). The same curves after the offset correction (b).

5.2.1 Measurement Execution

During the first vertical test the Q_0 vs. E_{acc} curve shown in orange in figure 5.5 was recorded. For comparison, a before measured curve, highlighted in blue of the empty test cavity is shown. In case of the measurement setup with the mounted cylinder insert, the quench occured already at an average accelerating electric field of about 4 MV/m and an intrinsic quality factor Q_0 of $3 \cdot 10^8$. The location of the quench could not be evaluated due to troubles with the second sound quench detection system.

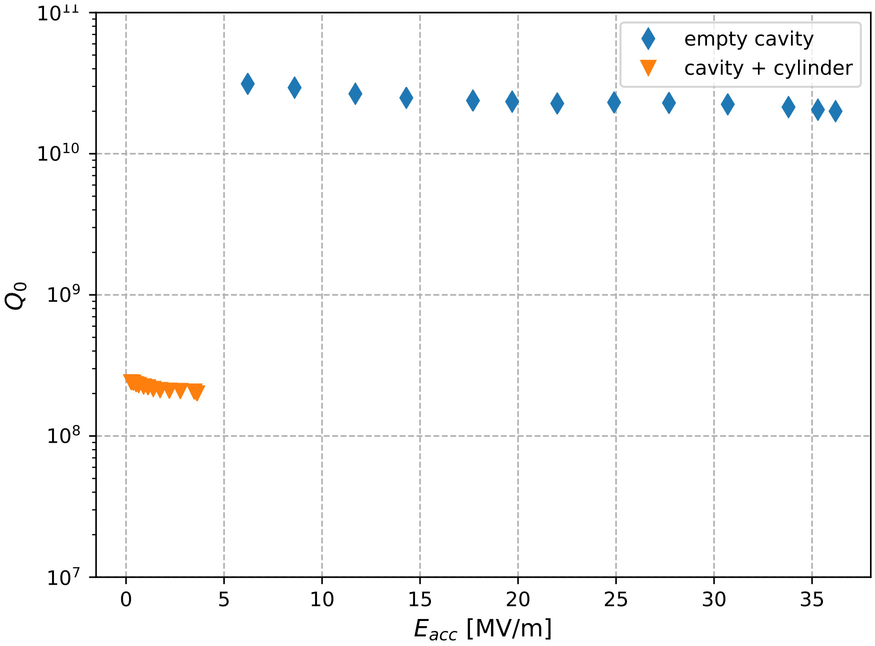

Figure 5.5: Q_0 vs. E_{acc} curve of the first vertical test to investigate the field limitation of a connection with an unshielded vacuum gasket. Additionally, the curve of a measurement of the empty test cavity is plotted for comparison.

5.2.2 Evaluation of the Temperature Sensors

None of the temperature sensors measured a signal above the measurement error of about 3.7 mK before the quench occured. Only by increasing the input power almost 20 times, a small temperature change of about 6 mK could be measured at two sensors close to the field probe antennas gasket.

5.2.3 Test Results

In the first vertical test of a connection with an unshielded aluminium vacuum gasket the quench occured at an average accelerating electric field E_{acc} of about 4 MV/m and an intrinsic quality factor of $3 \cdot 10^8$. According to the procedure described in section 4.6 this value for E_{acc} is related to a magnetic field magnitude in the centre of the connection gap entrance of about $9.576 \cdot 10^2$ A/m and a magnetic flux of about 1.2 mT. These values correspond to a minimal drift tube length of 65.6 mm under the assumption that the gap is the field limiting element of the setup. Before the breakdown occured, the temperature sensors mounted in vicinity of the vacuum gaskets did not measure any signals above the measurement error of about 3.7 mK. Since the second sound quench detection system was not available during the test, it can not be ruled out, that the quench was caused by the cylinder. For this reason the test needs to be repeated.

5.3 Second Vertical Test: Unshielded Vacuum Gasket

Due to the unknown quench location, the vertical test of the connection with an unshielded Aluminium vacuum gasket needs to be repeated. Before the execution of the test the following operations were carried out. Due to a minor impedance mismatch during the first vertical test, the input coupler's antenna was elongated by 12 mm. This length is related to an external quality factor Q_{ext} of $7 \cdot 10^7$. Furthermore, the cylinder insert was annealed at 800 °C to exclude a possible Hydrogen contamination of the Niobium surfaces.

5.3.1 Measurement Execution

The measurement of the average accelerating electric field E_{acc} and the intrinsic quality factor Q_0 of the measurement setup are carried out at the test stands at DESY by an automised procedure. According to the supervising engineer of the test stands, the procedure was developed for the measurements of cavities with quality factors in the range of 10^{10} to 10^{11} and corresponding ring down times of several seconds. For quality factors below 10^8 the measurement procedure does not record enough sampling points during the ring down process of the cavity to compute the intrinsic quality factor Q_0 of the setup with an acceptable accuracy. During the second vertical test, even for the maximal penetration depth of the elongated adjustable antenna of the input coupler corresponding to an external quality factor of $7 \cdot 10^7$ impedance matching could not be ensured. Due to this low quality factor, recorded measurement points in the Q_0 vs. E_{acc} curve in figure 5.6

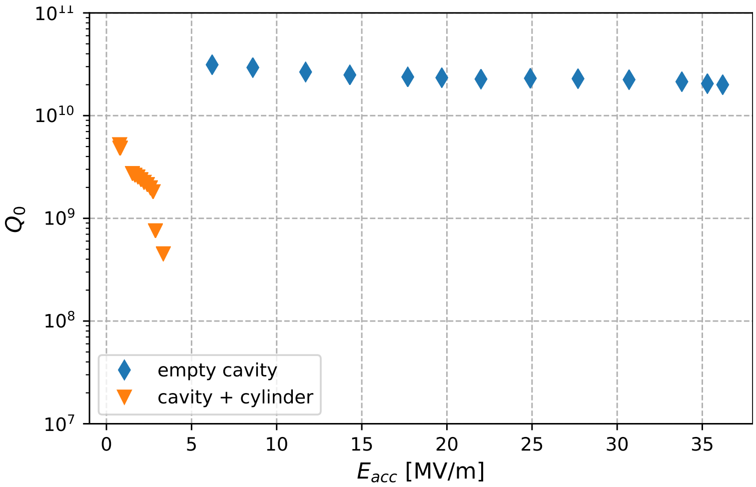

Figure 5.6: Q_0 vs. E_{acc} curve of the second vertical test plotted in orange in comparison to a before measured curve of the empty test cavity. Due to a to low amount of samples recorded during the ring down, the measured points are extensively deviating from the actual values and can not be used for the further evaluation.

show a large deviation from the actual values because of the mentioned reason and can not be used for further evaluations.

Since no reliable measurement could be carried out by the automised procedure the input power $P_{forward}$ was increased stepwise in steps of 10 W to manually record a couple of data points for a further investigation of a possible cause of the unexpected Q degradation. After each power increase the power $P_{forward}$ was kept constant for an interval of about 10 minutes. For each interval a timestamp, $P_{forward}$, $P_{reflected}$, $P_{transmitted}$ and a number indicating the the antenna penetration depth were recorded at the beginning and the end of each interval. The recorded data points are listed in table 5.1.

The penetration depth of the adjustable antenna of the input coupler was increased until the upper limit was reached because of a high fraction of reflected power of about 60 % at the beginning of the third interval. Even with the elongated adjustable antenna, impedance matching could not be ensured. Due to the increasing impedance mismatch for larger powers for the further evaluation the fraction:

$$P_{cavity} = P_{forward} - P_{reflected} \tag{5.1}$$

transmitted into the setup of $P_{forward}$ was calculated for the further evaluation. In figure 5.7 $P_{cavity}(P_{transmitted})$ is shown. The fraction $P_{transmitted}$ recieved at the field probe antenna decreases for larger values of $\mathrm{P_{cavity}}$ presumably because of an increasing surface resistance of the superconducting surfaces an related larger proportional losses.

Table 5.1: Manually recorded data points at the beginning and the end of each input power ($P_{forward}$) interval. The power transfered into the cavity P_{cavity} is calculated on basis of $P_{forward}$ and $P_{reflected}$.

timestamp [minutes]	$P_{forward}$ [W]	$P_{reflected}$ [W]	P_{cavity} [W]	$P_{transmitted}$ [mW]
00	10.05	5.67	4.38	0.03152
10	10.05	5.61	4.89	0.03195
11	20.03	12.13	7.90	0.05594
20	20.21	12.64	7.57	0.05919
23	30.07	13.80	16.27	0.148
34	30.30	14.33	15.97	0.147
35	40.11	18.27	21.84	0.1942
45	40.54	19.36	21.18	0.1834
46	49.97	24.22	25.75	0.2147
56	50.41	25.51	24.90	0.1974
57	60.04	31.10	28.94	0.2271
67	60.62	32.40	28.22	0.2066
68	70.01	37.92	32.09	0.2387
77	70.49	39.06	31.43	0.2224
78	80.03	44.00	36.03	0.2486
89	80.49	45.48	35.01	0.2322
91	90.15	57.08	33.07	0.1872
101	90.07	55.31	34.76	0.2105
102	99.58	61.04	38.54	0.2319
112	99.78	61.54	38.24	0.2253

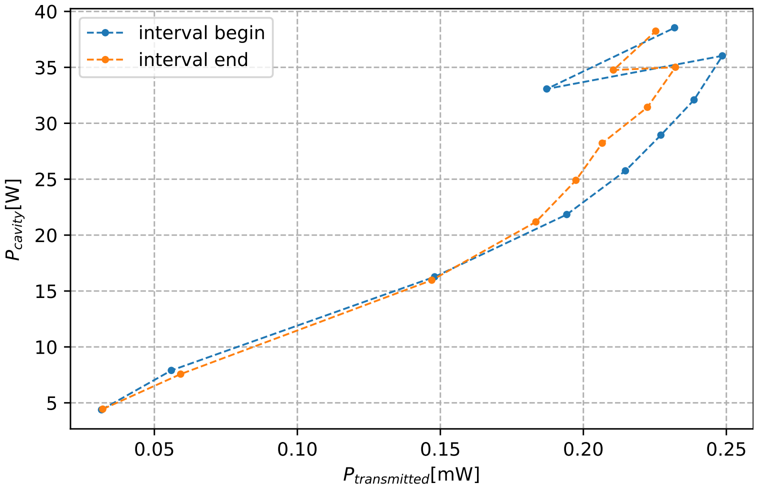

Figure 5.7: The power transmitted into the measurement setup P_{cavity} as a function of the power recieved at the field probe $P_{transmitted}$. The decreasing fraction of P_{cavity} recieved at the field probe for an increasing power P_{cavity} is caused by the increasing surface losses due to the surface warmup. The cause of the unstable behaviour for powers P_{cavity} above 30 W remains unknown.

5.3.2 Evaluation of the Temperature Sensors

To investigate possible asymetrical temperature changes of the test connection and the cylinder insert's socket, the values for $\mathrm{P_{cavity}}$ are aligned to the related measured temperatures with the help of their timestamps. The results of this alignment are shown in figure 5.8 together with a depiction of the location of the sensors. For the sensors a measurement error of about 2 mK was evaluated by the procedure described in section 5.1.2. During the time interval from the 68th minute to the 89th minute, sensor Ch00 measured divergent to all former power rises no temperature increase related to the power increase at the 78th minute. However, in the signal of sensor Ch07 this power rise can be noticed. For this reason, the warmup measured at the sensors has probably at least two different reasons. In case of a symmetrical warmup of the test connection's gasket and the cylinder insert, the sensor groups Ch00 to Ch03 and Ch04 to Ch07 should respectively measure almost the same temperatures. As visible in figure 5.8 this is not the case. To evaluate this asymmetry in detail, the sensor signals are plotted as a function of $\mathrm{P_{cavity}}$ in figure **??**. For a more detailed view of all measured temperatures as a function of $\mathrm{P_{cavity}}$ they are plotted separately in figure 5.11. For the maximal power transmitted into the setup the sensor Ch00 close to the gasket of the test connection measured a temperature increase of about 0.1 K. Also the neighbouring sensors Ch04 and Ch07 close to the cylinder insert's socket, measured a temperature significantly larger then the other two sensors of this group. Hence, presumably one of the warmup spots was located in the region of these three sensors. Two of the remaining sensors Ch01 and Ch02 close to the test connections gasket measured a minor temperature increase. The last sensor Ch03 measured no signal above the evaluated measurement error. Since the sensors were only pressed to the surface as shown in figure 5.10 and no thermally conductive glue was used, the coupling of sensor Ch03 was most probably unstable.

5.3.3 Test Results

During the second vertical test, the intrinsic quality factor Q_0 dropped in comparison to the first test below $7 \cdot 10^7$. For this reason, it became impossible to carry out the test with the automised procedure of the vertical test stands due to a low amount of recorded sampling points during the ring down time of the cavity. Instead, the input power $\mathrm{P_{forward}}$ was manually increased stepwise in time intervals of 10 minutes as an attempt to investigate the unexpected Q_0 degradation. An alignment with the signals of the temperature sensors showed an asymmetrical temperature increase probably caused by at least two origins. But, unstable coupled sensors can not be ruled out as the cause for this asymmetry. Even for the maximal power transmitted into the cavity $\mathrm{P_{cavity}}$ of about 38 W no quench occured in the setup.

5.4 Third Vertical Test: Shielded Vacuum Gasket

In the third vertical test the gap area of the connection was shielded by the developed RF seal. For this reason, the elongated antenna of the input coupler was replaced by the usual design since due to the shielding of the gap an increase of the intrinsic qualitiy factor Q_0 was expected. Additionally,

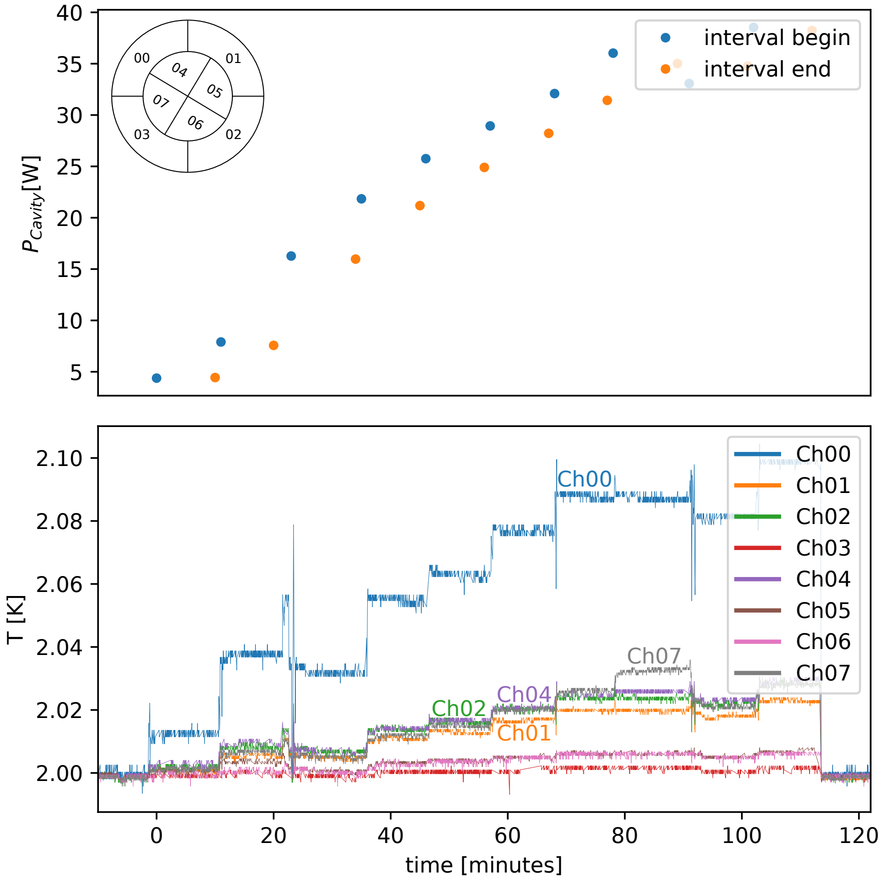

Figure 5.8: Power transmitted into the setup P_{cavity} measured at the begin and the end of each time interval in relation to the signals of the temperature sensors in vicinity of the vacuum gaskets. On the top left corner a sketch of the temperature sensor locations is shown.

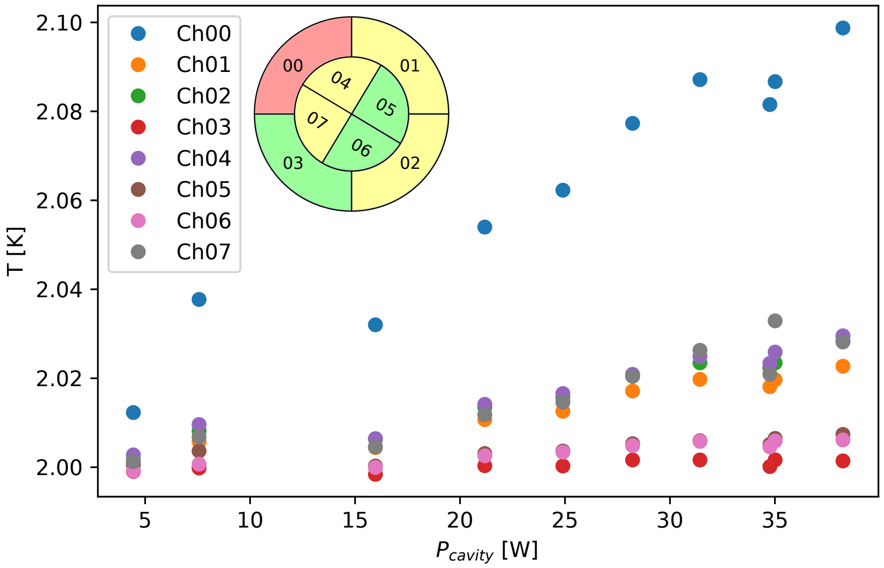

Figure 5.9: Comparison of the measured temperature sensor signals as a function of P_{cavity}. The different warmup regions are highlighted in the depiction of the sensor locations.

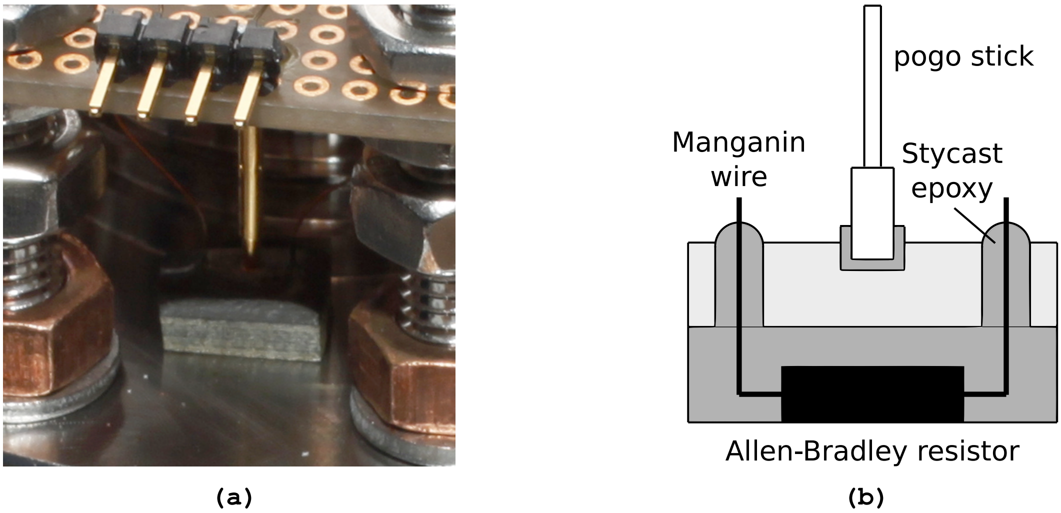

(a) **(b)**

Figure 5.10: Detailed view of one of the temperature sensors mounted in vicinity of the test connections vacuum gasket (a). Depiction of the configuration of the used temperature sensors. Adapted from: [KMP94, p. 2, Figure 1] (b).

it could not be ruled out, that the elongated antenna was the cause of the Q_0 degradation in the second vertical test.

5.4.1 Measurement Execution

During the vertical test the intrinsic quality factor of the setup appeared to be far below the minimal external quality factor of the input coupler. For this reason only about 1 W could be transmitted into the setup for the continious limit of the vertical test stand. Under these conditions it was not possible to perform a vertical test. Therefore, only the loaded quality factor $\mathrm{Q_L}$ of the setup is calculated by means of the formula in equation (5.2) [PKH08, p. 147 eq. (8.6)] based on a measurement of the cavity's ring down time of about 11 ms as follows:

$$Q_L = \omega \cdot \tau_L = 2 \cdot \pi \cdot 1.3\,GHz \cdot 11\,ms \approx 9.0 \cdot 10^7. \tag{5.2}$$

To verify this calculation additionally Q_L is calculated on basis of the 3 dB bandwidth Δf of the $\mathrm{TM_{010}}$ resonance. The bandwidth Δf of 15 Hz was measured by a network analyser. Hence, Q_L is given by:

$$Q_L = \frac{f}{\Delta f} = \frac{1.3\,\mathrm{GHz}}{15\,\mathrm{Hz}} = 8.67 \cdot 10^7. \tag{5.3}$$

Since the cavity is highly undercoupled the calculated values for Q_L are almost equal to Q_0.

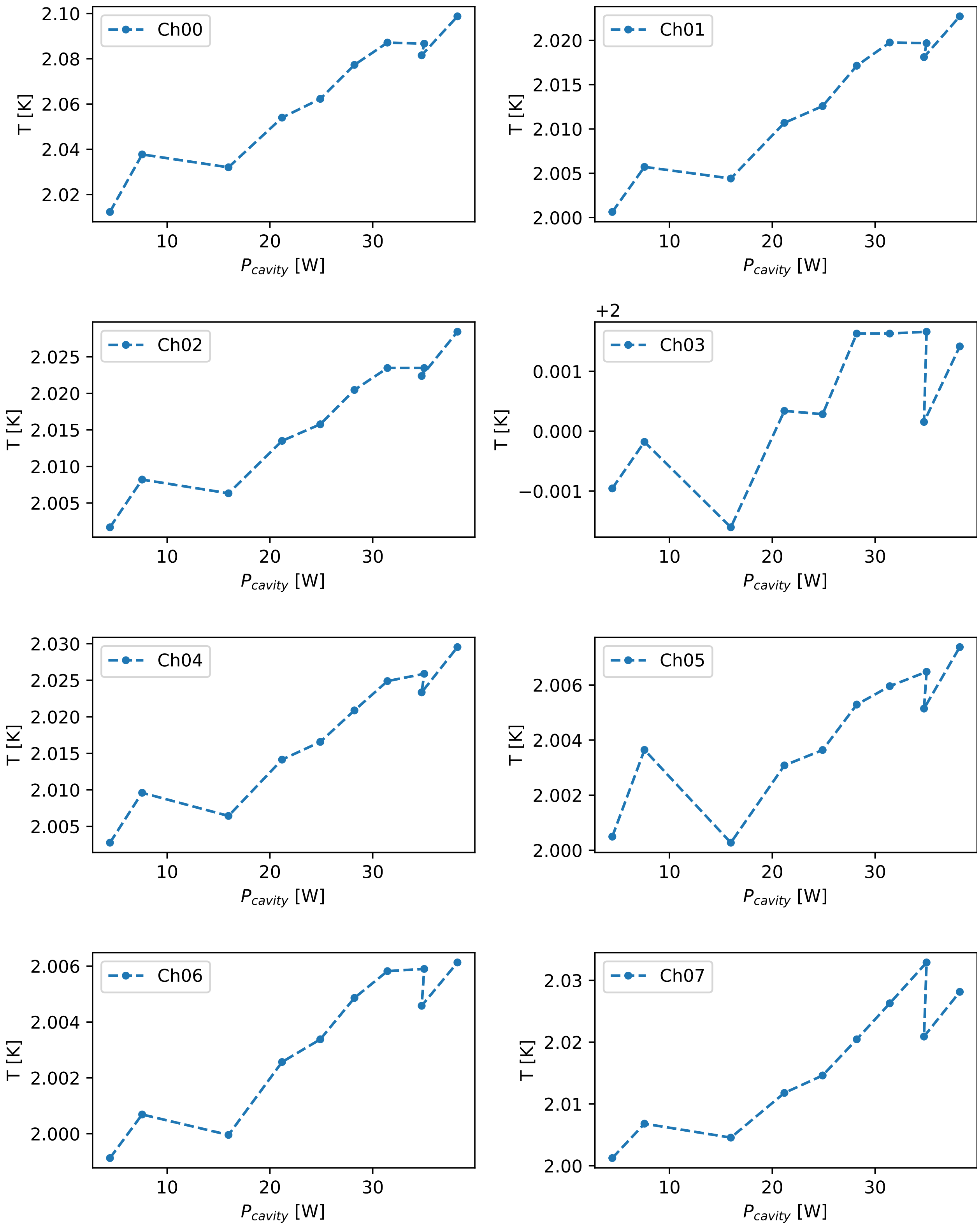

Figure 5.11: Seperated measurements of each temperature sensor as a function of P_{cavity} The sensors Ch00 - Ch03 are arranged symetrically in vicinity of the test connections vacuum gasket and the sensors Ch04 - Ch07 close to the gasket of the field probe antenna.

5.4.2 Evaluation of the Temperature Sensors

Since only a power of about 1 W could be transmitted into the measurement setup, a measureable signal could be excluded due to the experience made in the earlier vertical test's with the cylinder insert. For this reason the temperature signals of the sensors are not evaluated.

5.4.3 Test Results

Due to a high impedance mismatch between the input coupler and the cavity only a power of about 1 W could be transmitted into the cavity for the vertical test stands continious limit. For this reason it was impossible to perform a vertical test. Only a loaded quality factor Q_L of about $7 \cdot 10^7$ was separately determined by measurements of the ring down time of the cavity and its 3 dB bandwidth. Due to the low power transmitted into the cavity measurable temperatures can be excluded and the related signals were not evaluated.

Subsequently, the cavity was tested without the cylinder insert to investigate a possible intrinsic quality factor Q_0 degradation of the test cavity. During this test, the cavity showed a similar performance as during the measurements before the tests with the mounted cylinder insert. Hence, the test cavity is most likely not the cause of the bad perfomance during the second and the third vertical test. Only a possible damage of the drift tube surfaces may have remained undetected during the test because of the low field density in the drift tubes. For this reason it is considered to use the opposite drift tube, or to use another single cell cavity to mount the cylinder insert during the next vertical test.

6 Conclusion

To optimise the drift tube length of SRF cavities, it is required to know the critical RF field density of the connection. Thereby, an early quench of the cavity in the connection area can be prevented. To avoid a cost intensive drift tube length reduction of the cavity used for the investigation, in this thesis a model to virtually displace the connection was dimensioned and tested. For this purpose, a cylinder in the center of the drift tube is used to turn it into a coaxial line. That way, the field magnitude at the connection can be increased and the connection can be virtually displaced. The Niobium cylinder used for this purpose was designed, manufactured and tested in a single cell cavity in the scope of this thesis. It was dimensioned for the investigation of commonly used connections for TESLA-shape cavities at DESY. These connections are ensuring UHV-tightness by a normal conducting Aluminium gasket since they were designed for low field areas. For this reason a low field limitation was expected and hence an approach to increase the critical field density by shielding the vacuum gasket with a RF seal was tested as well. To ensure that an actual connection displacement can be modelled by the cylinder insert, the plausability of this model was successfully confirmed by RF simulations. Due to the higher field density at the connection and the related increasing losses at the normal conducting vacuum gasket, a degradation of the intrinsic quality factor was expected. This degradation was investigated by simulations on basis of the approximated surface resistances of the materials used in the setup. By means of the simulated intrinsic quality factor, the required antenna lengths for the input coupler and the field probe were evaluated as well.

Until now, three vertical tests with the mounted cylinder insert were carried out. During the first two tests the field limitation of a connection with an unshielded vacuum gasket was tested. In the first test, the measurement setup showed a gradient of about 4 MV/m and a related quality factor of about $3 \cdot 10^8$. This gradient corresponds to a magnetic flux of about 1.2 mT at the connection gap and a minimal drift tube length of about 65.6 mm. These values were evaluated by a comparison with an appropriate simulation model. Temperature sensors mounted on the blind flanges close to the vacuum gaskets were used as an attempt to detect an asymmetrical temperature increase. Due to the low input power and the large material thickness of the flanges, no signal exceeding measurement error could be measured. Because of a partially unavailable second sound quench detection system it could not be excluded, that the cylinder insert was the field limiting element of the setup. For this reason the test had to be repeated. During the second test, the setup showed an intrinsic quality factor Q_0 below $7 \cdot 10^7$. Because of an impedance mismatch between the input coupler and the setup, the maximal power P_{cavity} was limited to about 38 W. Until that point, no quench occured in the setup. Divergent to the first test, three neighbouring sensors measured an asymmetrical temperature increase. The low intrinsic quality factor may have been caused by a particle contamination of the setup. In the last vertical test the vacuum gasket was shielded by the RF seal. Because of a predicted intrinsic quality factor of about 10^{10} a shorter antenna was used in the input coupler. Unfortunately, the test setup showed a quality factor of only $9.1 \cdot 10^7$. Due to a high impedance mismatch, no vertical test could be performed. Again, a particle contamination of the cavity may be the cause of the quality factor degradation. Due to the first successful test and its confirmation via simulations, it is nevertheless expected, that the dimensioned cylinder insert can be used to model a connection displacement as soon as the issue of the supposed particle contamination is solved.

7 Outlook

The software solutions and the developed measurement setup provided in this thesis can be used for further similar investigations. During future vertical performance tests, the cause of the low intrinsic quality factors Q_0 of the last two vertical tests can be investigated. Additionally, it should be verified by means of the second sound quench detection system, that the cylinder insert was not the field limiting element of the setup during the first vertical test.

Otherwise it may be considered to close the iris facing side of the cylinder insert. By this modification, the cylinder can be actively Helium cooled to increase the critical field magnitude of the insert. This also enables the possibility to investigate the limitations of connection approaches with higher critical field magnitudes. Exemplary, the Aluminium vacuum gasket may be replaced by a Niobium coated one, to establish a superconducting connection.

The field probe antenna may be positioned sinked in a tube with a comparatively low diameter in the center of the cylinder closing cap to enable the required low external quality factor Q_t of the field probe.

8 Acknowledgement

I would like to thank A. Sulimov and R. Wendel for the kind and patient supervision of the thesis, H. Weise for the opportunity to write the thesis in his working group, all members of the groups MKS and MSL, especially C. Bate, T. Büttner, A. Gössel, D. Kostin, K. Lando, W.-D. Möller, D. Reschke, J. Sekutowicz, S. Sievers, L. Steder, E. Vogel, M. Wenskat and M. Wiencek, for their extensive support of the project, A. Ermakov for the specific resistance measurements, D. Klinke, J. Iversen and J.-H. Thie for the mechanical drawings of the cylinder insert and the monitoring of the manufacturing process, B. van der Horst and M. Schmökel for the clean room assembly, C. Ceylan, C. Müller and N. Engling for the installation of the temperature sensors as well as J. Eschke for the calibration, S. Arnold and S. Muhs for the manufacturing of the field probe antenna and finally my family and friends for their support during my studies.

List of Cited Literature

[AESS12] S. Aderhold, E. Elsen, F. Schlander, and L. Steder. A Common Cavity Coordinate System. Technical report, 3 2012. ILC-HiGrade-Report-2011-003-1.

[Bal97] P. Balleyguier. A straightforward method for cavity external q computation. *Particle Accelerators*, 57:113–127, 1997.

[BCS57] J. Bardeen, L. N. Cooper, and J. R. Schrieffer. Theory of Superconductivity. *Phys. Rev.*, 108:1175–1204, Dec 1957.

[BCS$^+$99] R. Bandelmann, G. Ciovati, J. Sekutowicz, A. Matheisen, X. Singer, and W. Singer. Nb Prototype of the Superstructure for the TESLA Linear Collider. pages 490–493, 1999.

[Bei19] B. Bein. Systematic Studies of a Cavity Quench Localization System. Master's thesis, University of Hamburg, Hamburg, Germany, 5 2019.

[BK13] W. Buckel and R. Kleiner. *Supraleitung.* WILEY-VCH Verlag, Weinheim, Germany, 7 edition, 2013.

[BY06] James H. Billen and Lloyd M. Young. *Poisson Superfish.* Los Alamos National Laboratory, Los Alamos, USA, January 2006. LA-UR-96-1834.

[Col86] E. W. Collings. *Applied Superconductivity, Metallurgy, and Physics of Titanium Alloys.* Plenum Press, New York, USA, 1 edition, 1986.

[Dav19] P. A. Davidson. *An Introduction to Electrodynamics.* OXFORD UNIVERSITY PRESS, Oxford, United Kingdom, 1 edition, 2019.

[DG02] M. Dressel and G. Grüner. *Electrodynamics of Solids.* CAMBRIDGE UNIVERSITY PRESS, New York, USA, 2002.

[Edw95] D. A. Edwards. TESLA Test Facility Linac Design Report. Technical Report Version 1.0, March 1 1995.

[EH00] C. Enss and S. Hunklinger. *Tieftemperaturphysik.* Springer-Verlag, Berlin / Heidelberg / New York, 1 edition, 2000.

[GC34] C. J. Gorter and H. B. G. Casimir. The thermodynamics of the superconducting state. Phys. Z., 1934. 35.

[GHH$^+$75] S. Giordano, H. Hahn, H. Halama, T. Luhman, and W. Bauer. Investigation of Microwave Properties of Superconducting Nb0.4Ti0.6. *IEEE Transactions on Magnetics*, 11(2):437–440, March 1975.

[GLR77] M. Grundner, H. Lengeler, and E. Rathgeber. Rf contact for superconducting resonators. *Nuclear Instruments and Methods*, 141(1):57 – 59, 1977.

[Hal70] J. Halbritter. FORTRAN-Program for the computation of the Surface Impedance of Superconductors. Technical Report 3/70-6, June 1970.

[Hum71] R. E. Hummel. *Optische Eigenschaften von Metallen und Legierungen.* Springer-Verlag, Berlin / Heidelberg / New York, 1 edition, 1971.

[Jac82] J. D. Jackson. *Klassische Elektrodynamik.* Walter de Gruyter, Berlin / New York, 2 edition, 1982.

[Jun12] T. Junginger. *Investigations of the surface resistance of superconducting materials.* PhD thesis, Ruperto-Carola University of Heidelberg, Heidelberg, Germany, 2012.

[KCS+07] P. Kneisel, G. Ciovati, J. Sekutowicz, A. Matheisen, X. Singer, and W. Singer. Development of a Superconducting Connection for Niobium Cavities. In *2007 IEEE Particle Accelerator Conference (PAC)*, pages 2484–2486, June 2007.

[Kle17] R. Kleinsdienst. *Radio Frequency Characterization of Superconductors for Particle Accelerators.* PhD thesis, Universität Siegen, Siegen, Germany, 2017.

[KMP94] J. Knobloch, H. Muller, and H. Padamsee. Design of a high speed, high resolution thermometry system for 1.5 GHz superconducting radio frequency cavities. *Review of Scientific Instruments*, 65:3521 – 3527, 12 1994.

[LAA] Download area for poisson superfish. `https://laacg.lanl.gov/laacg/services/download_sf.phtml`. Accessed: 2019-07-26.

[MB58] D. C. Mattis and J. Bardeen. Theory of the Anomalous Skin Effect in Normal and Superconducting Metals. *Phys. Rev.*, 111:412–417, Jul 1958.

[Mei66] H. H. Meinke. *Elektromagnetische Felder und Wellen.* Springer-Verlag, Berlin / Heidelberg, Germany, 2 edition, 1966.

[MR91] S. B. Maurer and A. Ralston. *Discrete Algorithmic Mathematics.* Addison-Wesley Publishing Company, USA, 1 edition, 1991.

[Pap11] L. Papula. *Mathematik für Ingenieure und Naturwissenschaftler Band 3.* Vieweg+Teubner Verlag, Wiesbaden, Germany, 3 edition, 2011.

[Peh12] E. Pehl. *Mikrowellentechnik.* VDE VERLAG GMBH, Berlin, Germany, 3 edition, 2012.

[PKH08] H. Padamsee, J. Knobloch, and T. Hays. *RF Superconductivity for Accelerators.* WILEY-VCH Verlag, Weinheim, Germany, 2 edition, 2008.

[Pro93] D. Proch. The TESLA Cavity: Design Considerations and RF Properties. *Proc. 6th Workshop on RF Superconductivity*, pages 382–397, 01 1993.

[Ric65] G. Rickayzen. *Theory of Superconductivity.* John Wiley & Sons, Inc, USA, 1 edition, 1965.

[ROKS53] H. J. Reich, P. F. Ordung, H. L. Krauss, and J. G. Skalnik. *MICROWAVE THEORY AND TECHNIQUES*. D. VAN NOSTRAND COMPANY, INC., Princeton, New Jersey, USA, 1 edition, 1953.

[Swa] H. Swan. Srimp. `https://www.classe.cornell.edu/~liepe/webpage/researchsrimp.html`. Javascript translation of the Halbritter code.

[Tho04] J. Thoms. *Hochfrequenzuntersuchungen an niedrigdimensionalen Supraleitern*. PhD thesis, Universität Stuttgart, Stuttgart, Germany, 2004.

[Wan08] T. P. Wangler. *RF Linear Accelerators*. WILEY-VCH Verlag, Weinheim, Germany, 2 edition, 2008.

[XFE10] Technical Specifications, Nb55Ti Alloy. Technical Report Revision C, May 07 2010. XFEL/008.

A Appendix

The appendix of this thesis is stored on the enclosed CD.

Erklärung zur selbstständigen Bearbeitung einer Abschlussarbeit

Hiermit versichere ich, dass ich die vorliegende Arbeit ohne fremde Hilfe selbständig verfasst und nur die angegebenen Hilfsmittel benutzt habe.

Ort	Datum	Unterschrift im Original